National Library of Canada

Acquisitions and Bibliographic Services Branch

395 Wellington Street
Ottawa, Ontario
K1A 0N4

Bibliothèque nationale du Canada

Direction des acquisitions et des services bibliographiques

395, rue Wellington
Ottawa (Ontario)
K1A 0N4

Your file Votre référence

Our file Notre référence

NOTICE

The quality of this microform is heavily dependent upon the quality of the original thesis submitted for microfilming. Every effort has been made to ensure the highest quality of reproduction possible.

If pages are missing, contact the university which granted the degree.

Some pages may have indistinct print especially if the original pages were typed with a poor typewriter ribbon or if the university sent us an inferior photocopy.

AVIS

La qualité de cette microforme dépend grandement de la qualité de la thèse soumise au microfilmage. Nous avons tout fait pour assurer une qualité supérieure de reproduction.

S'il manque des pages, veuillez communiquer avec l'université qui a conféré le grade.

La qualité d'impression de certaines pages peut laisser à désirer, surtout si les pages originales ont été dactylographiées à l'aide d'un ruban usé ou si l'université nous a fait parvenir une photocopie de qualité inférieure.

Canada

TIDAL FLOW MODIFICATION BY A SMALL BAY IN THE LOWER ST. LAWRENCE ESTUARY

Bernard E. Laval

Department of Atmospheric and Oceanic Sciences

McGill University, Montreal

October, 1995

A THESIS SUBMITTED TO THE FACULTY OF GRADUATE STUDIES

AND RESEARCH IN PARTIAL FULFILMENT OF THE

REQUIREMENTS OF THE DEGREE OF

MASTER OF SCIENCE

ISBN 0-612-08023-4

Canada

Abstract

The tidal flow characteristics around L'Anse du Petit Mitis were described using velocity data from six moored current metres. L'Anse du Petit Mitis is a shallow bay in the lee of the downstream slanting Pointe Mitis. The predominantly M_2 current showed the following signs of tide induced transient recirculation within the bay: the M_2 phase within the bay is 65° ahead of that outside of the bay; the amplitude of the M_4 and Eulerian mean constituents are relatively large within the bay; and the M_2 tidal ellipse and the Eulerian mean are oriented towards the tip of Pointe Mitis. The effects of tide induced transient recirculation were not found to extend to the station furthest within the bay. Flow in the bay region was found to be an order of magnitude weaker than the free stream tidal flow.

Résumé

Les caractéristiques des courants de marée près de l'Anse du Petit Mitis sont décrites a l'aide des données de vitesse obtenues avec six courantomètres. Les courants prédominants M_2 possèdent dans la baie les signent suivants de recirculation transitoire induite par la marée: la phase du courant M_2 devance de 65° celle a l'extérieur de la baie; l'amplitude du courant M_4 et de la moyenne eulerienne sont relativement grande à l'intérieur de la baie; et puis, l'ellipse de marée M_2 ainsi que la moyenne Eulerienne sont orientées vers l'extrémité de Pointe Mitis. Les effets causés par la recirculation transitoire induite par la marée n'ont pas été décelés par la station située la plus à l'intérieur dans la baie. L'écoulement dans la baie a été mesuré comme étant un ordre de grandeur plus faible que l'écoulement libre des marées.

Acknowledgements

First of all, a big thank you to Martin Levesque - capitaine, mon capitaine - merci pour toutes les heures de conversation, tous les castes de CTD, et de m'avoir retourné à la rive chaque soir sain et sauf. Merci à la bande de fou de la maison blanche pour m'avoir aidé, pour les soirées interessantes, et surtout pour les sorties de vélo. Thank you Paul Peltola for preparing all of the equipment, and Guy Millette for keeping them working even when they didn't want to. I am also very grateful to Jean-Yves Anctil of GIROQ for his help in designing moorings tough enough to withstand any nor-easter.

While back at the ranch, analyzing data, I had many insightful conversations with David Oxilia, Patrick Doyon, Martin Charron, Phil Archambault, Tineke van der Baaren, and Chris Hampel. Thank you. Of course the data analysis wouldn't have been possible without having Jean-Claude Croteau keeping the computers running.

Most of the help with the data analysis came from Dr Bohyun Bang. Thank you for having enough patience to deal with my ramblings. I learnt a lot from you.

I would like to thank my supervisor Dr Grant Ingram for trusting me with his equipment, for financial support, and for trusting me enough to write a thesis that I can call my own.

Table of Contents

List of Tables

List of Figures

1. Introduction

It was shown by Therriault and Levasseur (1985) that the least primary productivity in the lower St. Lawrence estuary occurs in the region along its south shore. Primary productivity in this region was not found to be nutrient limited and the authors invoked physical arguments to explain the reduced primary productivity. They suggested that the reduced productivity is due to high flushing rates induced by the combined outflow of the St. Lawrence and Saguenay rivers, as well as high turbidity associated with the riverine input and tidal mixing. While Therriault and Levasseur's work provides insights into the outflow region as a whole, near shore in shallower waters where flow interacts non-linearly with coastal features such as bays and promontories, the marine environment can be very different.

When viewing the St. Lawrence estuary as a whole, the south shore appears to be straight and featureless (figure 1). Zooming in, to a scale of 10's of kilometres, promontories and bays with an offshore extent on the order of one kilometre become evident (figure 2). Water can become trapped

downstream of these features in the same way that water can become trapped behind rocks along the shore of a river, as was found in field experiments by Fischer *et al.* (1979). This entrapment effect of coastal features could decrease the mean velocity of water borne material travelling near the shore, negating the high flushing rate argument proposed by Therriault and Levasseur (1985) to explain the low productivity of this region.

Studies have shown that coastal features can locally modify biological productivity (Alldredge and Hamner, 1980; Hamner and Hauri, 1981; Wolanksi and Hamner, 1988; Archambault, in prep.). Specifically, the work of Archambault (in prep) has shown that in several bays along the south shore of the St. Lawrence estuary, between Rimouski and Les Mechins, the biological productivity in a bay is higher than in the region just outside of the bay. It was hypothesized that this increased productivity in bays is due to an entrapment effect (Okubo, 1973), that serves to increase residence time of water-borne organisms in a particular region and hence to a subsequent increase in biomass and productivity (Okubo, 1980).

This study explores this hypothesis by describing the flow field in and around a bay on the south shore of the lower St. Lawrence estuary, L'Anse du Petit Mitis. This bay is the largest of the five bays used by Archambault (in prep). The following section is a brief review of previous studies of tidal flow

around coastal features. Chapter two will be used to describe the study area in some detail. Chapter three includes a description of the field methods used, as well as techniques used to analyze the data. Chapter four will be a presentation of results. A discussion and interpretation of results will be given in Chapter five.

1.1 Tidal flow around coastal features

In coastal areas, water motion is primarily controlled by tidal forces. Interactions between water movements and bottom topography become more complex and non-linear as the water column becomes shallower. As such, the sub-tidal transport properties of near-shore water can be very different than those of nearby deeper water, even though the mean velocity fields are similar. The tidal current along the south shore of the lower St. Lawrence estuary is sometimes an order of magnitude greater than the mean eastward flow due to the outflow of the Saguenay and St. Lawrence Rivers (El-Sabh, 1979). The interaction between tidal flows and bottom topography can create a flow field that is highly variable, both in space and time. Spatial and temporal variability of a flow field can enhance sub-tidal transport properties such that the net drift of a passive tracer can be quite different than that caused by a flow field with the same mean currents but with no spatial or temporal variability .

Much work has been done on the subject of oscillatory tidal flow around coastal features such as natural promontories, piers, islands, and bays (Pingree and Maddock, 1977, 1979, 1985; Pingree, 1978; Wolanski *et al.*, 1984; Ingram and Chu, 1987; Geyer and Signell, 1990; Signell and Geyer, 1991, Foreman *et al.*, 1992). An accurate description of tidal flow along a complex coastline is difficult as the flow is unsteady and highly non-linear. This problem has been approached using several different techniques, such as field studies, numerical modelling, and theoretical modelling. The following is a brief review of studies dealing with oscillatory flows around obstructions, beginning with observations of flow around promontories and islands, followed by physical explanations of the observed phenomena. Finally there will be a discussion about sub-tidal transport of water-borne material in tidal flows around headlands.

1.1.1 Observational studies

Wolanski *et al.* (1984) described the flow field around Rattray Island, an island 0.3 by 1.5 km that is oriented perpendicular to the tidal flow, using 24 current meters, radar, and aerial photography. They found that an eddy formed in the lee of the island during each half cycle of the semi-diurnal tide. The circulation pattern of the eddy led to a phase advance of the M_2 tide, as well as a strong Eulerian mean flow towards the tip of the island. The large

scale characteristics of the eddy, as shown in the aerial photographs, resembled those found in the lee of a flat plate in two dimensional flow at a Reynolds number of 10. The current speeds within the eddy were found to be of the same order of magnitude as the free-stream current speed. In steady-state flows, current speeds within an eddy are 1% of that found in the free-stream (Keller and Niewstadt, 1973). This increased recirculation speed may be due to the "start-up" eddy effect (Signell and Geyer, 1991) which will be described in more detail later.

Ingram and Chu (1987) studied the wakes behind 16 islands in Rupert Bay, Canada. The area is very shallow, about 3 m deep, and as such the bottom friction is thought to have a strong effect in controlling the flow. Using aerial photographs they described the wake structures in the lee of the islands. A zone of "dead water" with low turbulence and low sediment suspension was found downstream of islands with an extent perpendicular to the flow greater than 600 m. Unfortunately, there was no direct current data collected in the lee of the islands, and the structure of any recirculation downstream of the islands is difficult to assess as the pictures presented do not include a large enough extent. As with Wolanski *et al.* (1984), Ingram and Chu (1987) did not include any time dependence of the flow in their analyses even though the flow are predominantly tidal.

Geyer and Signell (1990) described the formation of an eddy in the lee of a headland, Gay Head, Massachusetts, using data from a shipboard acoustic doppler current profiler (ADCP). It was found that the M_2 tide was dominant and that tidal ellipses were roughly aligned with the isobaths, while tidal phase decreased towards the shore and especially towards the lee of the headland. These near-shore phase advances were attributed to the eddy's structure adding extra inertia to the return tide, but may also be due to the bed friction increasing shoreward. Bottom friction gradients can create eddy structures, known as phase eddies, even along a straight coastline (Black and Gay, 1987). Shallow water flows have less inertia than deep water flows and thus can follow the tidal forcing with less phase lag (Black and Gay, 1987). The eddy, as seen in a sequence of synoptic maps, begins as a small recirculation zone with high vorticity in the lee of the headland. This intense vorticity spreads out into the region downstream of the headland, leaving a large recirculating region at slack tide with flow speeds of the same order of magnitude as the free-stream flow, as seen by Wolanski *et al.* (1984).

1.1.2 Physics of transient eddy dynamics

One of the first comprehensive analyses of eddy formation in the lee of a headland in a tidally dominated regime was a numerical modelling study of the flow around Portland Bill, United Kingdom, by Pingree and Maddock (Pingree

and Maddock, 1977, 1979; Pingree, 1978). Their primary interest was in describing the characteristics of the tidal as well as the Eulerian mean flow field. Using a simple analytic model, three mechanisms were found to create or destroy vorticity in the vicinity of a headland (Pingree and Maddock, 1979). These are: bed friction torque, caused by shoaling coupled with the depth dependence of the bed friction term; speed torque, produced by velocity gradients perpendicular to the mean flow and the non-linearity of friction; and dissipation due to bed friction. Vorticity is created at the tip of the headland by the bed friction torque and speed torque, and is then advected downstream of the headland. This advected vorticity leads to the formation of an eddy in the lee of the headland, which is then dissipated by bed friction. The presence of this eddy causes the flow in the lee of the headland to be counter to the offshore flow. Thus, when the offshore tide turns, the water in the lee of the headland will already have a "head start". This leads to a phase advance in this region, something which has been observed in other studies (Wolanski, 1984; Geyer and Signell, 1990; Kuo *et al.*, 1990). From an Eulerian average point of view, this "head-start" will result in a strong mean current towards the headland. Pingree and Maddock (Pingree and Maddock, 1977, 1979; Pingree, 1978), in their studies of eddy formation around Portland Bill, concentrated their efforts on explaining the Eulerian mean current and vorticity induced by

the tides, and how this would effect transport of sediments and pollutants. It is the Lagrangian mean current that controls transport, and as will be shown later, Eulerian mean tidal flows are not necessarily a good indicator of Lagrangian mean tidal flows, especially in a region where the tidal excursion length is comparable to the length scale associated with variability of the velocity field.

Robinson (1981) discusses in detail the mechanisms by which tidal flows can produce residual vorticity, and how this vorticity is dissipated. As well as the three mechanisms introduced by Pingree and Maddock (1979), Robinson (1981) discusses advection back and forth across a bank or sill, and horizontal eddy viscosity as sources and sinks of residual vorticity. Mean vorticity created by advection across a sill has been observed in many field and numerical studies (Loder, 1980; Pingree and Maddock, 1985; Foreman *et al.*, 1992). Residual vorticity generation by horizontal eddy viscosity is much weaker than that generated by bed friction in regions that shoal slowly to the shore (Signell and Geyer, 1991). Robinson (1981) also showed that vorticity can be advected away from the production area, but that it cannot be advected more than a tidal excursion length from the production area.

Signell and Geyer (Signell, 1989; Signell and Geyer, 1991) followed up their field study of Gay Head with a numerical modelling study of an ideal

headland, with a slowly shoaling coastline. They were able to reproduce the principle features of eddies in the lee of headlands, and gained some further insight into the formation and evolution of tide induced transient eddies. Their approach was different from previous studies in that they focused on the eddies that formed with every tidal cycle and not on the Eulerian mean circulation. They showed that in the absence of side boundaries, as is the case along coastlines where bottom topography shoals slowly, a coastal boundary layer is produced by bed friction torque that is larger than the classic side boundary layer created by horizontal viscosity (Signell, 1989). This coastal boundary layer is characterized as being a region of strong shear and vorticity. If there is an alongshore adverse pressure gradient, then the boundary layer will separate and inject its higher vorticity into the free-stream (Signell, 1989).

Signell and Geyer (1991) also showed that gyres formed in the lee of headlands by tidal flows are much more intense than those created by steady flows. This is due to the oscillatory nature of the tidal flows. In impulsively started flows in which there is boundary layer separation, the separated boundary layer rolls up on itself, concentrating the vorticity in a blob. In steady flows, this initial blob would then propagate downstream and a weaker steady-state recirculating flow would occupy the lee of the headland. In tidal flows an initial start-up eddy will form in the lee of a headland at every half

tidal cycle. Signell and Geyer (1991) showed that for a common range of tidal flows (M_2 dominated tides with an amplitude of 0.5-1.5 m s^{-1}, water depths of 10-40 m, and a drag coefficient of $2.5x10^{-3}$) a start-up eddy would form on the downstream side of the headland. This eddy would then be advected back across the headland with the return tide and another start-up eddy would form in the lee. The first eddy would have been considerably weakened by bed friction at this point and would not interact appreciably with the second eddy. By the time the tide has changed again, the first eddy would have dissipated and the cycle would continue.

1.1.3 Sub-tidal transport

Interaction of tidal flow with coastal features can lead to very complex residual circulations. When considering the net transport of water borne material over several tidal periods, it is the Lagrangian residual velocity field that is of interest. When the tidal excursion length is smaller than coastal features, the flow is only weakly non-linear and the Eulerian residual circulation will be representative of the Lagrangian residual field (Robinson, 1981). When the tidal excursion is of comparable or larger scale than the coastal features, the transformation from the Eulerian residual to the Lagrangian residual becomes analytically impossible (Zimmerman, 1979), and the tide induced Eulerian residual field is of little use in interpreting the mean

transport over several tidal cycles (Imasato, 1983).

Longuet-Higgins (1969) showed, for time-varying flows, that the Eulerian mean velocity can be very different from the Lagrangian mean velocity. He termed this difference the Stokes velocity and estimated it to first order. Zimmerman (1979) showed that this approximation is invalid when the spatial scales of velocity variability are small compared with the advective length scales of oscillating flow. In order to make an Eulerian-Lagrangian transformation, the velocity field must be known at a resolution finer than the scale of velocity variability (Zimmerman, 1979).

Loder (1980) predicted that the existence of an Eulerian mean eddy does not imply the existence of a Lagrangian mean eddy, as the Stokes velocity may directly oppose the Eulerian residual velocity. This was found by Foreman *et al.* (1992), using a numerical model of the southwest coast of Vancouver Island, Canada. It was shown that a clockwise Eulerian mean eddy that forms over a shallow bank due to tidal rectification was more than cancelled by an anti-clockwise Stokes velocity, which resulted in a weak, anti-clockwise Lagrangian residual eddy.

2. Study area

2.1 The lower St. Lawrence estuary

The St. Lawrence estuary (figure 1) is the meeting place of the Atlantic Ocean and the St. Lawrence River. It begins at Quebec City, the landward limit of salt water intrusion and extends 400 km to Pointe des Monts, after which it becomes the Gulf of St. Lawrence. The estuary with its limits defined as such, has an area of 10 800 km^2. The estuary is divided naturally into an upper and a lower estuary by a sill 20 m deep that traverses the estuary near Tadoussac. The upper estuary is comprised of several disjointed channels and basins, with a maximum depth of 120 m. The lower estuary represents the beginning of the Laurentian Trough, a U-shaped channel typically greater than 300 m deep that extends through the Gulf of St. Lawrence to the continental shelf.

The St. Lawrence River accounts for 80% of the total fresh water input into the St. Lawrence estuary, with an annual average discharge at Quebec City of 11.9 x 10^3 m^3 s^{-1} (El-Sabh, 1988). Other major sources of fresh water into

the St. Lawrence estuary are the Saguenay River (9.9% of total fresh water input) and the north shore rivers; the Bersimis, the Outardes, and the Manicouagan (together 9.7% of total fresh water input) (El-Sabh, 1988). There is no significant fresh water input into the St. Lawrence estuary from the south shore. Total fresh water discharge up to Pointe des Monts varies from a minimum monthly mean of 13 x 10^3 m^3 s^{-1} in February to 23 x 10^3 m^3 s^{-1} in May.

Predominant winds are from the western quadrant, tending to follow the long axis of the estuary (Drapeau, 1990). Fetch increases downstream from Quebec City as the width of the estuary increases. During spring and summer, easterly wind events occur more frequently (Drapeau, 1990). Small bays and promontories protect near shore waters along the south shore from waves propagating along the long axis of the estuary. Only winds from the northern quadrant produce waves that enter into the small bays that line the south shore. Winds from the north-east have a fetch that extends well into the Gulf of St. Lawrence, and as a result produce the most energetic waves.

During the winter months there is ice in varying concentrations in the lower estuary. Ice in this region comes from 2 sources: ice that is advected downstream from the St. Lawrence River and the upper estuary; and ice that forms locally (El-Sabh, 1979). Ice begins to form in late November; by late

January most of the estuary is frozen over, and stays that way until late March. The highest concentrations of ice occur in the south shore region after mid-January. This is due to advection by prevailing wind and water currents, as well as the reduced salinity of this area.

The general surface circulation pattern of the lower estuary is characterized by the buoyant, fresh water outflow of the St. Lawrence and Saguenay Rivers along the south shore and two large recirculating gyres (El-Sabh, 1979). A smaller anti-clockwise gyre is situated between Ile du Bic and Tadoussac, and a larger clockwise gyre flows north at Ile du Bic, eastward along the north shore, south at Pointe des Monts, and completes its loop with a westward flow along the northern edge of the eastward flowing river discharge that hugs the south shore (El-Sabh, 1979).

The tides in the St. Lawrence estuary are semi-diurnal (Godin, 1979). The three main tidal constituents are M_2, S_2, and N_2 with periods of 12.42, 12.00, 12.66 hours respectively. The ratio between the M_2 and S_2 amplitudes of tide height (M_2/S_2) is 3.3 throughout the estuary (El-Sabh and Murty, 1990). Semi-diurnal and diurnal tides propagate as progressive waves from the Gulf of St. Lawrence into the estuary (Levesque, 1977). As tidal waves propagate upstream into the estuary, they face an ever decreasing cross-section and the amplitude of tidal height increases; from 93 cm at Les Mechins to 155

cm at Tadoussac (near the mouth of the Saquenay) for the M_2 constituent (Levesque, 1977; Godin, 1979). At Pointe au Père, just north-east of Rimouski, the M_2 constituent of tidal height is 126 cm (Defant, 1961).

2.2 L'Anse du Petit Mitis

L'Anse du Petit Mitis (figure 3) is a small bay on the downstream side of Pointe Mitis, a promontory that extends about 2 km offshore. It is situated approximately midway between Rimouski and Matane, and roughly 20 km downstream of Mont-Joli (figures 1 and 2). The bay is shallow, extending out to about the 15 m isobath. The shoreline is quite rocky and there are many small, rocky islets near the shore. The bay extends from the tip of Pointe Mitis to Les Boules, a pair of larger islets about three kilometres downstream. The bay is open to the estuary only to the north and north-east, thus it is sheltered from the prevailing westerly wind and waves. When the wind comes from the north-east, the effect is quite dramatic, as the fetch extends into the Gulf of St. Lawrence and large waves advance directly into the bay. The inner bay is split into two smaller bays. The south arm is shallow and drains at low tide. The north arm is deeper and does not drain at low tide. There is a colony of seals that spend their summer sunning on two small islets in the middle of the north arm.

3 Data collection and Analysis

3.1 Data collection

The primary data set consists of that collected by six Aanderaa recording current meters (RCM) moored at six different locations in and around L'Anse du Petit Mitis during the summer of 1994 (figure 3). Each RCM recorded water conductivity, temperature, speed and direction, as well as pressure. These data were used to calculate the east and north components of velocity, u and v respectively, water salinity and density, as well as the depth of the instrument. Specific information about each mooring (ie.: sampling interval, mooring duration, and distance of instrument from bottom) is listed in Table 1. The speed time series at station p1 was cut short due to a sea urchin finding its home in the rotor housing. The time series at p5 was cut short due to an entanglement of the mooring line. The depth time series at station p7 was cut short for unknown reasons.

The calibration accuracy of the instrument depth, as well as current speed and direction is listed in Table 1. An RCM consists of a CuNiSi alloy

and stainless, acid proof, epoxy coated steel pressure canister with an outside diameter of 128 mm and a height of 352 mm, counterbalanced on gimbals by a plastic vane. On top of the canister sit a rotor for measuring current speed, a conductivity cell for measuring water conductivity, a pressure sensor, and a thermistor. Power, circuitry, a compass, and data storage are all contained within the pressure canister. Paddle and not Savonius rotors where used on all six currentmeters. The rotor has a stall speed of 2 cm s^{-1}, and an accuracy of ± 1 cm s^{-1}. In regions of high wave activity, such as L'Anse du Petit Mitis during a northeast wind event, the error of the water velocity reading may be much larger than that quoted by Aanderaa. The vane has a stall speed of 2.5 cm s^{-1}, and the compass an accuracy of $\pm 5°$. At current speeds between 5 and 100 cm s^{-1} it is assumed that the vane follows the current perfectly and the only error is that due to the compass. At low (between 2.5 and 5 cm s^{-1}) and high (greater than 100 cm s^{-1}) current speeds, the vane does not line up perfectly with the current and the combined error is quoted by Aanderaa to be $\pm 7.5°$. While the resolution of the measured depths is 0.1% of full measurement range, the calibration accuracy is only 1% of full measurement range (Table 1). Calibrations of the RCM compasses, paddles, thermistors, conductivity cells, and pressure sensors were checked and found to be within the accuracy quoted by Aanderaa by Paul Peltola of the Department of

Atmospheric and Oceanic Sciences at McGill University.

Mooring configurations were of three types (see Table 1 for which mooring was of which type): tripod, L-type, and U-type. The tripod configuration (figure 4), used for the shallowest moorings inside the bay (p1 and p7), consisted of four aluminum legs, each 2 m long, and running flat along the bottom in a '+' type configuration. At the centre of the '+' was a 1 m long aluminum tube aligned perpendicular to the sea floor, atop of which was mounted the RCM. The L-type configuration (figure 5), used for medium depth moorings, consisted of a main mooring line on which the RCM was suspended. Two viny floats provided enough buoyancy to support the RCM and add tension to the line to keep it perpendicular. The main line was composed of two types of line: 1 inch (25 mm) diameter polypropylene rope being the bottom metre of line, to electrically isolate the mooring and to add flexibility to the mooring in the case of extreme storms; and the rest being 1/4 inch (6.5 mm) diameter stainless steel cable, to minimize drag. The electrical isolation was to minimize oxidation of the mooring assembly, which might lead to breakage of any of the various links, and subsequent loss of the mooring. The main line was held in place at the bottom by three 50 pound (23 kg) weights. A 100 m, 1/4 inch (6.5 mm) diameter, ground line was then stretched out across the bottom to a 50 pound (23 kg) weight. Small weights were

added to the ground line to prevent it from floating near the surface. The ground-line served two purposes: to aid in the deployment of the main mooring line; and for retrieval of the mooring at the summer's end. The U-type configuration (figure 6) was similar to that of the L-type configuration, except for the inclusion of an acoustic release. This configuration was used at stations p5 and p6. The acoustic release would allow for a 50 m, 1/4 inch diameter (6.5 mm) line attached to the 50 pound (23 kg) weight at the end of the ground line to be brought to the surface. This would allow for retrieval of the mooring in the event that the ground line could not be located. Neither acoustic release was released.

3.2. Data analysis

Data retrieval and analysis consisted of several steps. To begin with, data were retrieved from the storage modules of the RCM's; magnetic tape in the case of RCM4s' and solid state data storage units (DSU's) in the case of RCM7's. These data were then converted into ASCII format, and time series of east and north velocity components (u and v respectively), as well as temperature, salinity, density, and depth of the instrument were then calculated.

The velocity time series had their means and any linear trends removed

in order to prevent any contamination of the tidal signal in subsequent analyses. They were then broken down into three spectral components: low passed (frequencies less than 0.8 cycles per day, cpd); tidal band (frequencies between 0.8 and 6 cpd); and high passed (frequencies between 6 cpd and Nyquist; Table 1). The low passed signal was obtained by multiplying a linear ramp function with the Fourier transform of the time series (Walters and Heston, 1982). The ramp function had a value of one for all frequencies less than 0.6 cpd then decreased linearly to zero at a frequency of 0.8 cpd, and maintained a value of zero for all frequencies up to the Nyquist frequency. Finally, the low passed time series was subtracted from the detrended time series. This series was split into its tidal band and high passed components by using Fourier filter as before. This time the ramp function decreased linearly from one at 6 cpd to zero at 7 cpd.

3.2.1 Harmonic analysis

The tidal band time series were then subjected to a harmonic analysis. The harmonic analysis, consisted of a least squares fit of the time series to a summation of ten cosine functions with ten different known tidal periods known to be important in coastal waters (Table 2):

$$U = \sum_i u_i \cos(\frac{2\pi}{T_i} t - \delta_i) \qquad (1)$$

where the u_i's, T_i's and δ_i's are the amplitudes, periods and relative phase lags of the ten tidal constituents; U is the raw data time series and t is time. The u_i's and δ_i's were evaluated from equation 1 in a least squares sense by using the singular value decomposition (SVD) method. The resultant was amplitudes and relative phases for each tidal constituent for each time series. Here, relative phase refers to the phase lag with respect to the beginning of the time series. These phase lags were then converted to local Greenwich phase lags (g_i) at the eastern daylight savings time or 60° W time zone (Godin, 1972). Local Greenwich phase lag is the phase difference between the time of maximum tidal forcing (for example the passage of the moon overhead in the case of the M_2 tide) and the maximum tidal current.

The amplitudes and phases of the tidal analyses for u and v were then combined to create tidal ellipses (figure 7) for each tidal constituent. A tidal ellipse represents the magnitude and direction of the tidal currents throughout a tidal cycle, this is indicated as an imaginary vector pointing from the centre of the ellipse to the edge. The tip of this vector will trace the ellipse within one tidal cycle. The arrow on the perimeter of the ellipse indicates the direction of rotation. The local Greenwich phase lag is indicated as the angle measured, in the direction counter to that of the rotation of the vector, from the semi-major axis of the ellipse to the arrow indicating direction of rotation. This

convention is useful in that it also represents the magnitude and direction of the current at the local time of maximum tidal forcing.

Tidal currents can also be represented as a tidal excursion length. This is an integral over one half of a tidal cycle of the tidal velocities at one of the stations:

$$\Delta x = \int_{\frac{-T}{4}}^{\frac{T}{4}} U \cos(\frac{2\pi}{T} t) = \frac{UT}{\pi} \qquad (2)$$

where T is the period of a particular tidal constituent, and U is the tidal velocity amplitude. Physically, Δx is the horizontal distance a parcel of water would travel if it moved at the tidal velocity of a particular tidal constituent, and if there were no horizontal variation of the amplitude and phase of the tidal velocities.

3.2.2 Stokes drift calculation

The Stokes drift velocity as defined by Longuet-Higgins (1969) is the difference between the Lagrangian and Eulerian mean velocity. A first order approximation of the Stokes drift was derived by Longuet-Higgins (1969). A simplified derivation is shown here. Let M(x,y,t) be the Eulerian horizontal transport at a horizontal location (x,y) and time t, given by:

$$M(x,y,t) \equiv \int_0^{h(x,y,t)} u(x,y,z,t)\,dz \tag{3}$$

where h(x,y,t) is the total water depth, u(x,y,z,t) is the water velocity, and z is vertical distance from the sea floor. Let $\mathbf{u}_m$(x,y,t) be the transport velocity:

$$u_m(x,y,t) \equiv \frac{M(x,y,t)}{h(x,y,t)} \tag{4}$$

Separate both $\mathbf{u}_m$ and h into a mean and fluctuating part:

$$u_m = \overline{u_m} + u_m' \tag{5}$$

$$h = \overline{h} + h' \tag{6}$$

where $\overline{u_m}(x,y)$, the Eulerian mean velocity calculated as:

$$\overline{u_m}(x,y) = \frac{1}{T}\int_0^T u_m(x,y,t)\,dt \tag{7}$$

and

$$u_m' = u_m - \overline{u_m} \tag{8}$$

Equation 7 serves as a definition of the over-bar notation from here on. The variables $\overline{h}$ and h' are calculated as in equations 7 and 8. The Eulerian mean

transport, $\overline{M}$, can now be calculated as follows:

$$\overline{M} = \overline{u_m h} \tag{9}$$

$$\overline{M} = \overline{(\overline{u_m} + u_m')(\overline{h} + h')} \tag{10}$$

$$\overline{M} = \overline{u_m}\,\overline{h} + \overline{u_m' h'} \tag{11}$$

Dividing equation 11 by $\overline{h}$ gives:

$$\overline{u_{em}} = \overline{u_m} + \frac{\overline{u_m' h'}}{\overline{h}} \tag{12}$$

where $\overline{u_{em}}(x,y)$ is a first order approximation of the mean Lagrangian transport velocity, and $\frac{\overline{u_m' h'}}{\overline{h}}$ is considered to be a first order approximation of the Stokes drift velocity. Physically, this Stokes drift correction, accounts for transport due to the interaction between depth and velocity fluctuations at a particular location. For example, in a tidal region, both depth and velocity fluctuate sinusoidally; when both depth and velocity are in phase, high water corresponds with maximum eastward velocity, and low water corresponds with maximum westward velocity. In this case there will be more transport in the eastward than in the westward direction and the Stokes drift correction velocity

will be eastward. When water depth and velocity are 90° out of phase then the Stokes drift correction velocity will be zero.

3.2.3 Vertical velocity profiles

In order to calculate a Stokes drift correction velocity, a vertical velocity profile is required to calculate M. As the data set only provided current measurements at one depth at any given station, a vertical profile had to be assumed. The assumed vertical profile was a quadratic profile with no-slip and no-shear boundary conditions at the bottom and top boundaries respectively (Davies, 1987):

$$\mathbf{u}(x, y, z, t) = a(x, y, t) + b(x, y, t)z + cz^2$$

$$\mathbf{u}(x, y, 0, t) = 0$$

$$\frac{du(x,y,h,t)}{dz} = 0 \qquad (13)$$

where z is vertical height from the sea floor and $h(x,y,t)$ is the total water depth. If the instrument is located at a height z_0 above the bottom and $\mathbf{u}(z_0, t)$ is the recorded velocity at a location (x, y) and time t, then using equation 13:

$$a(x, y, t) = 0$$

$$b(x, y, t) = \frac{-2h(x,y,t)u(x,y,z_0,t)}{z_0^2 - 2h(x,y,t)z_0}$$

$$c(x, y, t) = \frac{u(x,y,z_0)}{-2h(x,y,t)z_0 + z_0^2} \tag{14}$$

Equation 3 can then be evaluated as:

$$M(x,y,t) = \int_0^{h(x,y,t)} bz + cz^2\, dz \tag{15}$$

$$M(x,y,t) = \frac{b}{2}z^2 + \frac{c}{3}z^3 \Big|_0^{h(x,y,t)} \tag{16}$$

$$M(x,y,t) = \frac{b}{2}h^2(x,y,t) + \frac{c}{3}h^3(x,y,t) \tag{17}$$

The appropriateness of the this assumed profile will be discussed in the next chapter.

3.2.4 Analysis of variance

Statistical variance of different components of the velocity time series were calculated. As previously mentioned, the velocity spectra were separated into three bandwidths: low passed, tidal, and high passed. The tidal band data had ten line spectra, corresponding to ten tidal constituent frequencies (Table 2), removed using harmonic analysis. Each of these spectral bands were then converted back to the time domain using an inverse Fourier transform. The

variance of each of these time series can be used to isolate the physical phenomena that are forcing the water motion. Low frequency physical forcing includes: variation of river run-off from the St. Lawrence and Saguenay; long period tidal components; and atmospheric forcing. High frequency physical forcing includes: wind and waves.

3.3 Bathymetry

The bathymetric map shown in figure 3 was constructed using data from two types of instruments: a Ross SL-600C chart recording depth sounder, using an acoustic beam of 103 kHz, with a 22° spreading angle; and a 4 beam broadband RDI Acoustic Doppler Current Profiler (ADCP), using an acoustic beam of 600 kHz, with a 20° spreading angle. Positioning was obtained using a Trimble Pathfinder Basic Plus Global Positioning System (GPS). Data were all reduced to Normal Low Tide, the marine chart datum used by the Canadian Hydrographic Service, using tide height information obtained from the RCM pressure data.

4. Results

The currents in and around L'Anse du Petit Mitis were found to have strong semi-diurnal tidal signal, as is evident in the power spectra of the velocity time series at each station (figure 8 a-f). Harmonic analysis results also reflect this dominance of the semi-diurnal signal, as the amplitudes of the semi-diurnal constituents (M_2, S_2, and N_2) are the largest of all the resolved constituent in the harmonic analysis(Table 3). This is true at all six mooring locations. Also, $\frac{K_1 + O_1}{M_2 + S_2}$ is less than 0.25 at all stations (Table 4). Generally, the tidal constituent amplitudes decreased from M_2 to S_2 to N_2, with S_2 and N_2 being of similar amplitude and M_2 being larger by factors ranging from 2.2 to 5.5, with one extreme value of 19.3 (Table 4). As the M_2 constituent is dominant, most of the following discussion will be about currents with a periodicity at the M_2 frequency.

4.1 M_2 tidal currents

At the four offshore stations (p4, p5, p6, and p8), the M_2 currents were

similar, but had differences due to the effects caused by the bay geometry. The M_2 tidal ellipses (figure 9) at stations outside of the bay (p4, p5, p6, and p8) are oriented alongshore with amplitudes on the order of 40 cm s^{-1}. The M_2 tidal ellipse at station p8 is very elongated, indicating that the predominant currents are in a direction parallel to the coastline. The M_2 amplitude here is the largest of all six locations. That the M_2 current at station p8 is more rapid than that at station p6 implies the possible formation of an M_2 tidal jet in this region: a tidal jet being defined here as a localized region with tidal currents faster than in the surrounding region. The jet's centre would be located somewhere between station p6 and the promontory. Tidal jet formation offshore of a promontory is consistent with theoretical and numerical predictions by Pingree and Maddock (1979), as well as observations by Geyer and Signell (1990). At station p6, the M_2 ellipse is more rounded, indicating less of a boundary effect due to the coast than at station p8. The M_2 amplitudes offshore of the promontory (p6 and p8) are about 10 cm s^{-1} greater than those downstream of the promontory (p5 and p4). This is consistent with the theoretical work of Pingree and Maddock (1979) who predicted maximal tidal flow offshore of a promontory with reduced flow in adjacent regions and bays. The M_2 currents at station p4 were the weakest of the four offshore stations possibly due to a combination of three things: the current meter being

nearest the bottom; the water depth being the shallowest.

The M_2 currents at the stations within the bay (p1 and p7) were significantly different than those outside of the bay, as well as being different from one another. The direction of rotation of the semi-diurnal tidal velocity vectors was clockwise outside of the bay (p4, p5, p6, and p8) and counterclockwise within the bay (p1 and p7; figure 9; Table 3). Within the bay, the M_2 currents were an order of magnitude weaker than those measured outside of the bay. The M_2 tidal ellipse at station p1 (figure 9) is almost circular and its semi-major axis is roughly perpendicular to the coastline downstream of the promontory. Although the M_2 Greenwich phase lag, g, at station p1 is about 65° greater then that at any of the other stations, its inclination is about 60° greater. Thus at the time of maximal tidal forcing, the currents at all of the stations are flowing in almost the same direction, approximately west southwest. At station p7, the M_2 tidal ellipse has an aspect ratio, phase and inclination similar to those at the stations outside of the bay, but with a smaller amplitude.

The tidal excursion length (figure 10) of the M_2 tide at the stations outside of the bay (p4, p5, p6, and p8) was of the same order as the alongshore extent of L'Anse du Petit Mitis. At the stations within the bay, the M_2 tidal excursion length is smaller than the bay, but as has been previously mentioned,

even within the bay there is variability of tidal currents. That the tidal excursion length at all stations is comparable to the spatial variability of the currents renders the determination of long term transport of water borne particles difficult or impossible to calculate without higher spatial resolution of the velocity field, as was discussed in section 1.1.3.

Further understanding of the tidal current regime is gained by examination of "snapshots" of the tidal currents throughout a tidal cycle (figure 11). At hour 8.97, during ebb tide, the currents at all six stations are roughly alongshore. This continues through the maximum ebb at hour 10.75. By hour 12.52, the direction of the flow in the bay (p1 and p7) has rotated northward, suggesting the existence of a phase eddy as described by Black and Gay (1987). By hour 14.3, during low slack tide, the currents have changed direction and are flowing westward or southwestward at all stations; flood tide has begun. Flood tide continues through hour 17.85, when the flow direction at station p1, within the bay, is changing; indicative again of a phase eddy. This is also evident at hour 19.62 when the currents at stations within the bay are flowing perpendicular to the shoreline downstream of the bay, and the currents at the stations offshore are still flowing roughly alongshore, but have begun to change direction from flood to ebb. Hour 19.62 has the same phase as hour 7.2 and thus the cycle continues.

4.2 Eulerian mean currents

Eulerian vector averaged currents (figure 12; table 5) are found to be an order of magnitude weaker than the amplitude of the M_2 tidal constituent, at every station except p1, where the magnitude of the mean current is 55% of the M_2 semi-major axis (Table 5). The mean currents (figure 12) at the offshore stations (p4, p5, p6, and p8) flow roughly eastward, in the same direction as the discharge from the St. Lawrence and Saguenay rivers. The mean current at station p8 appears to have been deflected northward by the promontory. The flow direction at station p1 suggests a recirculation within the bay forced by the mean offshore currents. As will be discussed later, the tidal dominance of the flow in this region makes it difficult to interpret the Eulerian mean current field.

4.3 Stokes drift correction velocity

The Stokes drift correction velocity (figure 13; Table 6) was calculated as described in section 3.2.2, using raw velocity and depth data, as well as the quadratic velocity profiles described in section 3.2.3. The depth data used was that provided by the RCM pressure sensors. Even with the poor accuracies quoted (section 3.1, table 1), at stations p1, p4, p5, and p6 the amplitude and phase of the M_2 tidal constituent (Table 7) compared reasonably well with the

estimates, 1.26 m and 78°, from the Pointe-au-Père tidal station (Defant, 1961). At stations p7 and p8 however, the M_2 amplitude was significantly reduced. Thus, the depth time series from stations p1 and p6 were used for the Stokes drift calculation at stations p7 and p8, respectively.

The Stokes correction velocity did not significantly modify the mean flow. The magnitude of the correction velocity was less than 12% of the mean velocity measured outside of the bay (p4, p5, p6 and p8) and about 20% of that measured inside the bay (p1 and p7)(Table 6). The small size of the Stokes correction velocity is not surprising since, at all stations but p1, the M_2 constituent of tidal height leads the M_2 constituent of velocity by 60 to 90° (Tables 7 and 3). As mentioned in section 3.2.2, a 90° phase difference between tidal depth and velocity leads to zero Stokes correction. At the inner stations, where the Stokes correction velocity is more significant, the tidal signal is much weaker with only about 20% of the velocity signal variance explained by the M_2 tidal constituent, and as such other components of the velocity may have contributed to creating a more significant Stokes correction velocity. Signal variance will be discussed further in a later section.

4.4 Vertical velocity profiles

While the Stokes correction velocity had a small effect on the Eulerian

mean velocity, the assumed velocity profiles had a pronounced effect (Table 6). At the stations inside of the bay, the magnitude of the depth averaged mean velocity was twice that of the mean velocity at the instrument depth (Table 6). Whereas, at stations outside of the bay, the mean of the depth averaged velocity ranged from 62 to 87% of the mean velocity at the instrument depth (Table 6). This effect is due to the characteristic shape of the assumed quadratic profile (figure 14) which has a large vertical shear near the bottom that gradually diminishes towards the surface. Therefore, if an instrument is moored near the bottom as they were at stations p1 and p7, the depth averaged velocity will be greater than the velocity measured by the instrument. Whereas, if the instruments are moored near the surface, as they were at stations p4, p5, p6 and p8 then the depth averaged currents will be less than that measured by the instrument. Thus, the assumed quadratic profile had the effect of augmenting the currents measured by the currentmeters within the bay and diminishing those measured by currentmeters outside of the bay. As the actual vertical velocity profiles are unknown, the quadratic profiles were used only for the Stokes correction calculation, and everywhere else the velocities shown are those measured at the instrument depth.

4.5 M_2 and its non-linear components; M_4 and the mean

Tidal flow in regions where bathymetry varies rapidly within one tidal excursion length can have strong non-linear components (Zimmerman, 1979). It has been previously mentioned that the tidal excursion length in the Anse du Mitis region is larger than the alongshore extent of Pointe Mitis, and therefore the non-linear components of the M_2 current, M_4 and the Eulerian mean, may play an important role in determining the nature of the flow in this region.

While the inclination of the M_4 tidal ellipses (figure 15) is similar to that of the M_2 tidal ellipses, their amplitude and phase differ. Outside of the bay (p4, p5, p6, and p8) the ratio $\frac{M_4}{M_2}$ for the semi-major axis is about 0.1 (Table 4). Inside the bay, at stations p1 and p7 this ratio is about 0.4 and 0.2 respectively. The M_2 + M_4 tidal currents are little different than those of the M_2 tidal currents (figure 16); there are slight changes in the velocity amplitude, but the flow direction remains the same.

The Eulerian mean currents, though much smaller in amplitude than the M_2 tidal currents (Table 5), have a significant effect on the flow at station p1. When the M_2, M_4 and Eulerian mean constituents are considered (figure 17) the flow direction at station p1 is seen to have turned from ebb to northward two hours prior (hour 10.75) to equivalent turning when only M_2 or M_2 + M_4 are considered. The current at p1 continues to flow northward faster and

longer (figure 17; hours 10.75, 12.52, 14.3, and 16.07) than that shown by only the M_2 or $M_2 + M_4$ currents. By hour 17.85, the current at station p1 has turned to flow alongshore in the westward direction. Within the next two hours, the flow at station p1 quickly turns from flood to ebb.

Even though the M_2 and M_4 constituents explain only 29% of the velocity variance at station p1, the salient features described by the $M_2 + M_4$ +Eulerian mean constituents (figure 17) are apparent in the raw data (figure 18). There is a phase advance of the tidal cycle in the raw data during the period shown (figure 18) with respect to the reconstructed M_2 currents shown in figures 11, 16, and 17. This is likely due to the effects of other tidal constituents. Also, as will be discussed in the following section, there is significant variability of the M_2 amplitude at stations within the bay, and the flow does not always follow that described by the currents reconstructed from the harmonic analysis of the entire time series.

4.6 Analysis of variance

The velocity time series were broken up into the three band widths, low, tidal, and high, as discussed in section 3.2. As well, the tidal band had ten line spectra removed at ten tidal frequencies (Table 2). The variance of the velocity time series associated with different spectral band widths was calculated and

expressed as a percentage of the variance of the raw signal (Table 8). There was proportionately more variance at high frequencies within the bay, 14 to 20%, than outside of the bay, 1 to 12%. Also, outside of the bay, the eastward (u) component of velocity had weak variance, 1 to 3% at the high frequencies. At low frequencies, the percent variance was similar amongst all of the stations (5 to 15%). Outside of the bay, most, 50 to 75%, of the total variance was at the ten tidal frequencies (Table 2) with 40 to 65% at the M_2 frequency. Inside of the bay, about 30% of the total variance was at tidal frequencies, with 20 to 30% at the M_2 frequency. Interestingly, most of the variance (35 to 40% of total variance) at stations p1 and p7 is within the tidal band, but not at tidal frequencies. This is possibly due to the shallowness of the bay, as well as the slow water motion within the bay. Because the interior of the bay is shallow, interaction between water and bathymetry, through friction and velocity advection can distort the tidal signal. Since the currents in the bay are generally weak, less than 5 cm s^{-1} 59% of the time at station p1, the tidal signal does not stand out very high above the background noise. As well, the RCM's are not able to follow changes in the currents very well at such low velocities. This will be further discussed in section 5.1.

In order to further understand the source of the variance in the tidal band that is not at tidal frequencies, a harmonic analysis was run on 2 day

segments of the velocity time series at stations p1 and p7. Since the segments were so short, only the M_2, K_1, M_4, MK_3 and M_6 constituents were resolved. It was assumed that the S_2 and N_2 constituents were included in the M_2 estimate and that the O_1 constituent was included in the K_1 estimate. It was found that there was considerable variability in both the harmonic analysis results and the percent variance explained by the harmonic analysis (figures 19, 20, and 21). While the M_2 amplitude and phase (figures 19 and 20, respectively) fluctuated almost evenly about the value obtained by a harmonic analysis of the entire signal, the percent variance attributed to the tidal constituents (figure 21) was generally greater than that obtained by a harmonic analysis of the entire time series. The percent variance and M_2 amplitude time series appear well correlated (figure 22), and the following comparisons will refer only to the percent variance time series.

Since the S_2 constituent is not resolved in the calculation of the percent variance and M_2 amplitude time series, a spring-neap modulation is expected. Comparison of the percent variance time series with the spring-neap modulation of the depth tidal signal at station p4 (figure 23) shows that while low values of percent variance do sometimes correspond with neap tides, there is no clear relation between the two.

Another physical factor that may decrease percent variance as well as M_2

amplitude is the wind. As mentioned in section 2.2, wind from the north-east quadrant has the effect of creating large swells that enter into the bay. Hourly wind readings were obtained from the nearby Mont-Joli airport. These were smoothed using a 24 hour running mean and compared with the percent variance time series at stations p1 and p7 (figure 24). Three northeasterly wind events occurred during the time that the RCM at station p7 was moored. These are: JED 181-183, 187-189, and 205-207. While the only values of percent variance that are below the global percent variance (JED 184 and 190), for the eastward (u) velocity component at station p1, occurred just one day after the first two northeasterly wind events, there is no such correlation with that at station p7. As well, the only values of percent variance that are below the global percent variance (JED 214 and 226), for the eastward (u) velocity at station p7, do not occur at times related to northeasterly wind events. While winds likely do have an effect on the circulation in the bay, a relation between the two is unclear.

4.7 Comparison with a numerical model

A numerical simulation of M_2 forced currents around Pointe Mitis (figure 25) was produced by van der Baaren *et al.* (1995). The model was run during the 1994 summer field season at L'Anse du Petit Mitis, and as such

none of the currentmeter data was used to calibrate the model. The model results show a surface flow field significantly faster than that observed, but still exhibited some of the salient features of the flow field that are implied by the RCM data (figures 17 and 18). While there is no boundary layer separation during flood (figure 25 b), there is a weak, anti-clockwise rotating gyre within the bay at high slack tide (figure 25 c). This weak gyre may be a phase eddy caused by the bed friction gradient of this shoaling region (Black and Gay ,1987). The flow is found to recirculate within L'Anse du Petit Mitis soon after the commencement of ebb tide (figure 25 d). This recirculating region grows to include the entire bay by maximum ebb (figure 25 e). Recirculation continues until after low slack tide (figures 25 a and b). The eddy tide induced transient eddy formed during ebb tide does not appear to extend offshore further than Pointe Mitis, which is contrary to that found in other similar studies (Pingree and Maddock, 1979; Geyer and Signell, 1990; Signell and Geyer, 1991).

The vorticity of this surface flow field (figure 26) reveals some of the same dynamics of the evolution of a tide induced residual circulation. Notably, there is a small region of strong negative vorticity at the tip of Pointe Mitis early in the ebb tide (figure 26 d). This small blob of vorticity is seen to advect into the bay region and diffuse into a large blob encompassing most of the bay

(figures 26 e and f) by low slack tide. At maximum flood tide (figure 26 b) there are no remaining traces of this eddy.

4.8 Comparison with ADCP data

Acoustic Doppler Current Profiler (ADCP) data were collected at L'Anse du Petit Mitis during July and August of 1995 (Bang, Laval, and Ingram unpublished data). Data from two different ship tracks, collected between July 27th and August 2nd (JED 206-213), were combined to create synoptic maps of M_2 and M_4 tidal ellipses (figures 27 and 28), as well as the Eulerian mean velocity (figure 29). Data shown are those recorded along the ship tracks with no horizontal interpolation.

The M_2 tidal ellipses show a general decrease in amplitude towards the interior of the bay (figure 27), similar to that shown by the ellipses obtained from RCM data (figure 9). While anticlockwise rotating ellipses are clustered mostly in a large region east of the promontory, and clockwise rotating ellipses are to the north and east of that, there is no clear delineation between the two. The ellipses produced by the RCM data rotated anticlockwise at stations within the bay and clockwise at stations outside of the bay. At the time of maximal tidal forcing, the current at all locations is flowing towards the western

quadrant. This is something that is also evident in the RCM data.

The Eulerian mean flow field (figure 29) gives the impression of a clockwise rotating gyre in the region east of the promontory. This corresponds well with what is shown by the mean flow as measured by the RCM's (figure 12). North of the promontory however, there is a westward mean flow which gives the impression of a second anticlockwise rotating flow. No sign of this westward mean flow shows up in the mean velocities as measured by the RCM's at stations p6 and p8. This westward flow may be due to a low period variability of the current which was under-sampled by the short duration of the ADCP data (9 days). While some westward currents were recorded by the RCM's at the outer stations during the time ADCP sampling, the mean east-west current over the entire nine days was about 10 cm s^{-1} in the eastward direction at stations p5, p6 and p8 (figure 30).

The M_4 tidal ellipses are generally very weak, and become weaker within the bay (figure 28), similar to that shown in the RCM data (figure 15). There are no clear patterns in the phase, inclination, or in the direction of rotation of the ellipses. This lack of organization is also apparent in the RCM data.

5. Discussion

5.1 Tide induced transient eddies

Some distinct features of transient, non-linear boundary separation and recirculation that have been observed in field and in numerical modelling studies are: a phase advance of the dominant tidal constituent advance in the lee of the promontory or island (Pingree and Maddock, 1979; Wolanski *et al.*, 1984; Geyer and Signell, 1990; Kuo *et al.*, 1990); a strong Eulerian mean flow directed towards a point offshore of the tip of the promontory or island (Pingree and Maddock, 1977; Pingree, 1978; Pingree and Maddock, 1979; Wolanski *et al.*, 1984; Signell, 1989; Geyer and Signell, 1990; Signell and Geyer, 1991); recirculation velocities comparable in magnitude to the free stream flow (Wolanski *et al.*, 1984; Geyer and Signell, 1990); and a tidal jet that forms offshore of the tip of the promontory or island (Pingree and Maddock, 1979; Signell, 1989; Geyer and Signell, 1990; Signell and Geyer, 1991). The following is a comparison of these observed features to those observed at Pointe Mitis.

The presence of the recirculating eddy causes both the phase advance and the strong Eulerian mean current towards the tip. The phase advance occurs because the recirculation in the lee of the promontory changes the direction of the current in this region before the direction of the offshore tidal current changes. In effect, the current in a region just downstream of a promontory receives a "head-start" from the recirculation. The phase at station p1, in the bay, is 65° ahead of that at all of the other stations, including p7 which is also inside of the bay. The strong Eulerian mean current towards the tip of the promontory occurs when there is transient eddy formation on a particular side of a promontory only during one half of a tidal cycle; either ebb or flood. During the half cycle when there is no eddy formation, flow will be alongshore. During the half cycle when there is eddy formation, flow will be alongshore, opposing the flow in the previous half cycle until the eddy grows strong enough to reverse the flow in the lee of a promontory. Because of this premature reversing of the flow that occurs only during half of a tidal cycle, the current in this region will have a mean flow towards the promontory. At station p1, the Eulerian mean current is of the same order of magnitude as the M_2 current and is towards the promontory. The flow field constructed from the M_2 + M_4 + Eulerian mean constituents (figure 17) shows that the current at p1 rotated away from ebb up to 4 hours prior to that at any of the other

stations. The current at station p1 continued to flow towards the promontory for the remainder of the flood tide.

Tide induced transient recirculation with velocities of the same order of magnitude as the free-stream flow has been observed in the field as well as in numerical models (Wolanski *et al.*, 1984; Geyer and Signell, 1990; Signell and Geyer, 1991). However, the currents measured within L'Anse du Petit Mitis (stations p1 and p7) are an order of magnitude slower than those outside of the bay. This may be due to a combination of three factors: differences in shoaling at the different sites; strong bottom friction due to the shallowness of L'Anse du Petit Mitis; and the vertical position of the currentmeters at stations p1 and p7. The sea floor at both Rattray Island (Wolanski *et al.*, 1984) and Gay Head (Geyer and Signell, 1990) was flat at about 20 m, and then shoaled within a kilometre of the coast, whereas at L'Anse du Petit Mitis there is constant shoaling from the 40 m isobath to the shore (figure 2). The inner bay region, where stations p1 and p7 are located, is less that 5 m deep at LNT (Lowest Normal Tide, the chart datum used by the Canadian Hydrographic Survey). Neither Wolanski *et al.* (1984) nor Geyer and Signell (1990) collected data in water shallower than 10 m. The currentmeters at p1 and p7 were located 1 m above the bottom, whereas in Wolanski *et al.* (1984) the currentmeters were 5 m above the bottom, and Geyer and Signell (1990) used the vertical average of

ADCP profiles.

Another factor that may lead to the measurement of extremely weak tidal currents within the bay is poor instrument performance in such a slow current regime. Due to the slower currents within the bay, the M_2 amplitude as measured by the currentmeters may be smaller than that which actually occurs. The rotor used to measure current velocity has little inertia and follows current speed changes well, but in order to follow changes in current direction the entire instrument must swivel, and the entire currentmeter has significant inertia. Thus, when current speeds are low, such as during slack tides, the instrument may not be able to follow the direction change and may even stall until the currents reach a sufficiently high velocity (4-5 cm s^{-1}). This would lead to a distortion of the tidal signal which would tend to spread tidal energy to other frequencies and thus give a low estimate of tidal velocity. Surface gravity waves will have also affected observed data, especially at the shallow mooring locations within the bay. This effect should be pronounced during northeast wind events, but no obvious correlations were found between northeast wind events and flow velocity variance.

Another observed characteristic of tidal flows around promontories is a tidal jet that forms offshore of the promontory (Pingree and Maddock, 1979; Signell, 1989; Geyer and Signell, 1990; Signell and Geyer, 1991). That the M_2

tidal ellipse (figure 9) at station p8 has a larger semi-major axis and is more elongated than the ellipse at station p6, indicates the formation of an M_2 tidal jet whose maximum lies between p6 and the shore.

Interestingly, there appears to be an eastward flowing jet that shows up in the average current as well (figure 12). The mean current observed just offshore of symmetric headlands in models (Pingree and Maddock, 1979; Signell, 1989), and in the field (Geyer and Signell, 1990) is typically strong relative to the amplitude of the M_2 constituent, and oriented towards a point offshore of the tip of the promontory. While the Eulerian mean current (figure 12) just offshore of Pointe Mitis at stations p6 and p8 is strong, it is oriented perpendicular to the promontory. It is possible that the strong mean eastward flow that occurs at stations p6 and p8 is caused by the discharge of the St. Lawrence and Saguenay rivers. The strong mean flow at station p1 towards the promontory appears to have been caused by a tide induced transient eddy.

5.2 Sub-tidal transport

In order to determine the net transport of water borne material over several tidal cycles it is necessary to have some idea of the Lagrangian mean velocity field. As mentioned in section 1.1.3, an Eulerian mean velocity is only representative of a Lagrangian mean velocity field when the tidal excursion

length is smaller than any coastal features (Robinson, 1981), and the transformation from an Eulerian field to a Lagrangian field becomes analytically untractable when the tidal excursion length is comparable or larger than coastal features (Zimmerman, 1979).

In the case of L'Anse du Petit Mitis, the tidal excursion length (figure 10) of currents outside of the bay (stations p4, p5, p6, and p8) is comparable with the extent of the bay itself. As well, outside of the bay (stations p4, p5, p6, and p8) the tidal excursion length is comparable to the spatial scales of variability of the velocity field. This is especially evident at station p4, where at the two extremities of the tidal excursion the velocity characteristics are quite different. The eastern end of the tidal excursion at station p4, is very near to shore and shallow and thus the current there may be slower than at station p4. Likewise, at the western end of the tidal excursion, which lies inside the bay near station p1, the flow is much weaker. As water is advected to these regions its net displacement may be quite different than that given by the tidal excursion.

The tidal excursion length of currents within the bay is constrained by the bay, but there is spatial variability of the currents within the bay, as is shown by the differences of the flow at stations p1 and p7. Thus, even within the bay, where the tidal excursion length is small, the Eulerian mean plus the

Stokes correction velocity may be a poor estimate of the Lagrangian mean velocity.

In order to further address the question of sub-tidal residence times in this region, more extensive spatial coverage is required. This would include: more information regarding the definition of the seaward boundary of the bay, and a better idea of the fluxes across this boundary; as well as current velocity information at a spatial resolution small enough to be able to estimate the Lagrangian mean velocity field, or perhaps a direct look at Lagrangian velocities using drogued drifters. Other effects that might prove to be important in controlling residence time of water within L'Anse du Petit Mitis include: turbulent dispersion in the shallow regions of the bay; secondary currents created by the upstream end of Pointe Mitis; current patterns that are too large to be resolved by this study and too small to be resolved by studies of the entire lower St. Lawrence estuary; and an idea of the fate of water that leaves the bay, that is to say, how much of the water that leaves the bay during an ebb tide, returns during the following flood tide.

6. Conclusions

The flow downstream of Pointe Mitis shows the following characteristics that imply the formation of a transient eddy during ebb tide that strongly influences the current at station p1: the M_2 velocity phase just downstream of the promontory, at station p1 is approximately 65° ahead of that measured at the other five stations; the M_2 tidal ellipse at station p1 is oriented towards the promontory; the mean flow at station p1 is strong relative to the amplitude of the M_2 constituent and is oriented towards the promontory. The flow in the region downstream of Pointe Mitis is an order of magnitude weaker than that observed offshore of the promontory, possibly due to the shallowness of the region downstream of Pointe Mitis, as well as a sheltering effect of the downstream orientation of the promontory. Tide induced transient eddies do not appear to extend into L'Anse du Petit Mitis as far as station p7.

The first order Stokes drift correction velocity was found to be negligible. Since the M_2 tidal excursion length is of the same order as the scale of horizontal variability of the velocity field, the Lagrangian mean velocity field

may be considerably different than the Eulerian velocity field. If this is true then the first order Stokes drift correction may be a poor estimate of the actual Stokes drift, indicating that an estimate of the mean residence time of water within the bay is unattainable with the present data set.

While the present study was able to provide insight into the nature of the flow downstream of Pointe Mitis, it was not able to provide physical reasons as to why Archambault (in prep.) found that the region just downstream of Pointe Mitis held greater biological productivity than the surrounding regions.

References

Alldredge, A.L. and W.M. Hamner, 1980 Recurring aggregation of zooplankton by a tidal current. *Estuarine and Coastal Marine Sciences*. 10: 31-37

Archambault, P., The effect of coastal heterogeneity on the planktonic community. PhD thesis, in preparation, Université Laval, département de biologie.

Black, K.P., and S.L. Gay, 1987 Eddy formation in unsteady flows. *J. Geophys. Res.* 92(c9): 9514-9522

Davies, A.M., 1987 Spectral models in continental shelf sea oceanography. In: Coastal and Estuarine Sciences 4, N.S. Heaps (Ed.), Three-Dimensional Coastal Models. American Geophysical Union Washington, D.C., 71-105

Defant, A., 1961 Physical Oceanography, volume 2. Pergamon Press, New York, 598 p.

Drapeau, G., 1990 Nearshore sediment dynamics in the St. Lawrence estuary. In: Coastal and Estuarine studies, Vol. 39 M. I. El-Sabh, N. Silverberg (Eds.) Oceanography of a Large-Scale Estuarine System: The St.

Lawrence. Springer-Verlag, New York, inc., 130-154

El-Sabh, M.I., 1979 The Lower St. Lawrence Estuary as a physical oceanographic system. *Naturaliste Can.* 106: 44-73

El-Sabh, M.I., 1988 Physical Oceanography of the St. Lawrence estuary. In: Hydrodynamics of Estuaries, Vol., II (B. Kjerke, Ed.). CRC Press, 61-78

El-Sabh, M.I. and T.S. Murty, 1990 Mathematical modelling of tides in the St. Lawrence Estuary. In: Coastal and Estuarine studies, Vol. 39 M. I. El-Sabh, n. Silverberg (Eds.) Oceanography of a Large-Scale Estuarine System: The St. Lawrence. Springer-Verlag, New York, 10-50

Fischer, H.B., E.J. List, R.C.Y. Koh, J. Imberger, N.H. Brooks, 1979 Mixing in inland and coastal waters. Academic Press, Ltd., New York, 483 p.

Foreman, M.G.G., A.M. Baptista, R.A. Walters, 1992 Tidal model studies of particle trajectories around a shallow coastal bank. *Atmos.-Oc.*, 30(1): 43-69

Geyer, W.R. and R.P. Signell, 1990 Measurements of tidal flow around a headland with a shipboard Acoustic Doppler Current Profiler. *J. Geophys. Res.*, 95: 3189-3197

Godin, G., 1972 The analysis of tides. University of Toronto Press, Toronto and Buffalo, 264 p.

Godin, G., 1979 La marée dans le golfe et l'estuaire du St-Laurent. *Naturaliste can.*, 106: 195-121

Godin, G., 1988 Tides. Centro de Investigacion Cientifica y de Educacion Superior de Ensenada (CICESE). Ensenada, Baja California, MEXICO, 290 p.

Hamner, W.M. and I.R. Hauri, 1981 Effects of island mass: water flow and plankton pattern around a reef in the Great Barrier Reef lagoon, Australia. *Limnol. Oceanogr.* 26(6): 1084-1102

Imasato, N., 1983 What is tide-induced residual current? *J. Phys. Oceanogr.* 13: 1307-1317

Ingram, R.G., V.H. Chu, 1987 Flow around islands in Rupert Bay: An investigation of the bottom friction effect. *J. Geophys. Res.*, 92: 14521-14533

Keller, H.B., and F. Niewstadt, 1973 Viscous flow past circular cylinders. *Computers and Fluids*, 1: 59-71

Kuo, A.Y., R.J. Byrne, P.V. Hyer, E.P. Ruzecki, and J.M. Brubaker, 1990 Practical application of theory for tidal-intrusion fronts. *Journal of Waterway, Port, Coastal, and Ocean Engineering.*, 116: 341-361

Levesque L., 1977 Etude du modèle mathématique de la propagation des marées dans l'Estuaire du St. Laurent. MSc. Thesis, Souqar, UQAR,

161 p.

Loder, J. W., 1980 Topographic rectification of tidal currents on the sides of Georges Bank. *J. Phys. Oceanogr.*, 10: 1399-1416

Longuet-Higgins, M.S., 1969 On the transport of mass by time varying ocean currents. *Deep Sea Res.* 16: 431-447

Okubo, A., 1973 Effect of shoreline irregularities on streamwise dispersion in estuaries and other embayments. *Netherlands Journal of Sea Research.* 6(1-2): 213-224

Okubo, A., 1980 Diffusion and ecological problems: mathematical models. Springer Verlag, New York, inc., 254 p.

Pingree, R., 1978 The formation of the Shambles and other banks by tidal stirring of the seas. *J. Mar. Biol Ass. U.K.*, 58: 211-226

Pingree, R., and L. Maddock, 1977 Tidal eddies and coastal discharge. *J. Mar. Biol. Ass. U.K.*, 57: 869-875

Pingree, R., and L. Maddock, 1979 The tidal physics of headland flows and offshore tidal bank formation. *Marine Geology*. 32: 269-289

Pingree, R., and L. Maddock, 1985 Rotary currents and residual circulation around banks and islands. *Deep Sea Res.* 32: 929-947

Robinson, I., 1981 Tidal vorticity and residual circulation. *Deep Sea Res.*, 28A(3): 195-212

Signell, R.P., 1989 Tidal dynamics and dispersion around coastal headlands. Ph.D. Thesis, Woods Hole Oceanographic Institute and Massachusetts Institute of Technology, WHOI-89-38, Cambridge, MA. 162 p.

Signell, R.P., and W.R. Geyer, 1991 Transient eddy formation around headlands. *J. Geophys. Res.*, 96: 2561-2575

Therriault, J.-C. and M. Levasseur, 1985 Control of phytoplankton production in the lower St. Lawrence Estuary: light and freshwater run-off. *Naturaliste Can.* 112: 77-96

van der Baaren, A., J. Wang, and R.G. Ingram, 1995 A report on numerical simulations of tidal flow past a headland and within a small shallow bay: L'Anse du Petit Mitis. Bedford Institute of Oceanography internal report. 48 p.

Walters, R.A. and C. Heston, 1982 Removing tidal-period variations from time-series data using low-pass digital filters. *J. Phys. Oceanogr.* 12: 112-115

Wolanski, E. and W.M. Hamner, 1988 Topographically controlled fronts in the ocean and their biological influence. *Science.* 241: 177-181

Wolanski, E., J. Imberger, M.L. Heron, 1984 Island wakes in shallow coastal waters. *J. Geophys. Res.* 89(C6): 10553-10569

Zimmerman, J.T.F., 1979 On the Euler-Lagrange transformation and the

Stokes Drift in the presence of oscillatory and residual currents. *Deep Sea Res.* 26A: 505-520

Tables

Table 1. Mooring information. Nyquist frequency is given as cycles per day (cpd). LNT refers to lowest normal tide, the chart datum used by the Canadian Hydrographic Service. Instrument accuracy is a quoted by manufacturer. The error of the depth measurement is a function of the range of the particular sensor. The starting velocity for the rotor is 2 cm s^{-1}. The estimate of directional error has two ranges: low, 2.5 to 5 cm s^{-1}; and high 5 to 100 cm s^{-1}.

			Station					
			p1	p4	p5	p6	p7	p8
instrument			RCM7	RCM7	RCM7	RCM4	RCM4	RCM4
serial number			10761	10270	9174	8857	2906	8673
latitude (° N)			48° 40' 51.5"	48° 41' 36.9"	48° 42' 18.9"	48° 41' 35.0"	48° 40' 42.3"	48° 41' 21.1"
longitude (° E)			68° 00' 58.5"	67° 58' 50.1"	67° 59' 58.0"	68° 02' 44.3"	68° 01' 19.2"	68° 01' 56.3"
mooring type			tripod	L-type	U-type	U-type	tripod	L-type
sampling interval (min)			10	10	10	10	15	15
Nyquist frequency (cpd)			72	72	72	72	48	48
record length (days)			37.4	48.4	38.4	43.4	62.5	62.5
distance of instrument from bottom (m)			1	7.5	12	12	1	9.4
total water depth with respect to LNT (m)			4	10	20	20	17	14.7
Accuracy	depth (m)		±3.5	±1.4	±1.4	±3.5	±1.4	±3.5
	speed (cm s^{-1})		±1	±1	±1	±1	±1	±1
	dir	low	±7.5°	±7.5°	±7.5°	±7.5°	±7.5°	±7.5°
		high	±5°	±5°	±5°	±5°	±5°	±5°

Table 2. List of tidal constituents used in tidal analysis (Godin, 1988). cpd refers to cycles per day.

Symbol	Frequency (cpd)	Period (solar hours)	Description
M_2	1.9323	12.4206	principal lunar semi-diurnal
S_2	2.0000	12.0000	principal solar semi-diurnal
N_2	1.8960	12.6583	due to monthly variations in moon's distance from earth
K_1	1.0027	23.9345	soli-lunar diurnal; due to variations in declination of orbits of sun and moon
M_4	3.8645	6.2103	quarter-diurnal; caused by the doubling of the M_2 frequency due to interaction with itself through non-linear advection
O_1	0.9295	25.8193	principal lunar diurnal
M_6	4.1402	5.7968	one sixth diurnal; caused by the tripling of the M_2 frequency due to interaction with itself through bottom friction
MK_3	8.1771	2.9350	one third diurnal; caused by interactions between the M_2 and K_1 constituents through non-linear advection
S_4	4.0000	6.0000	quarter-diurnal; caused by the doubling of the S_2 frequency due to interaction with itself through non-linear advection
MN_4	3.8283	6.2692	quarter-diurnal; due to interactions between M_2 and N_2 through non-linear advection

Table 3. Harmonic analysis of velocity for all ten tidal constituents at all six stations. U and V are eastward and northward velocity components respectively. Amp is the tidal constituent amplitude in cm s^{-1}. Local Greenwich phase lag is given as g, in degrees. Local time refers to Greenwich mean time minus four hours. M and m are the amplitude of the semi-major and semi-minor axes of a tidal ellipse, given in cm s^{-1}. A negative m represents clockwise rotation of the velocity vector. Inc is the angle measured clockwise from east to the semi-major axis of a tidal ellipse.

Station	Constituent	u		v		M	m	inc	g
		amp	g	amp	g				
p1	M_2	2.7	125.0	2.3	231.4	2.9	2.1	-28.6	103.8
p1	S_2	0.8	212.9	1.0	284.7	1.1	0.7	67.1	-90.5
p1	N_2	0.5	44.4	1.1	215.4	1.2	0.1	-66.4	36.9
p1	K_1	0.4	122.4	0.1	355.5	0.4	-0.1	-8.4	123.9
p1	M_4	0.8	160.4	0.9	315.8	1.2	0.3	-48.2	146.8
p1	O_1	0.3	12.5	0.3	265.0	0.4	-0.3	-44.2	48.0
p1	M_6	0.4	229.0	0.1	70.4	0.4	0.0	-13.5	-129.8
p1	MK_3	0.3	211.0	0.2	101.6	0.3	-0.1	-13.9	-142.0
p1	S_4	0.2	185.9	0.3	304.9	0.3	0.1	-47.7	139.0
p1	MN_4	0.4	123.7	0.5	283.9	0.6	0.1	-48.9	112.5
p4	M_2	24.9	180.1	10.0	164.5	26.7	-2.5	21.5	178.0
p4	S_2	5.6	214.6	2.4	211.3	6.1	-0.1	22.8	-145.9
p4	N_2	4.3	133.3	1.5	117.8	4.5	-0.4	18.8	131.6
p4	K_1	3.3	246.5	0.5	259.2	3.4	0.1	8.8	-113.2
p4	M_4	2.4	338.2	1.3	303.6	2.6	-0.7	26.2	-29.0
p4	O_1	1.9	195.9	0.7	213.8	2.0	0.2	20.0	-162.0
p4	M_6	0.5	120.5	0.5	94.2	0.7	-0.2	48.5	105.8
p4	MK_3	2.1	88.7	1.0	36.8	2.2	-0.8	18.6	82.1
p4	S_4	0.9	49.2	0.3	313.9	0.9	-0.3	-2.0	49.9
p4	MN_4	0.7	321.9	0.4	228.2	0.7	-0.4	-3.2	-36.2

Table 3 continued: tidal analysis results

Station	Constituent	u		v		M	m	inc	g
		amp	g	amp	g				
p5	M_2	30.9	191.2	9.3	165.6	32.0	-3.9	15.5	-170.7
p5	S_2	8.3	244.2	3.7	230.4	9.1	-0.8	23.8	-118.1
p5	N_2	6.7	146.5	1.5	118.6	6.9	-0.7	11.2	145.4
p5	K_1	4.4	283.1	0.7	319.8	4.4	0.4	7.3	-76.2
p5	M_4	3.3	9.7	1.0	326.1	3.4	-0.7	13.3	6.9
p5	O_1	2.0	249.6	1.3	292.6	2.3	0.8	29.9	-99.0
p5	M_6	0.6	213.1	0.7	165.1	0.8	-0.4	46.8	-172.2
p5	MK_3	2.5	88.1	0.6	1.3	2.5	-0.6	0.7	-88.0
p5	S_4	1.0	81.3	0.6	266.3	1.2	0.0	-27.7	-82.4
p5	MN_4	1.5	319.0	0.6	250.4	1.6	-0.5	8.6	-43.9
p6	M_2	37.7	174.0	21.7	159.8	43.2	-4.6	29.6	170.5
p6	S_2	10.8	207.9	6.5	197.3	12.6	-1.0	30.9	-154.9
p6	N_2	6.3	132.2	3.6	122.6	7.3	-0.5	29.2	129.9
p6	K_1	5.3	263.8	1.7	271.5	5.5	0.2	17.9	-95.5
p6	M_4	4.7	308.9	2.5	255.1	5.0	-1.9	20.3	-59.1
p6	O_1	1.5	210.6	1.3	228.7	1.9	0.3	40.4	-141.8
p6	M_6	0.5	102.5	0.4	76.5	0.6	-0.1	35.9	93.4
p6	MK_3	3.1	46.1	1.8	20.3	3.5	-0.7	28.0	40.3
p6	S_4	1.2	54.4	0.9	355.9	1.3	-0.7	29.3	38.4
p6	MN_4	1.8	258.6	0.3	261.1	1.8	0.0	9.1	-101.4

Table 3 continued: tidal analysis results

Station	Constituent	u		v		M	m	inc	g
		amp	g	amp	g				
p7	M_2	2.8	156.2	2.6	187.5	3.7	1.0	42.7	170.6
p7	S_2	0.9	231.8	0.5	282.7	1.0	0.3	20.2	-120.9
p7	N_2	0.5	192.5	0.7	202.9	0.9	-0.1	58.5	-160.0
p7	K_1	0.3	243.8	0.2	278.3	0.3	0.1	29.8	-107.3
p7	M_4	0.6	124.5	0.2	328.1	.0.7	-0.1	-19.4	127.2
p7	O_1	0.4	305.5	0.3	275.2	0.5	-0.1	-38.2	-66.2
p7	M_6	0.1	299.6	0.1	81.8	0.2	0.0	-75.1	-95.4
p7	MK_3	0.2	228.1	0.2	175.6	0.2	-0.1	45.6	-158.6
p7	S_4	0.1	169.2	0.0	121.7	0.1	0.0	20.6	162.3
p7	MN_4	0.1	102.7	0.1	144.9	0.2	0.1	38.7	119.5
p8	M_2	45.4	170.5	10.3	160.5	46.5	-1.8	12.7	170.0
p8	S_2	8.8	214.1	2.2	204.6	9.1	-0.4	13.8	-146.4
p8	N_2	7.8	120.5	1.4	115.5	7.9	-0.1	10.3	120.3
p8	K_1	5.6	262.0	2.2	278.0	6.0	0.6	20.6	-96.0
p8	M_4	4.5	303.6	1.8	332.5	4.7	0.8	19.6	-52.9
p8	O_1	3.7	196.4	1.6	228.4	3.9	0.8	21.4	-159.1
p8	M_6	1.2	112.5	0.4	116.6	1.3	0.0	18.4	112.9
p8	MK_3	4.0	51.3	1.4	46.9	4.2	-0.1	18.7	50.9
p8	S_4	0.5	106.9	0.4	193.8	0.5	0.4	11.7	117.1
p8	MN_4	1.6	273.1	0.9	266.7	1.9	-0.1	29.6	-88.4

Table 4. Comparisons of velocity tidal constituent amplitudes. All values are given in cm s^{-1}.

Station		p1	p4	p5	p6	p7	p8
$\frac{O_1 + K_1}{S_2 + M_2}$	u	0.19	0.17	0.16	0.14	0.19	0.17
	v	0.12	0.1	0.15	0.11	0.17	0.3
	M	0.18	0.16	0.16	0.13	0.18	0.18
	m	0.12	0.12	0.26	0.09	0.16	0.64
$\frac{M_2}{S_2}$	u	3.6	4.4	3.7	3.5	3	5.1
	v	2.2	4.3	2.5	3.3	5.5	4.7
	M	2.7	4.4	3.5	3.4	3.8	5.1
	m	3.0	19.3	4.8	4.5	3.1	5.0
$\frac{M_4}{M_2}$	u	0.30	0.10	0.11	0.12	0.22	0.10
	v	0.39	0.13	0.11	0.11	0.09	0.17
	M	0.41	0.10	0.11	0.11	0.18	0.10
	m	0.13	0.27	0.18	0.41	0.09	0.45
$\frac{(mean)}{M_2}$	u	0.40	0.13	0.13	0.14	0.14	0.14
	v	0.51	0.03	0.11	0.04	0.17	0.33

Table 5. Comparison of Eulerian mean current to M_2 current amplitudes. U is the current magnitude ($\sqrt{u^2 + v^2}$). Mean velocities and M_2 amplitudes are given in cm s^{-1}.

station #		p1	p4	p5	p6	p7	p8
mean	u	-1.10	3.13	4.14	5.12	-0.40	6.32
	v	-1.15	-0.34	1.03	-0.79	-0.45	3.41
	U	1.59	3.15	4.26	5.18	0.61	7.18
M_2	u	2.73	24.85	30.85	37.65	2.81	45.35
	v	2.28	10.04	9.34	21.71	2.62	10.32
	M	2.90	26.68	31.99	43.21	3.70	46.47
	m	2.06	2.51	-3.90	4.63	1.04	-1.76
$\frac{(mean)}{M_2}$	u	0.40	0.13	0.13	0.14	0.14	0.14
	v	0.51	0.03	0.11	0.04	0.17	0.33
	U	0.55	0.12	0.13	0.12	0.16	0.15

Table 6. Eulerian mean recorded velocity, $\bar{u}(x,y,z_0)$, mean transport velocity, $\overline{u_m}(x,y)$, Stokes correction velocity, $\frac{\overline{u_m' h'}}{\bar{h}}$, and Stokes correction + mean transport, $\overline{u_{cm}}(x,y)$. U is the velocity magnitude, u and v are the east and north velocity components respectively. Velocities are in cm s^{-1}.

station #		p1	p4	p5	p6	p7	p8
recorded	u	-1.10	3.13	4.14	5.12	-0.40	6.32
	v	1.15	-0.34	1.03	-0.79	-0.45	3.41
	U	1.59	3.15	4.26	5.18	0.61	7.18
transport	u	-2.67	2.45	3.58	3.45	-0.81	3.87
	v	2.21	-0.20	0.94	-0.51	-0.81	2.26
	U	3.47	2.46	3.70	3.49	1.15	4.48
Stokes	u	0.42	0.10	0.04	0.26	0.11	0.42
	v	-0.53	0.12	0.10	0.34	-0.21	0.17
	U	0.68	0.16	0.11	0.43	0.24	0.45
transport + Stokes	u	-2.25	2.55	3.62	3.71	-0.70	4.29
	v	1.69	-0.07	1.04	-0.18	-1.02	2.43
	U	2.81	2.55	3.77	3.71	1.24	4.93
$\frac{Stokes'}{transport}$	U	0.20	0.07	0.03	0.12	0.21	0.10
$\frac{transport}{recorded}$	U	2.18	0.78	0.87	0.67	1.89	0.62

Table 7. Harmonic analysis of total water depth for all ten tidal constituents at all six stations. Tidal amplitude is given in metres. Local Greenwich phase lag, g, is given in degrees. Local time refers to Greenwich mean time minus four hours.

Amplitude (m)

Station	p1	p4	p5	p6	p7	p8
M_2	1.22	1.15	1.14	1.26	0.81	0.53
S_2	0.32	0.35	0.38	0.38	0.24	0.22
N_2	0.24	0.22	0.24	0.23	0.22	0.15
K_1	0.25	0.24	0.28	0.28	0.04	0.19
M_4	0.01	0.00	0.05	0.05	0.21	0.02
O_1	0.19	0.20	0.28	0.21	0.05	0.15
M_6	0.01	0.02	0.07	0.04	0.04	0.04
MK_3	0.00	0.00	0.02	0.03	0.01	0.04
S_4	0.00	0.00	0.02	0.02	0.02	0.01
MN_4	0.00	0.01	0.01	0.02	0.03	0.01

g (degrees)

Station	p1	p4	p5	p6	p7	p8
M_2	88.91	90.94	100.06	88.33	108.04	108.54
S_2	133.25	134.37	143.48	137.02	145.68	151.04
N_2	53.81	61.61	65.86	63.94	59.30	85.64
K_1	233.32	242.66	250.34	242.97	241.96	255.36
M_4	114.81	180.86	0.40	313.20	179.36	308.77
O_1	202.11	204.84	208.40	202.59	213.07	209.39
M_6	148.99	74.43	118.32	75.33	128.27	146.04
MK_3	280.51	297.63	47.58	92.80	339.37	38.40
S_4	229.96	74.45	105.61	25.07	294.14	216.67
MN_4	12.50	27.90	0.60	298.96	183.48	209.55

Table 8. Velocity signal percent variance attributable to various frequencies. The velocity spectrum was broken into three bandwidths: low, frequencies less than 0.8 cycles per day (cpd); tidal, frequencies between 0.8 and 6 cpd; and high, frequencies between 6 cpd and the Nyquist frequency. A harmonic analysis was performed on the tidal band velocity time series and line spectra corresponding to 10 tidal constituent frequencies were removed. Statistical variance as a percentage of the statistical variance of the original velocity time series is presented for the east and north components of velocity, u and v respectively. Within the tidal band, tidal refers to the percent variance of the tidal frequencies, and non-tidal refers to the percent variance of the remaining signal (ie: that which is left after the harmonic analysis).

station			p1	p4	p5	p6	p7	p8
low		u	9.70	13.50	9.27	6.78	13.61	7.58
		v	6.49	9.65	8.87	6.44	9.23	4.96
tidal band	all 10 tidal constituents	u	33.94	62.21	72.67	76.32	31.95	72.35
		v	30.52	60.61	52.64	70.03	34.62	55.75
	M_2 only	u	27.08	58.50	61.99	66.04	26.57	69.92
		v	19.47	57.78	41.11	60.78	29.20	47.27
	remainder	u	40.00	20.93	15.87	15.02	35.50	18.50
		v	40.26	20.66	28.40	19.07	39.23	25.66
high		u	18.94	2.61	1.85	1.58	14.79	1.23
		v	19.48	8.29	9.06	4.05	16.15	11.77

Figures

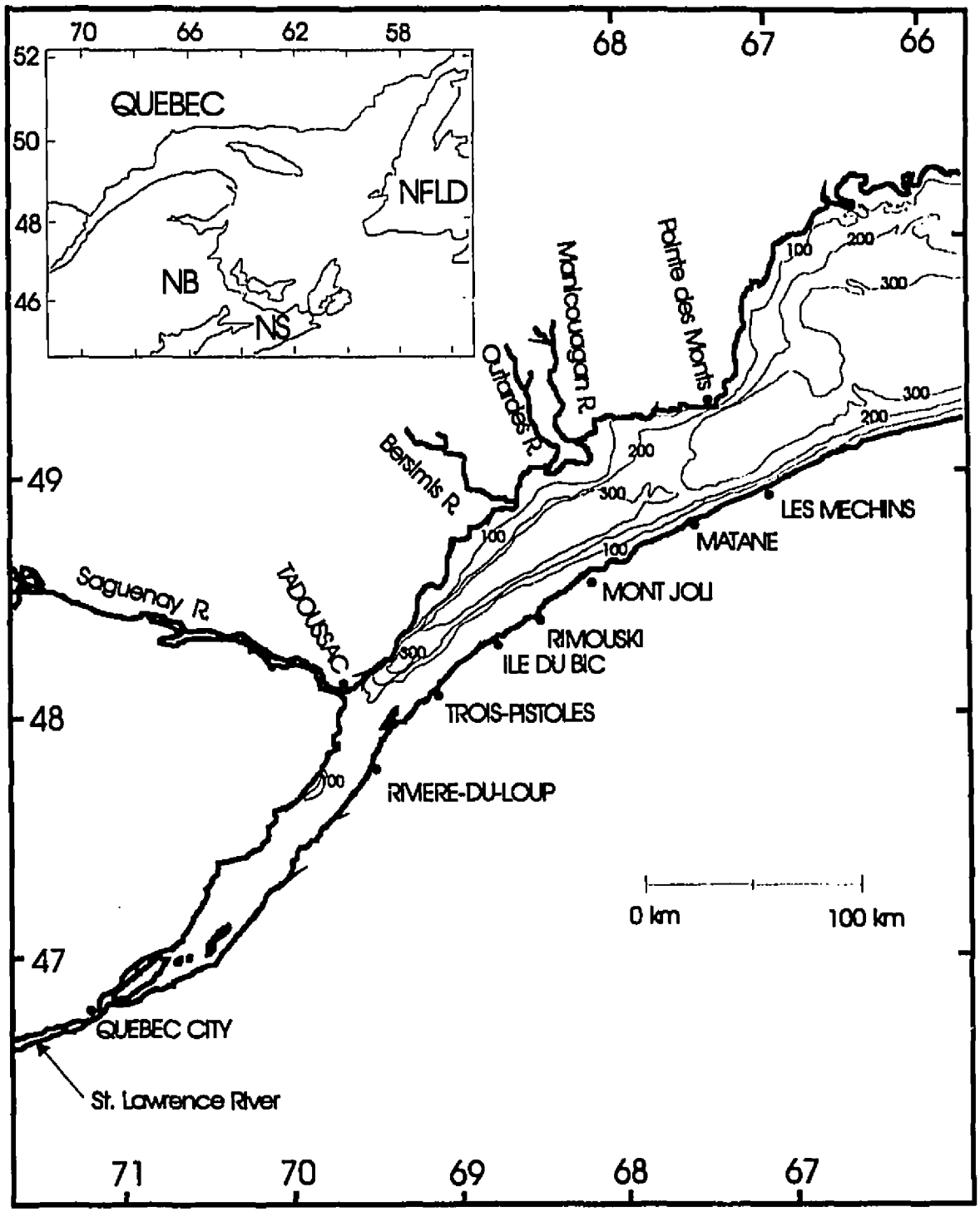

figure 1. Map of the St. Lawrence estuary

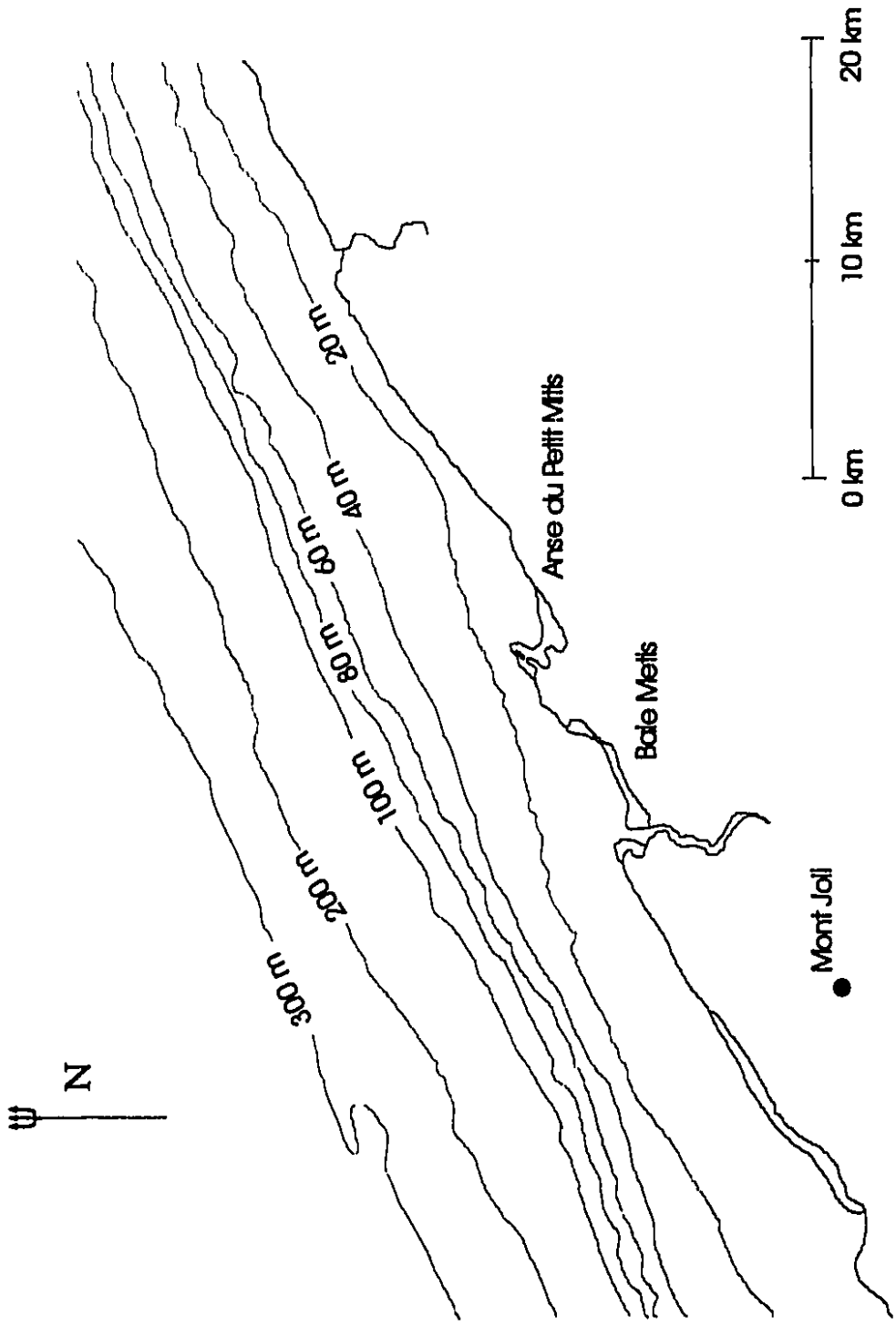

figure 2. Map the of Mont Joli area.

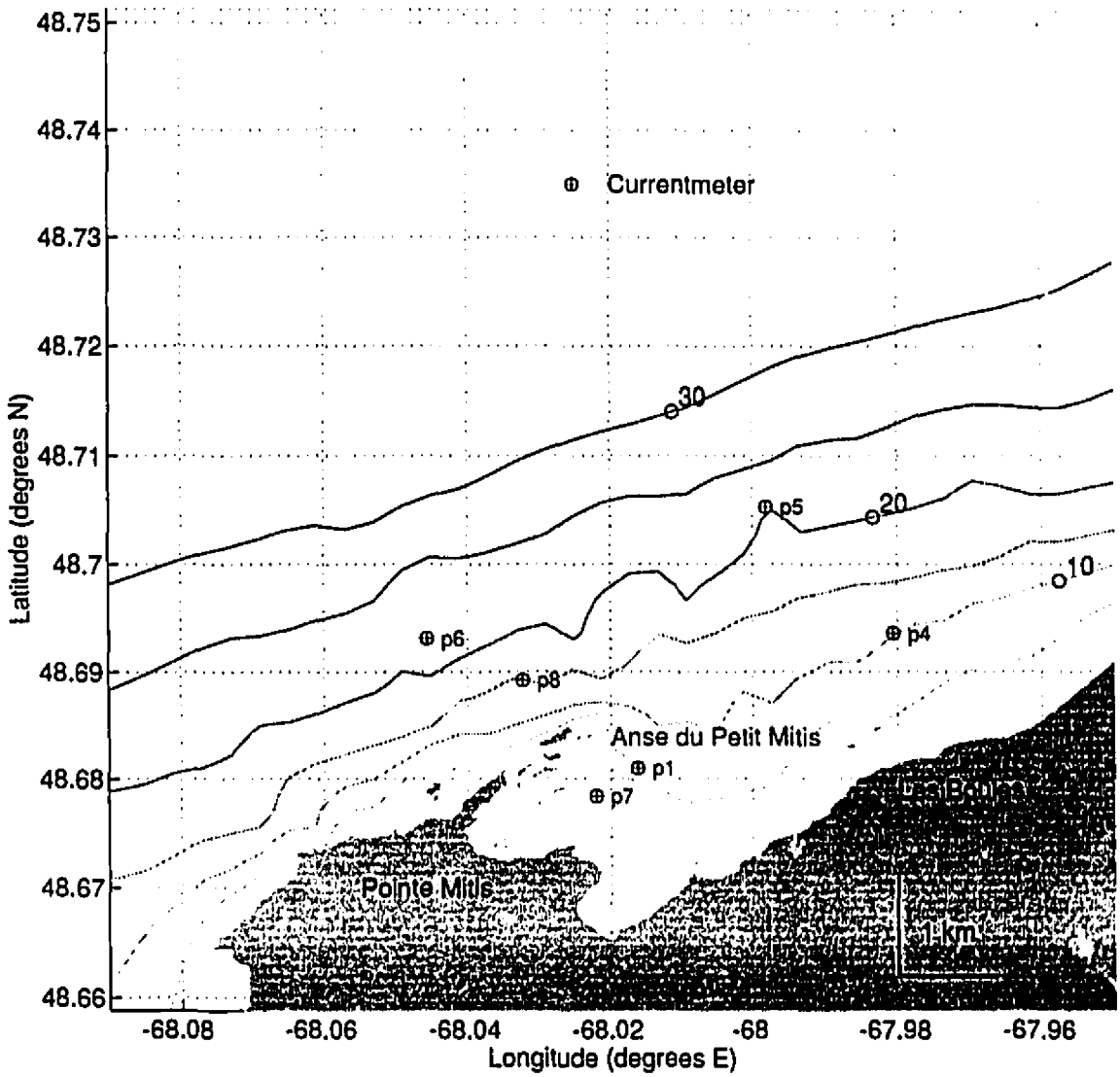

figure 3 Bathymetric map of the study site, L'Anse du Petit Mitis, showing the location of the moored current metres. The contour interval is 5 metres. Contours are shown only to 30 metres depth.

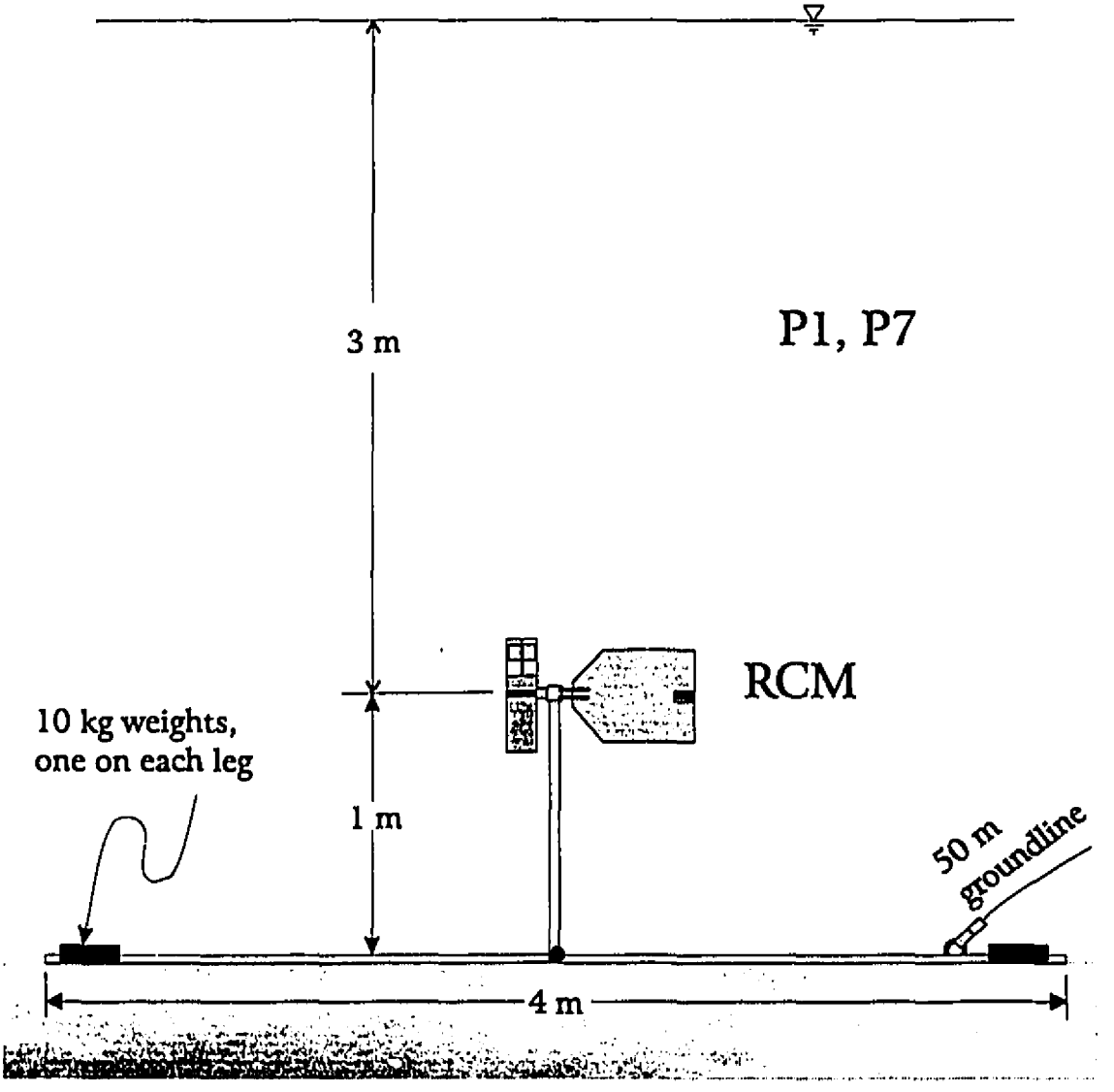

figure 4 Schematic diagram of tripod, shallow water moorings; p1 and p7.

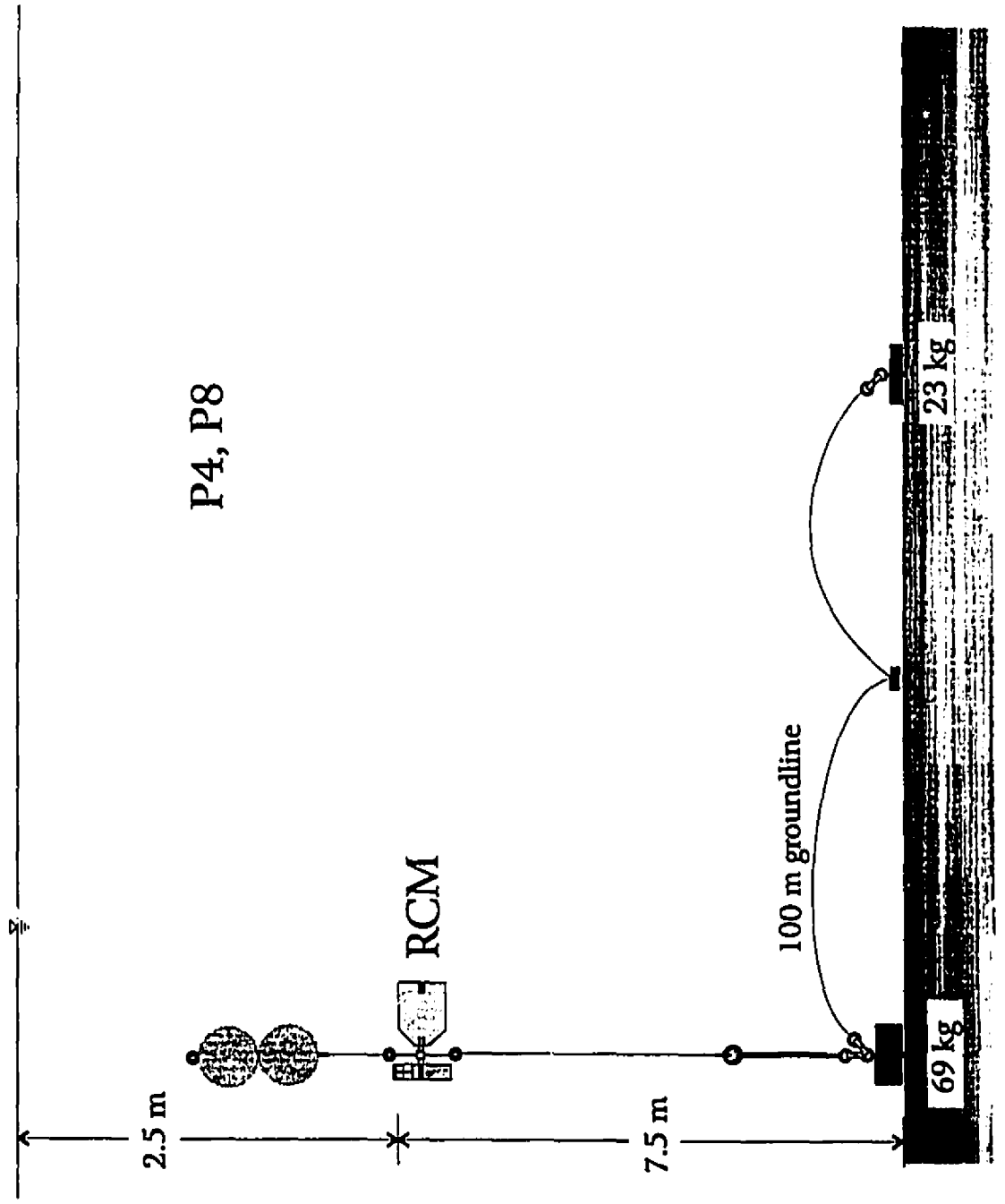

figure 5 Schematic diagram of L-type, medium depth mooring; p4 and p8.

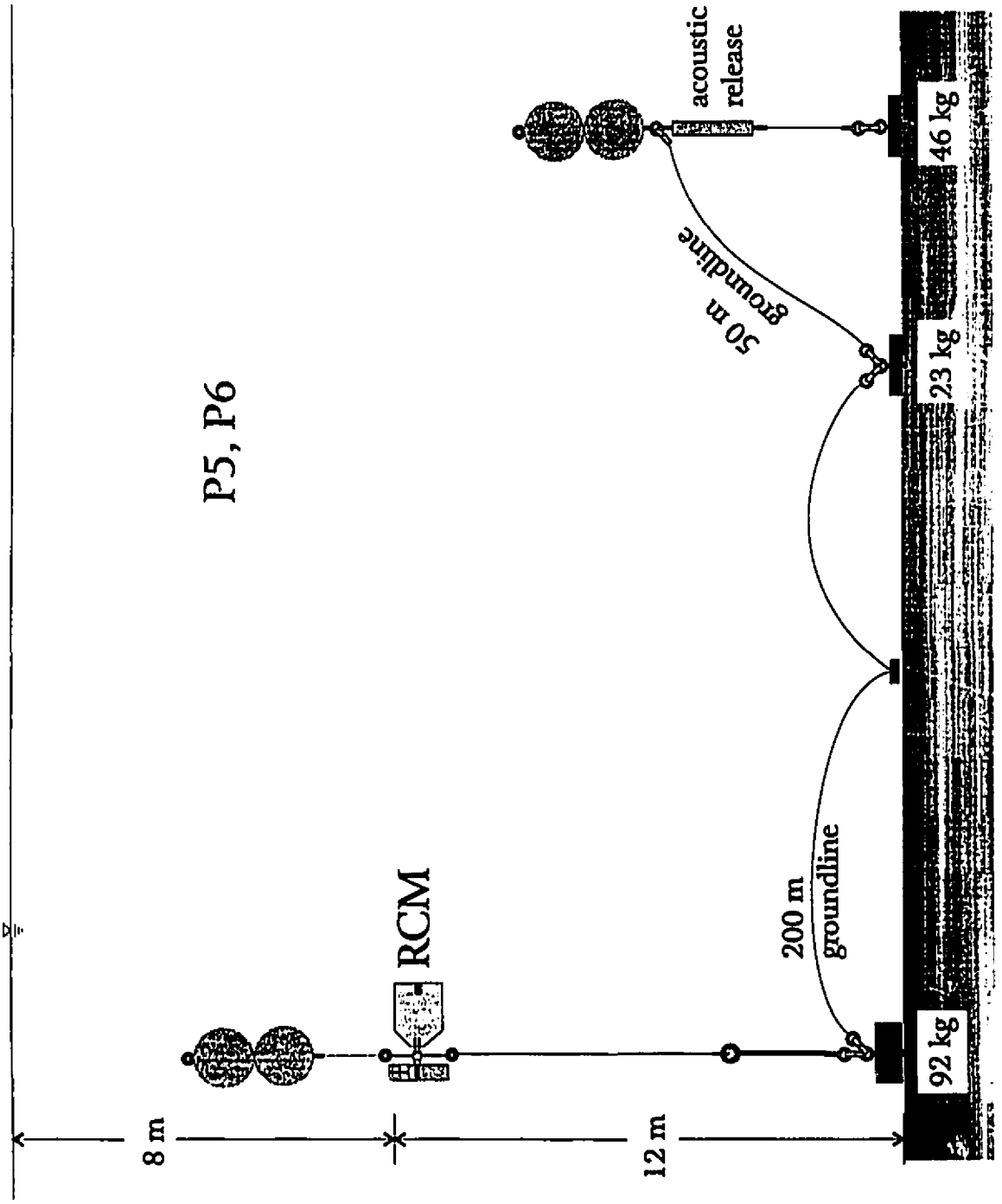

figure 6 Schematic diagram of the U-type, deep water mooring; p5 and p6.

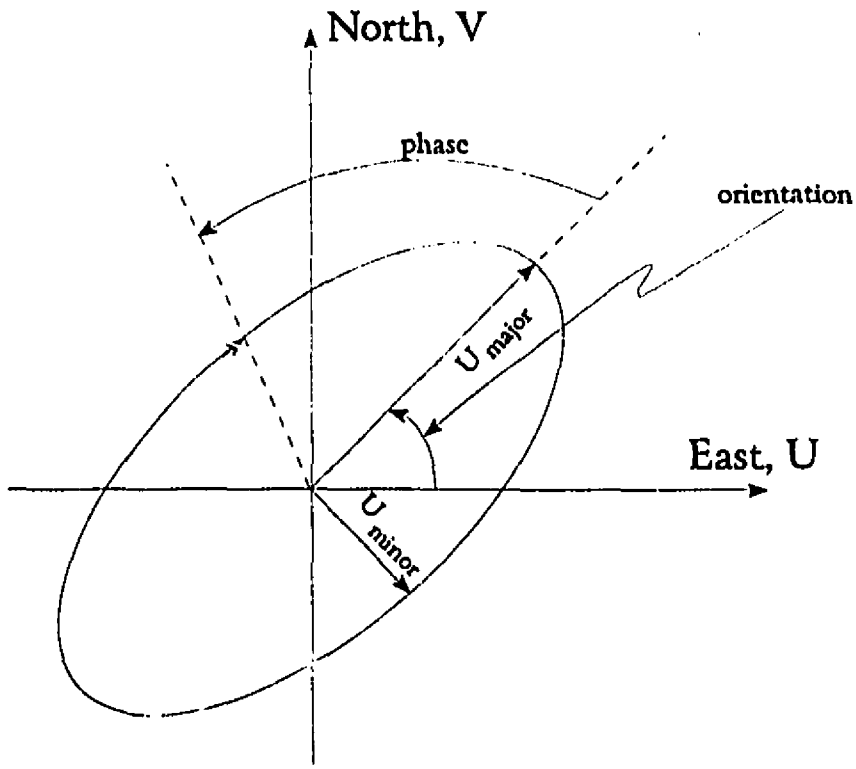

figure 7 Schematic of a tidal ellipse. Tidal velocities for each tidal frequency can be represented as tidal ellipse. The ellipse represents the path traced out by the tip of the velocity vector during a tidal cycle. The orientation angle of the ellipse is the angle measured from east to the semi-major axis of the ellipse. The phase lag of the maximum tidal current is indicated as the angle measured from the semi-major axis of the ellipse to the tip of the arrowhead, where 360° represents one complete cycle of the tide in question and the arrowhead direction indicates the direction of rotation of the velocity vector.

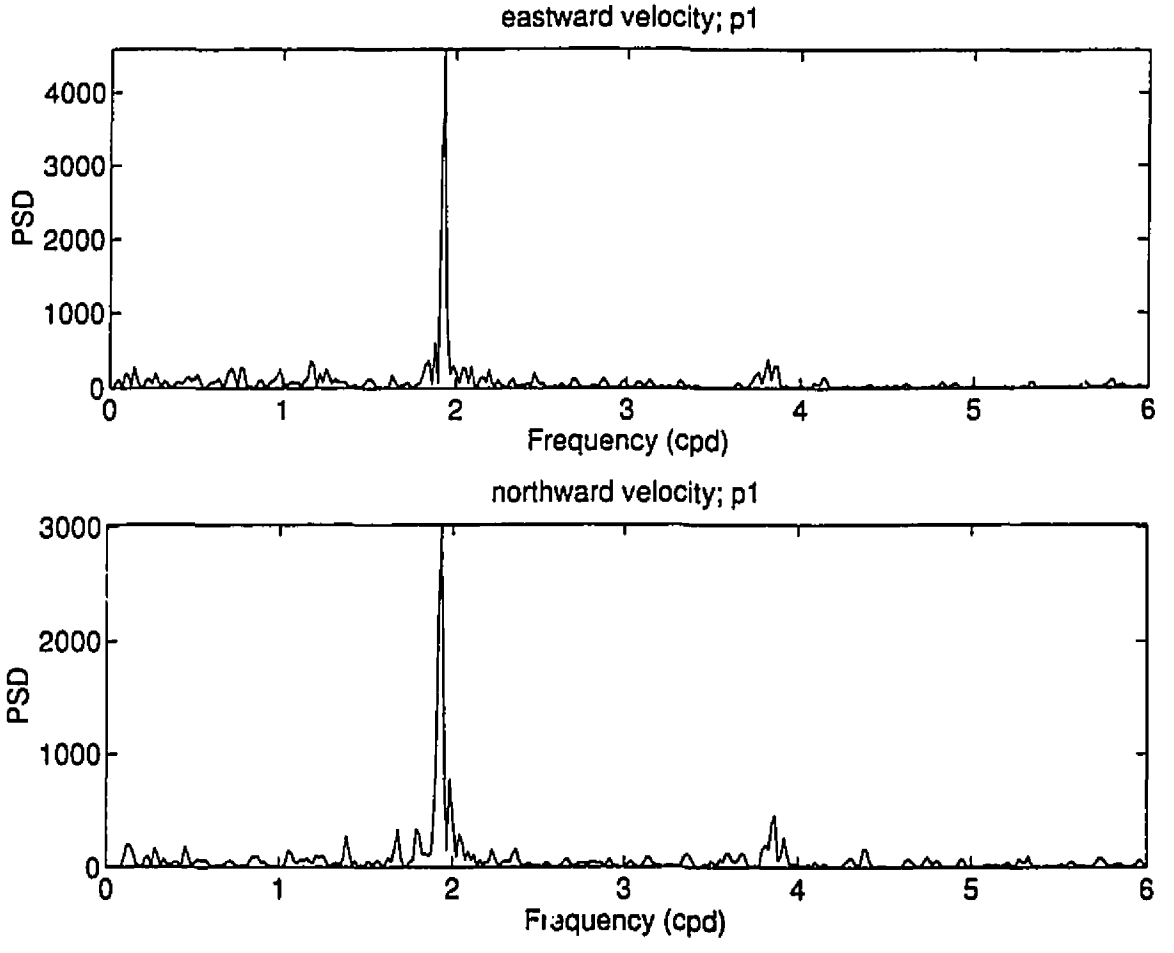

figure 8a Power spectra of the east, u, and north, v, components of velocity. Station p1.

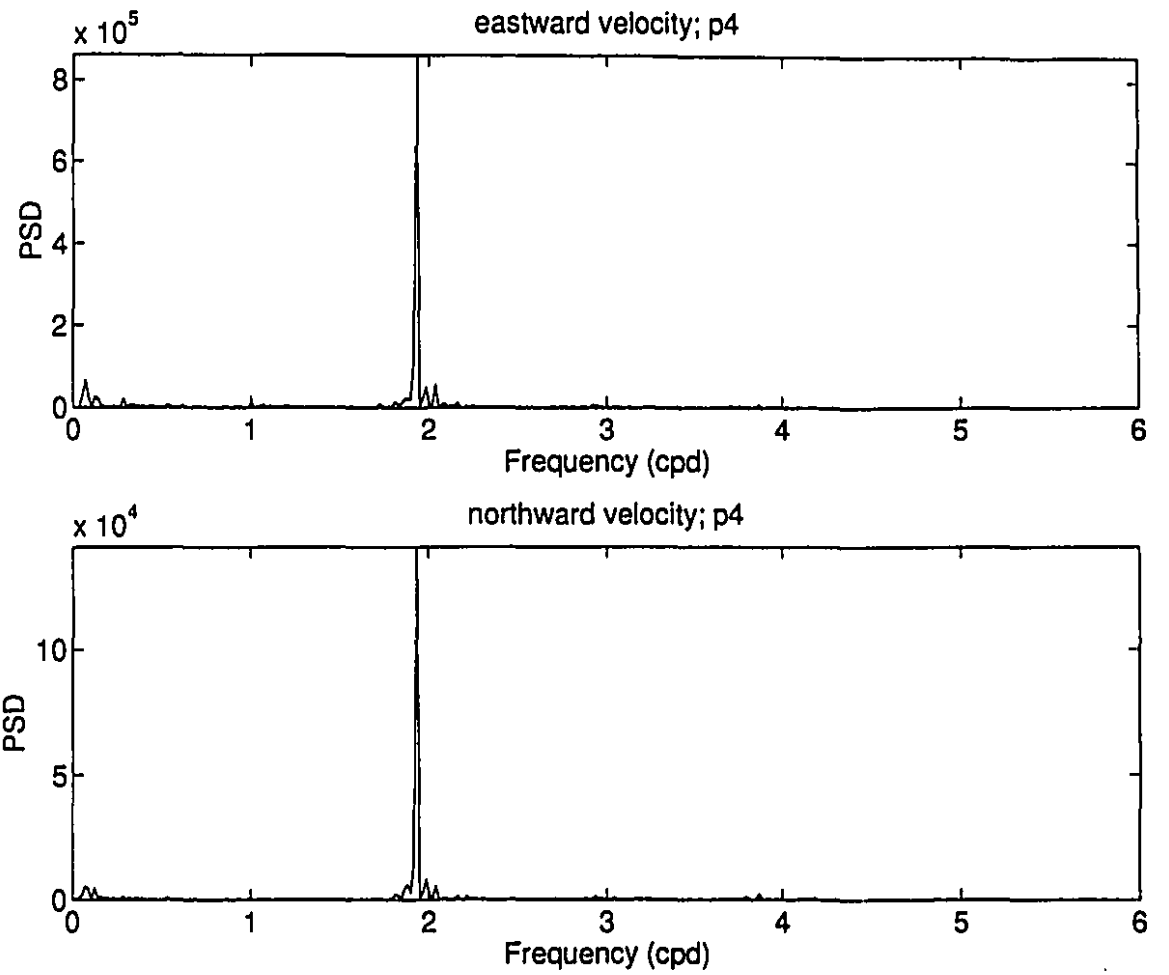

figure 8b Power spectra of the east, u, and north, v, components of velocity. Station p4.

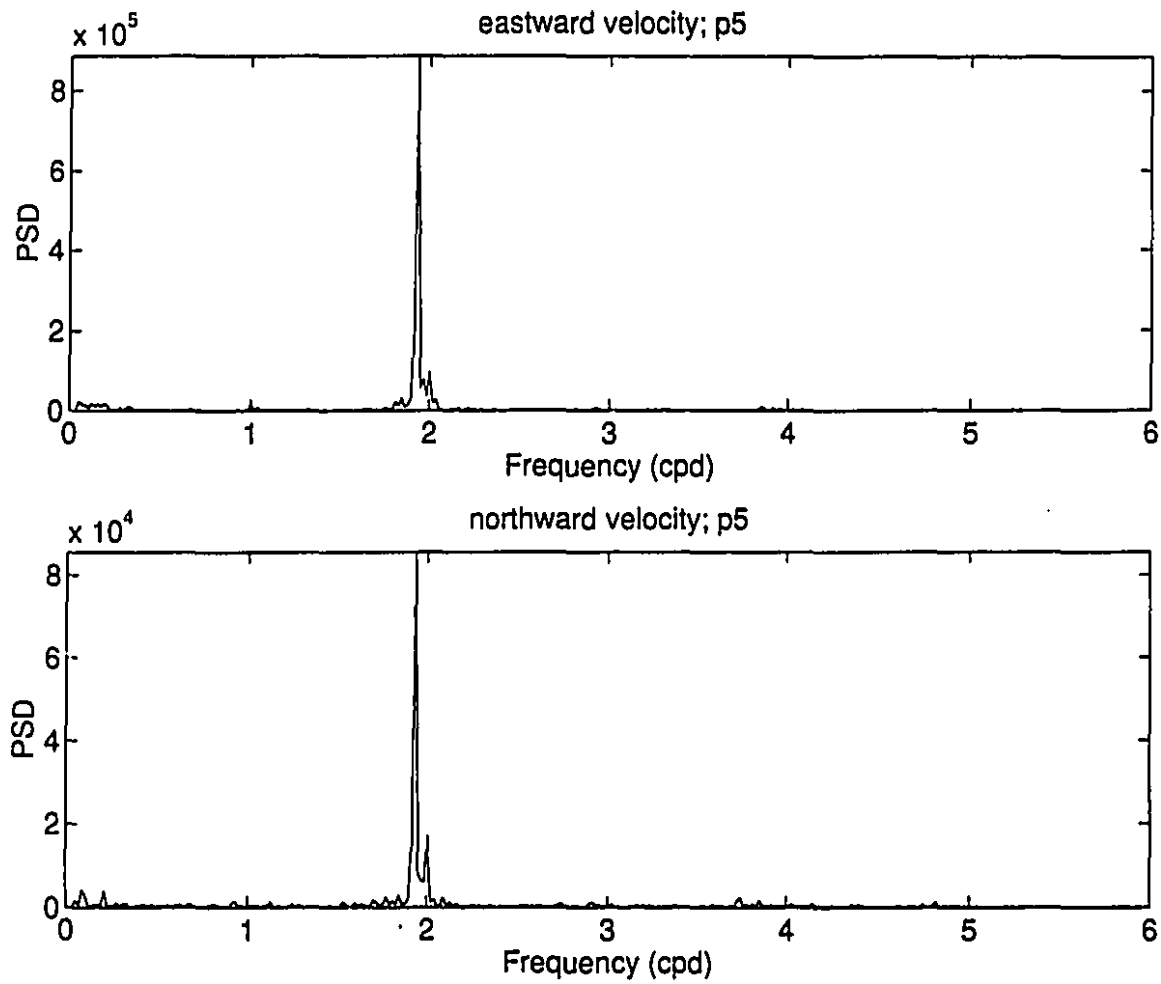

figure 8c Power spectra of the east, u, and north, v, components of velocity. Station p5.

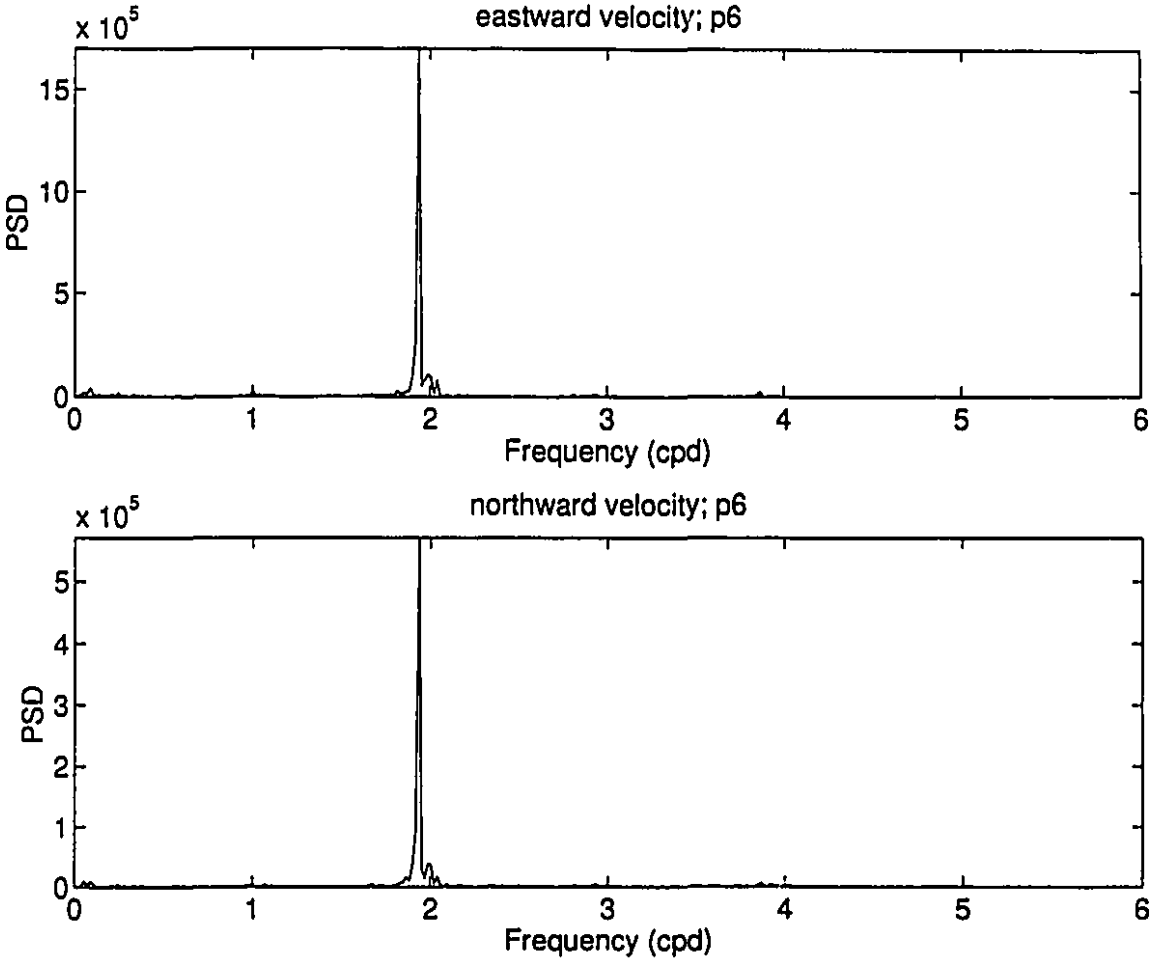

figure 8d Power spectra of the east, u, and north, v, components of velocity. Station p6.

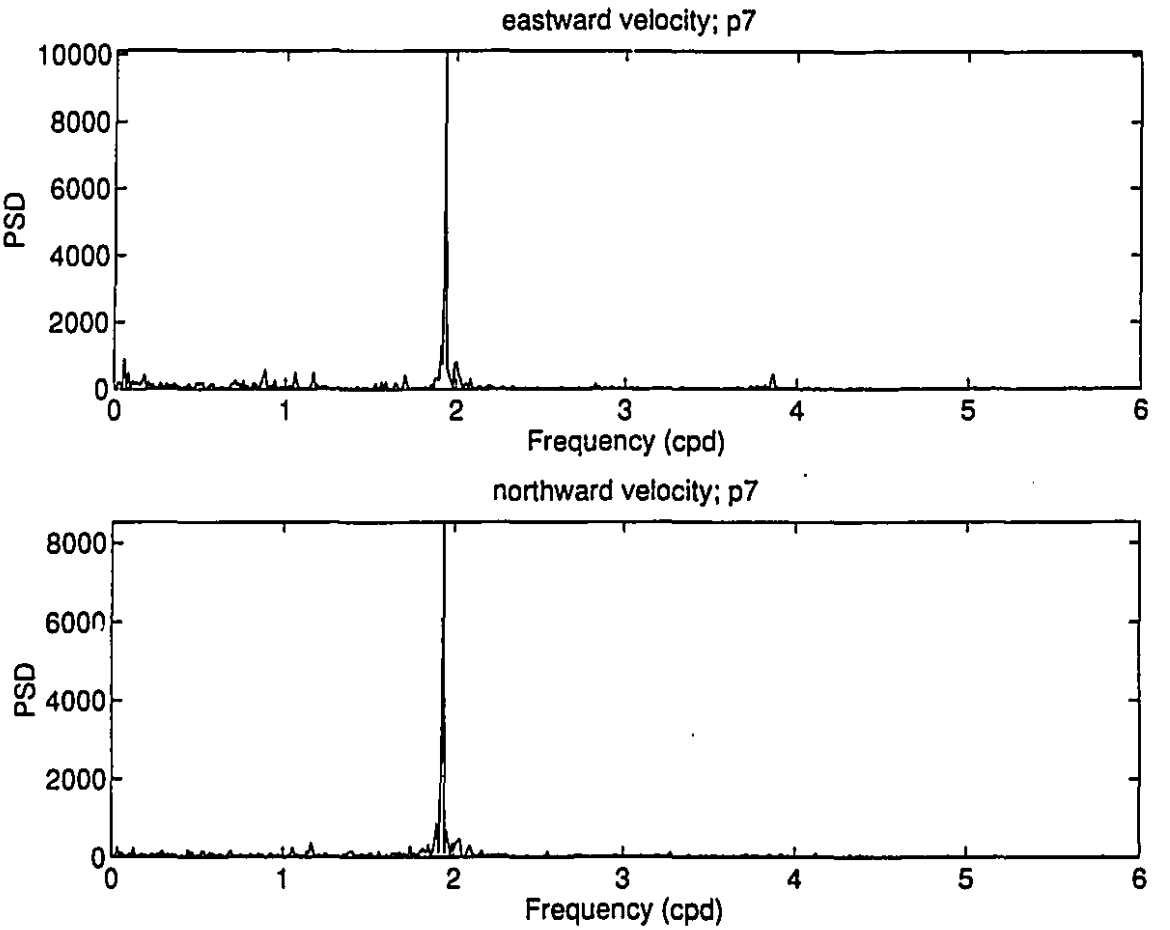

figure 8e Power spectra of the east, u, and north, v, components of velocity. Station p7.

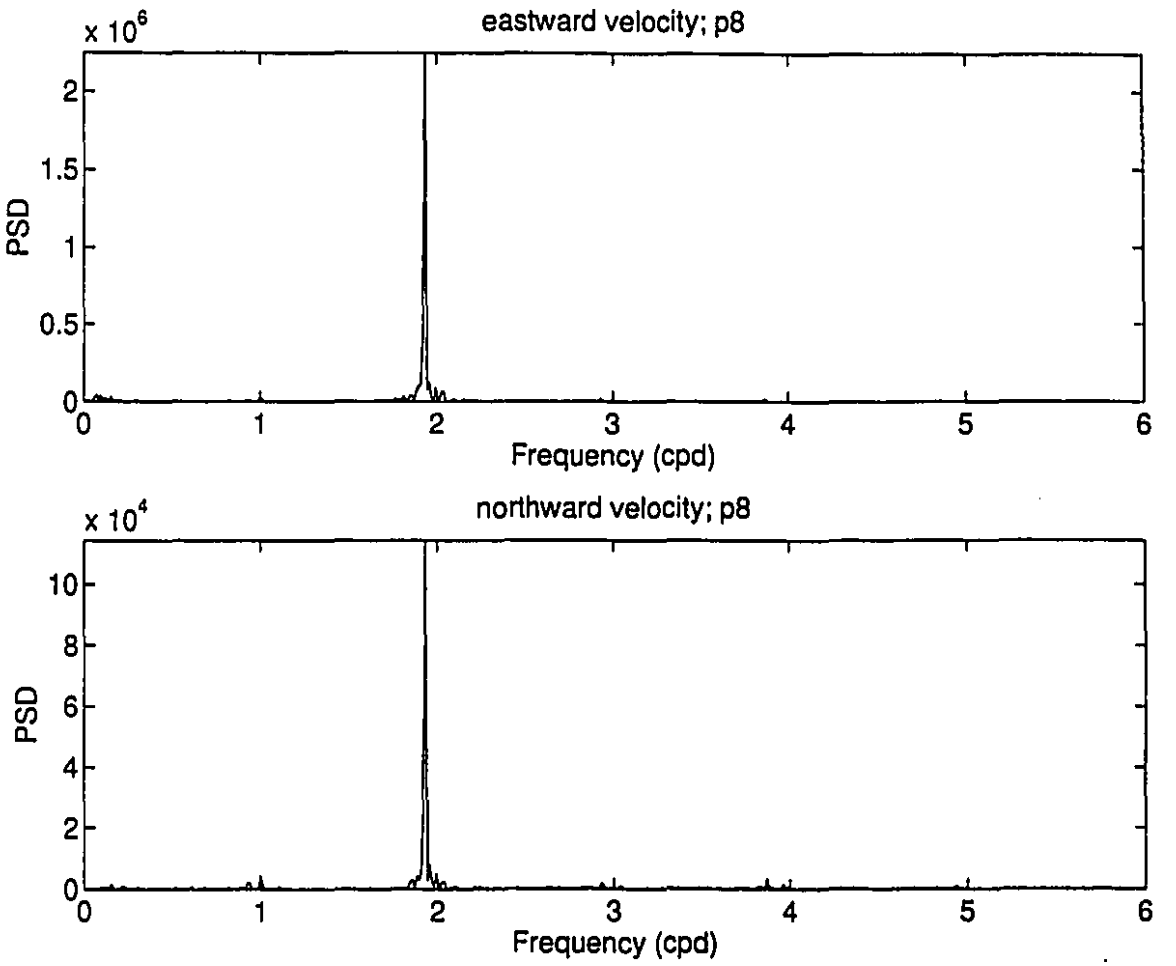

figure 8f Power spectra of the east, u, and north, v, components of velocity. Station p8.

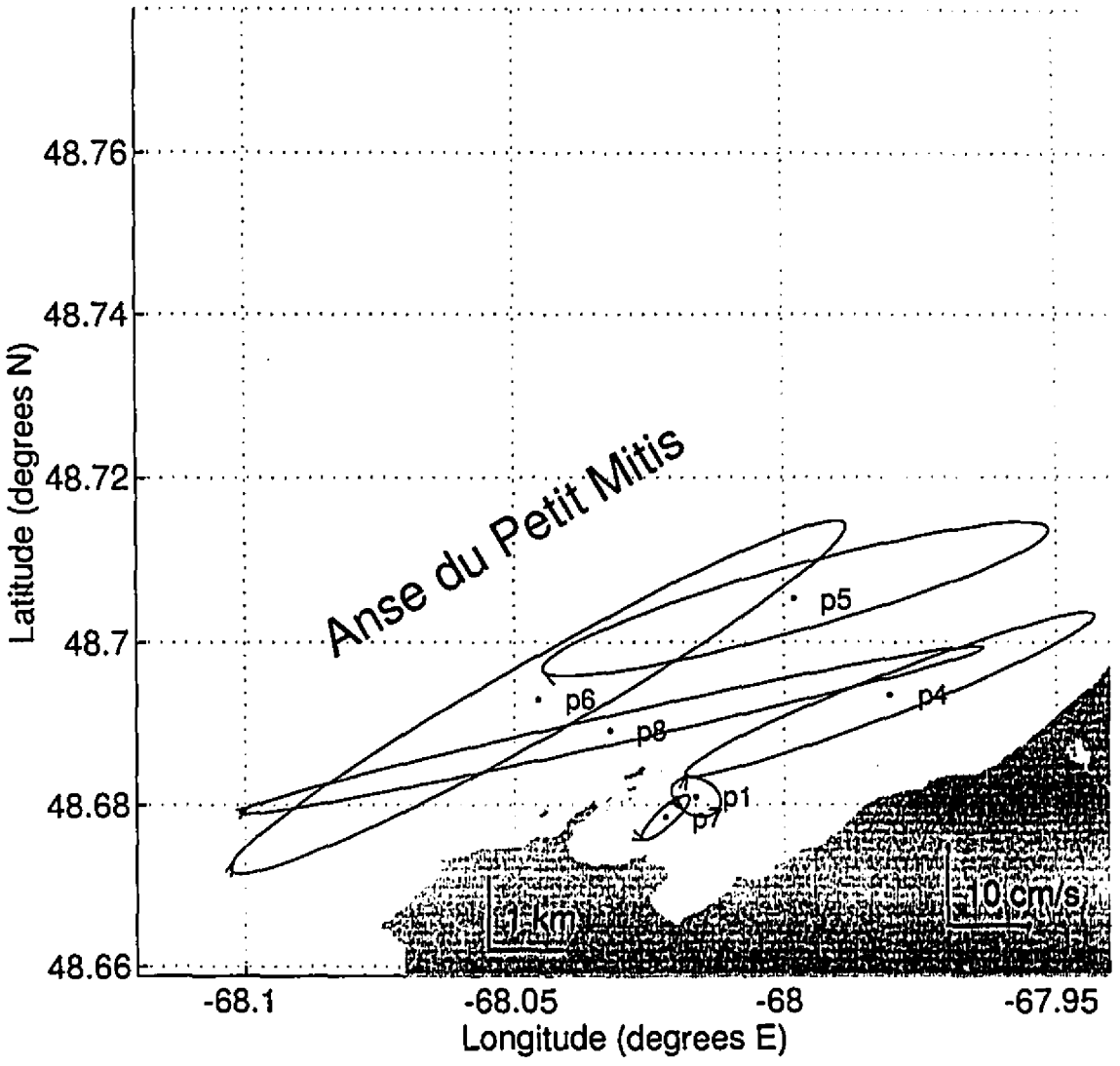

figure 9 M_2 tidal ellipses at L'Anse du Petit Mitis. The convention used is as described in figure 7.

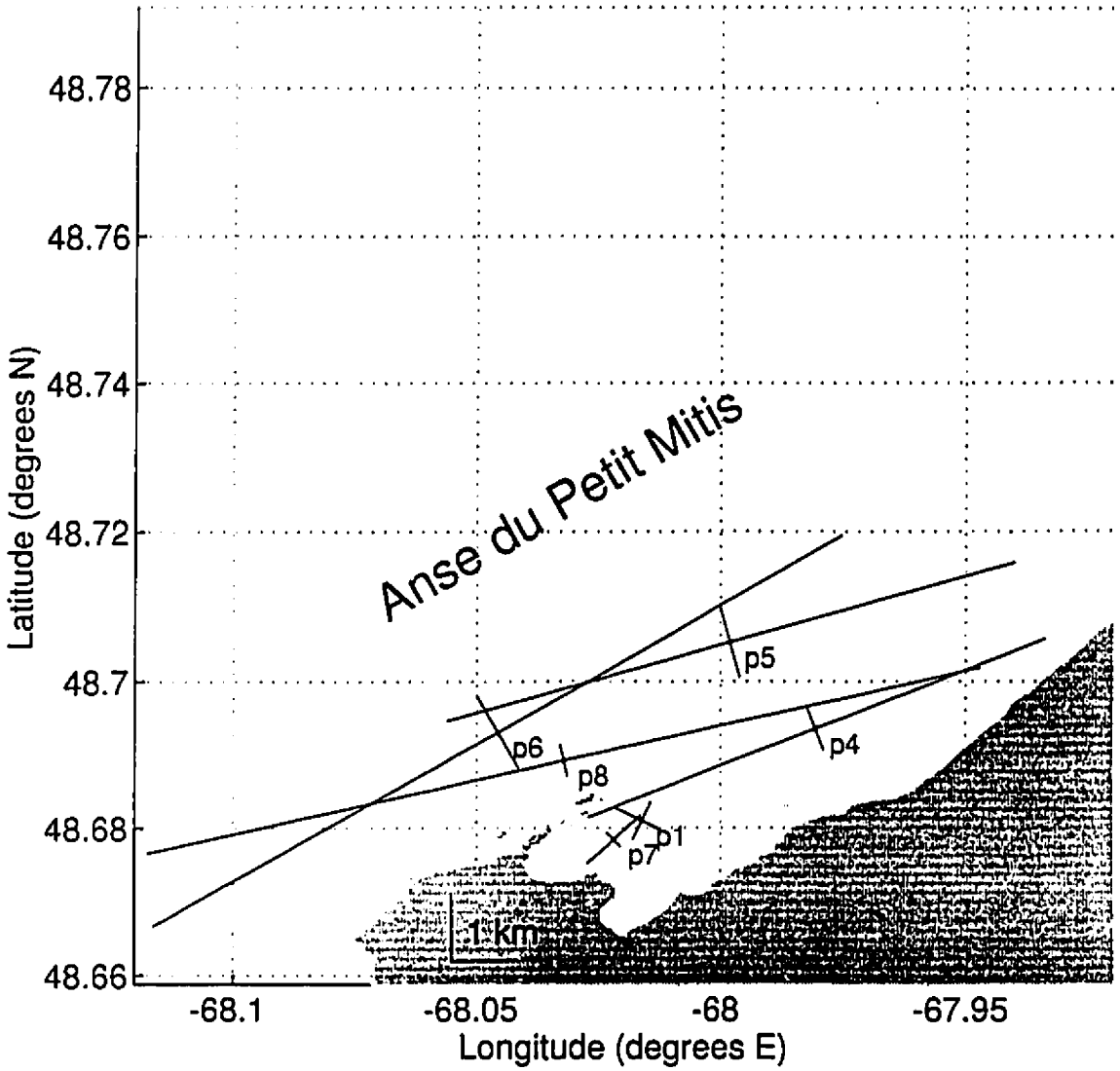

figure 10 M_2 tidal excursion lengths at L'Anse du Petit Mitis

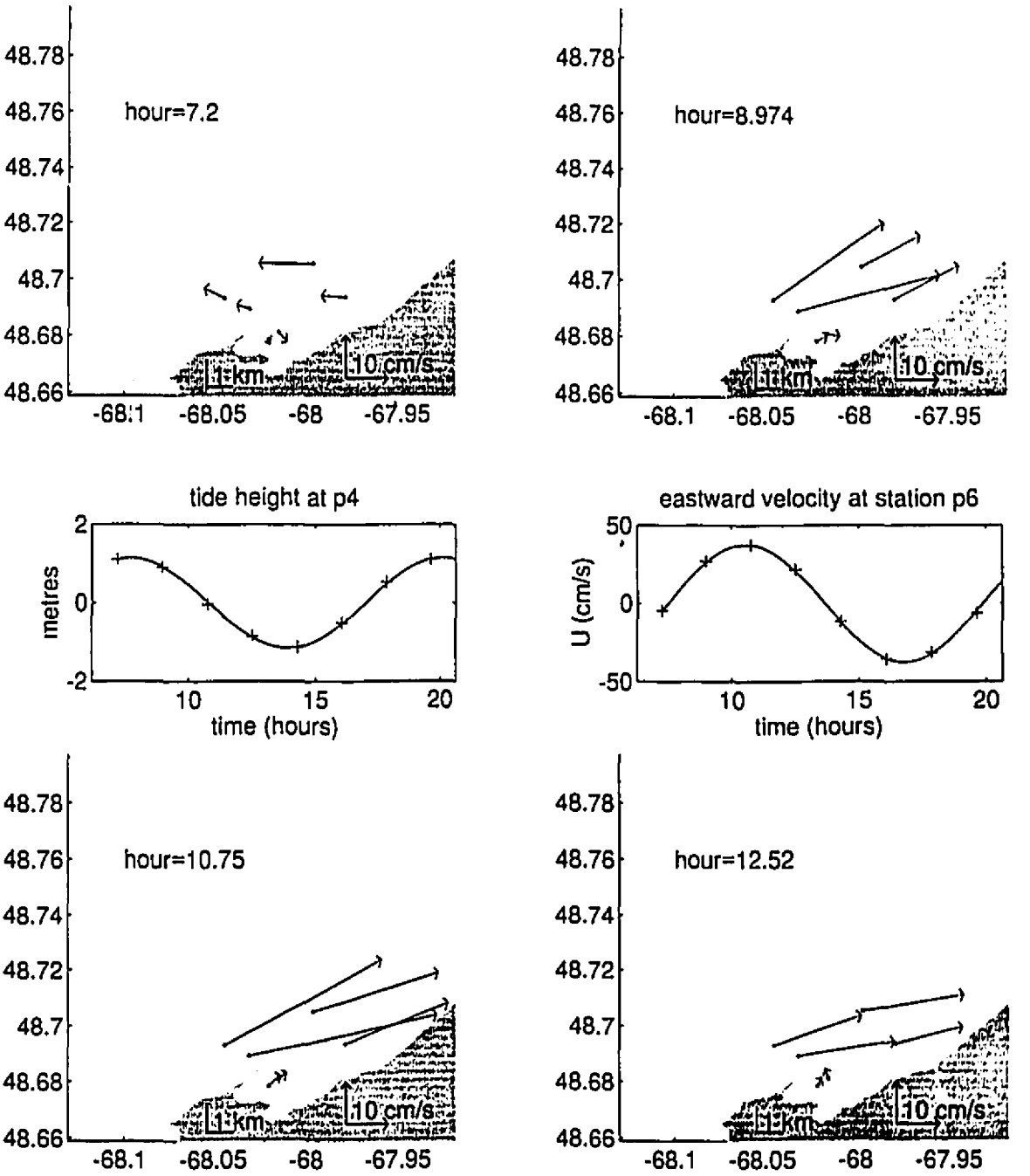

figure 11 Snapshots of the M_2 tidal currents at eight equally spaced times during one M_2 tidal cycle. The centre panels show tide height and eastward tidal velocity at stations p4 and p6 respectively, with plus signs indicating the snapshot times.

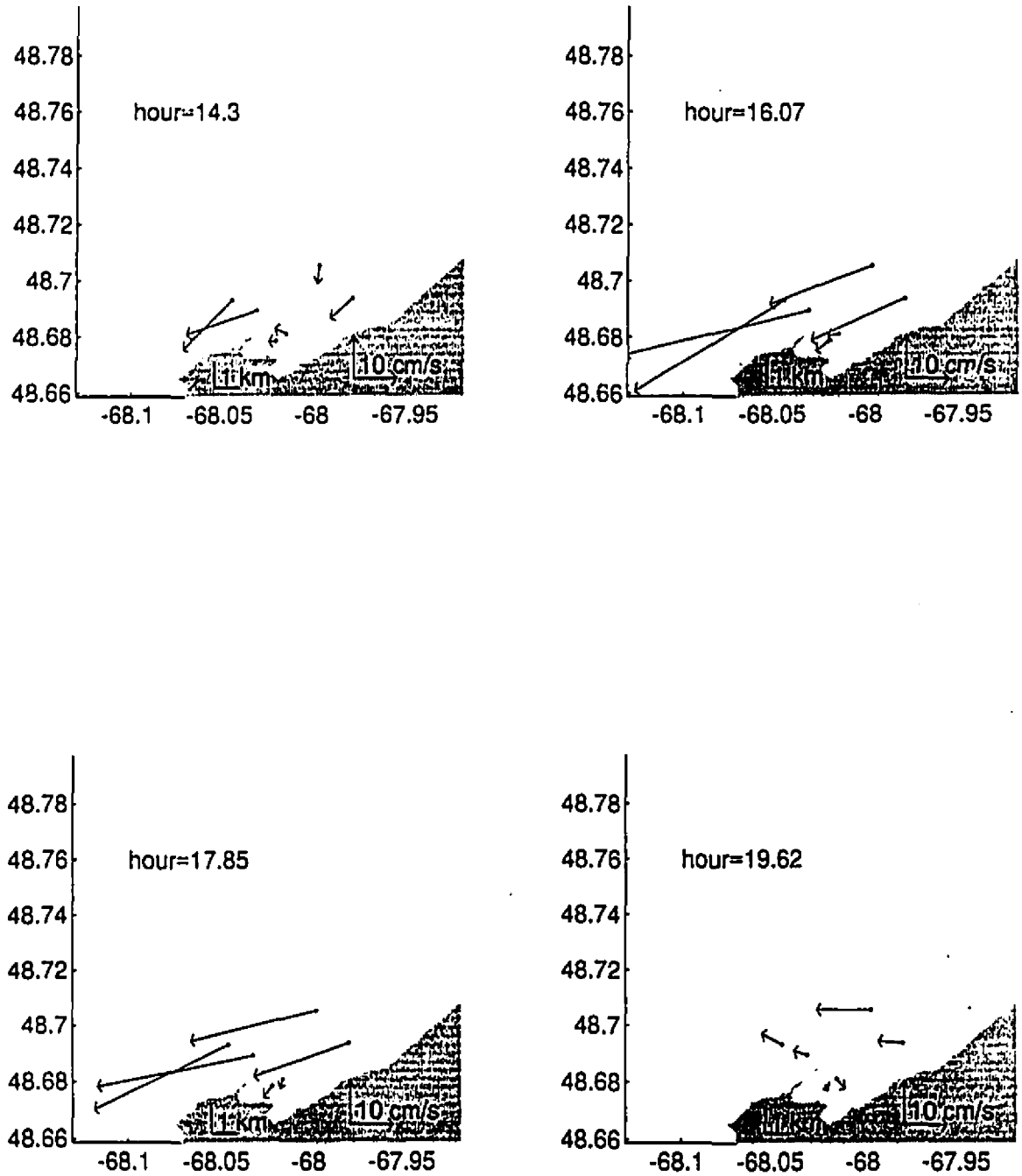

figure 11 continued Snapshots of the M_2 current at eight equally spaced times during one M_2 tidal cycle.

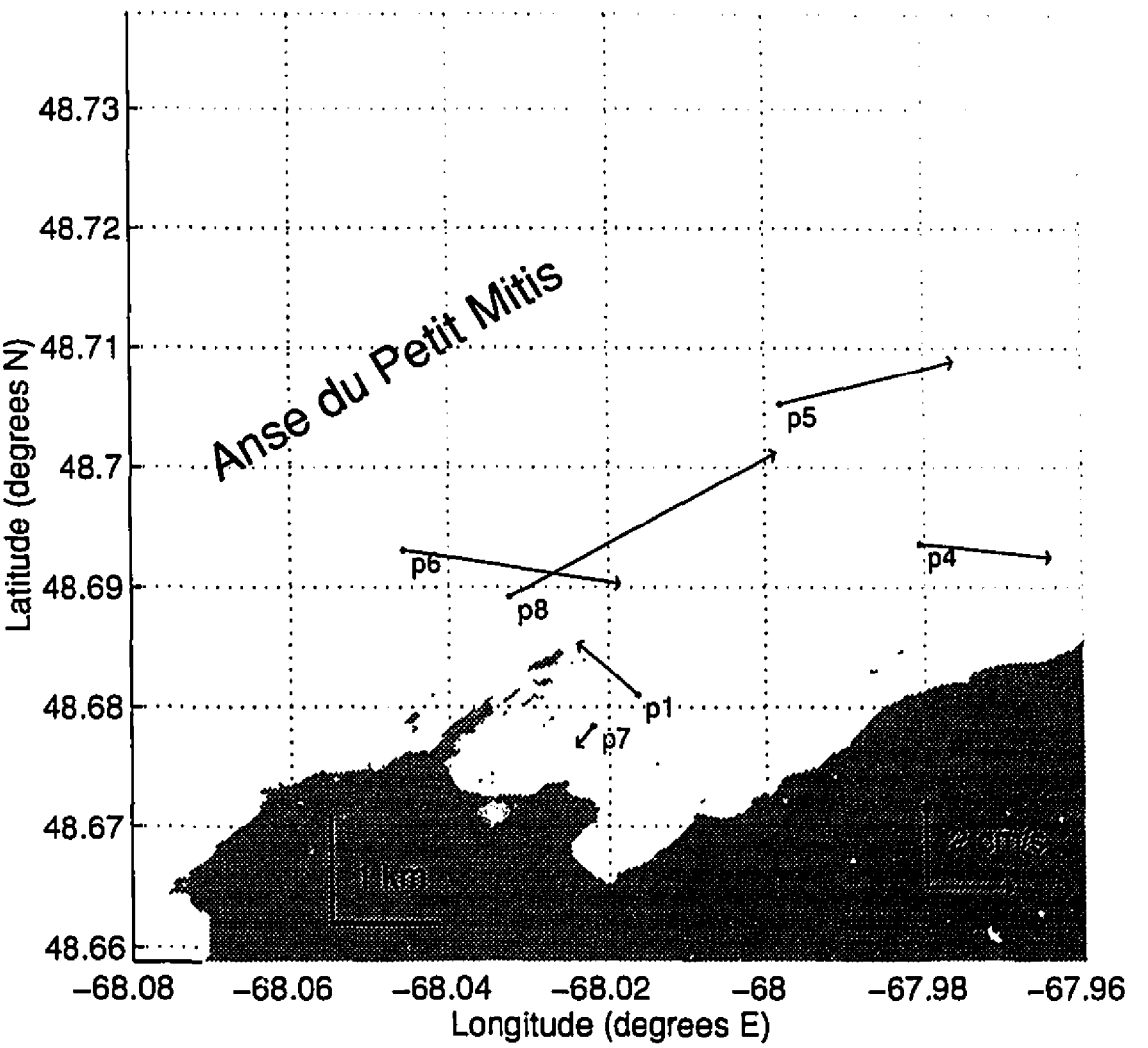

figure 12 Eulerian vector average velocities at L'Anse du Petit Mitis.

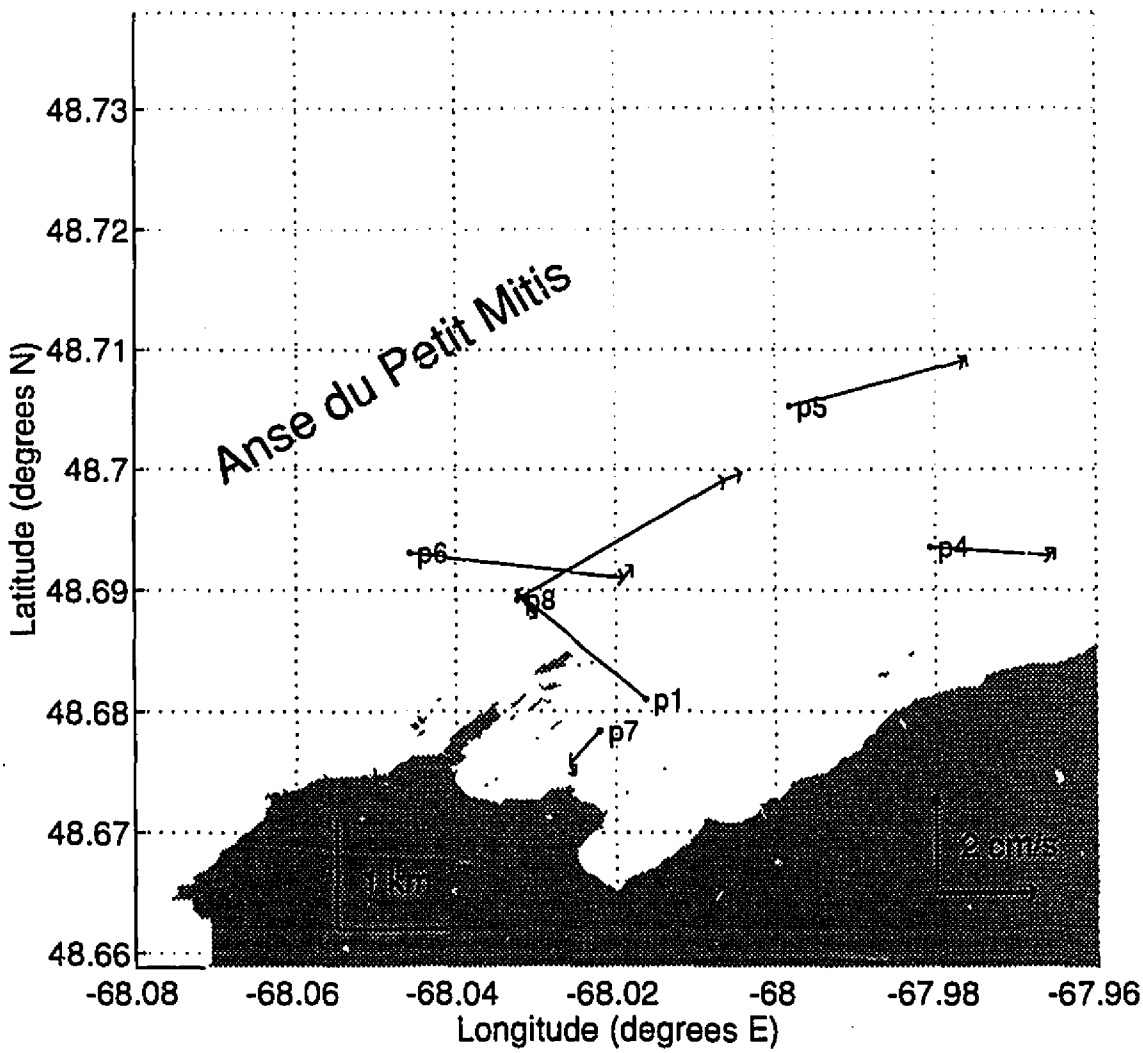

figure 13 Eulerian vector average and Stokes drift correction velocities. The shortest arrow is the Stokes correction. The arrow pointing to its tail is the depth, and time averaged eulerian velocity.

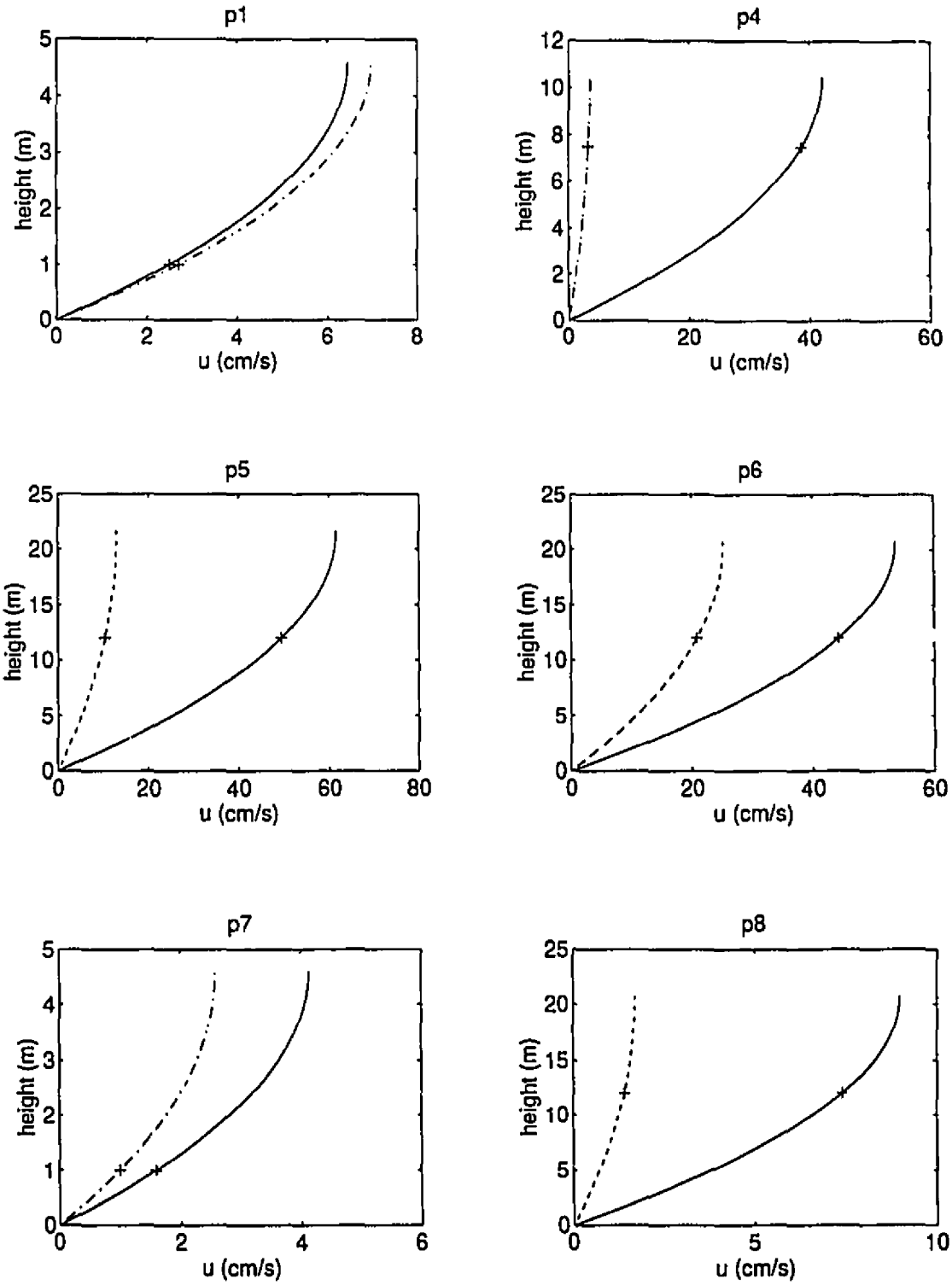

figure 14 Quadratic vertical velocity profiles at all six stations, at hour 10 of Julian elapsed day (JED) 194. The eastward velocity component, u, is given as a solid line, and the northward velocity component, v, is given as a dotted line. The RCM height is given as a plus sign.

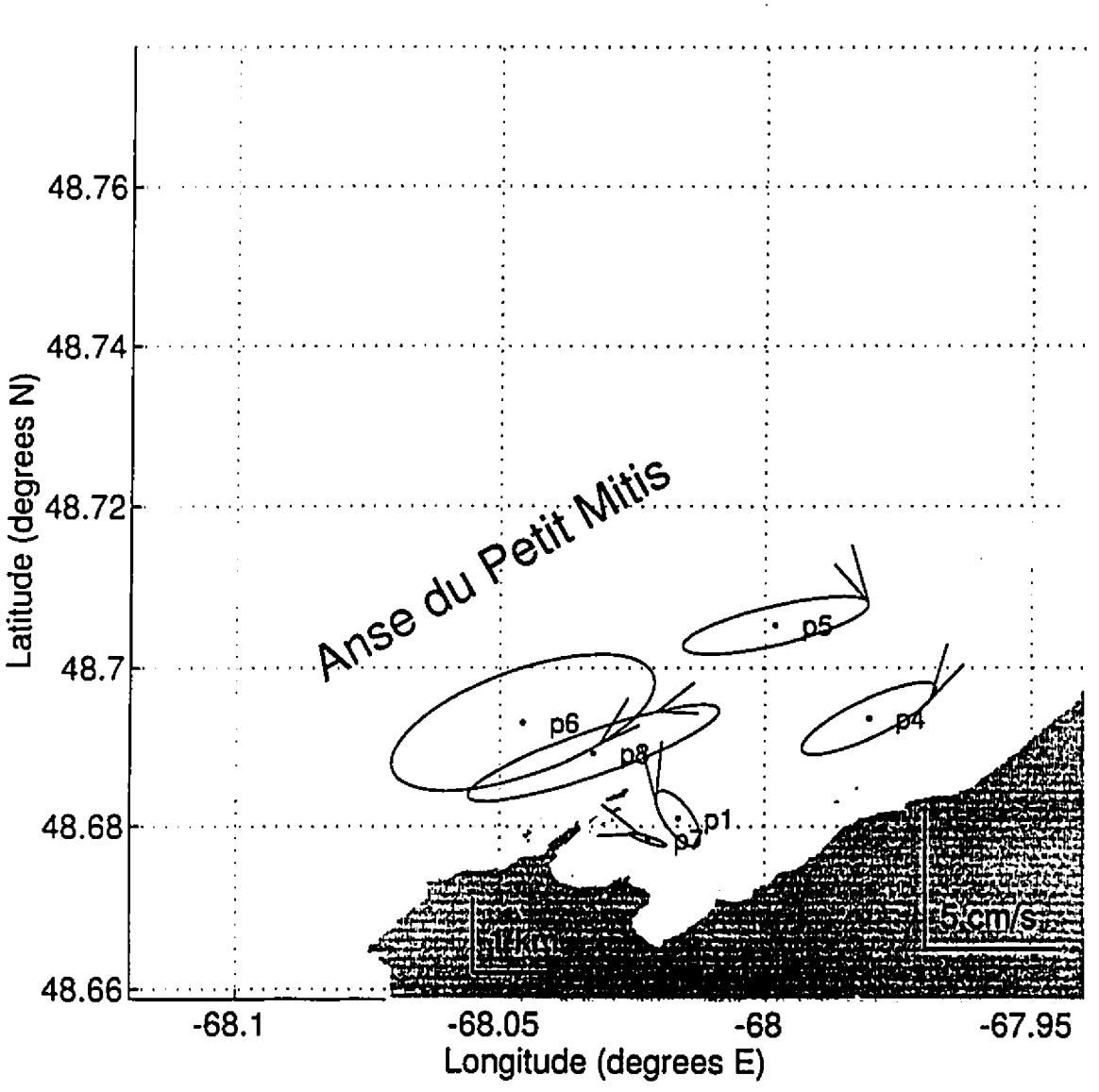

figure 15 M_4 tidal ellipses at L'Anse du Petit Mitis

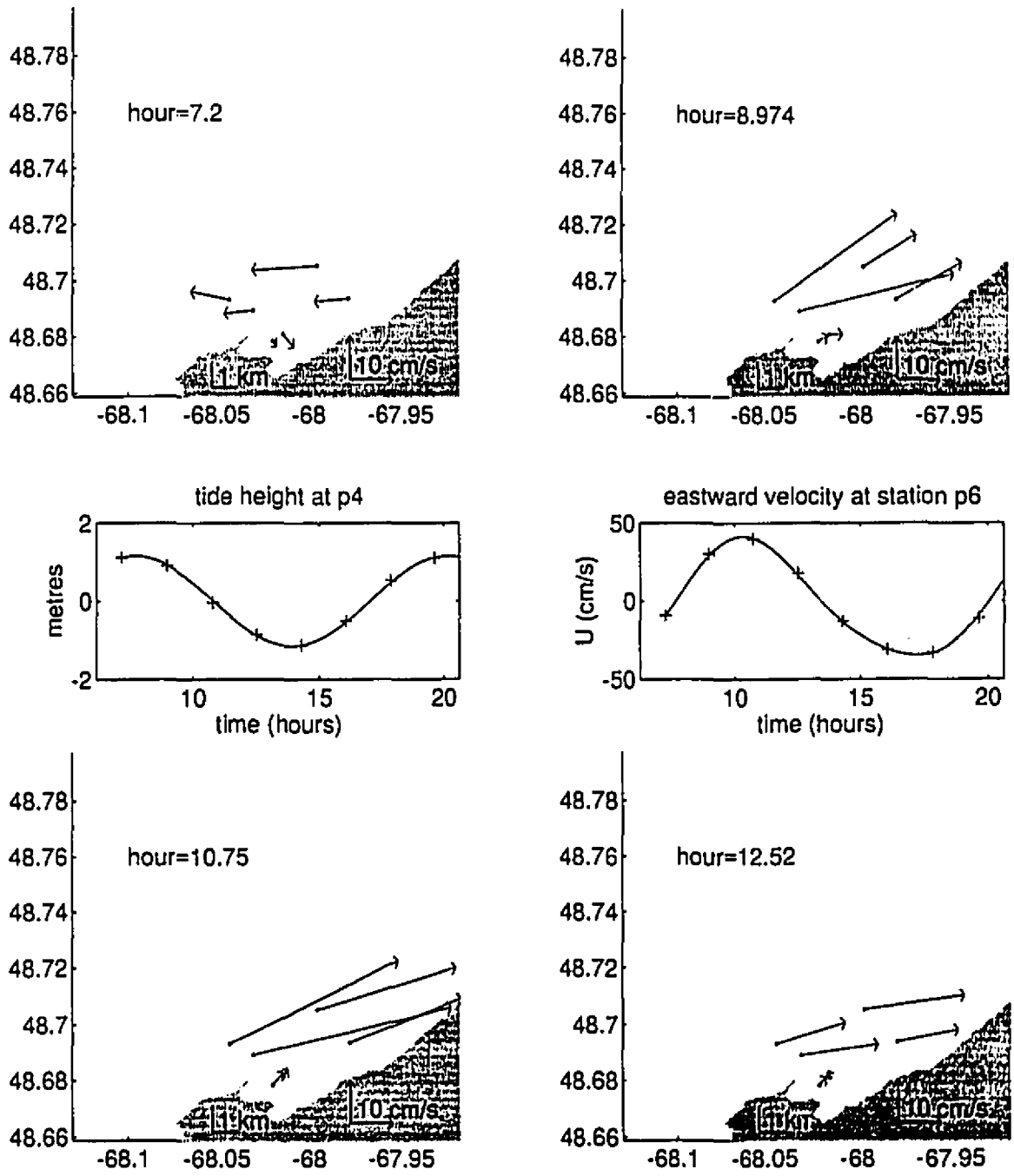

figure 16 Snapshots of the M_2 + M_4 current at eight equally spaced times during one M_2 tidal cycle. The centre panels show tide height and eastward tidal velocity at stations p4 and p6 respectively, with plus signs indicating the snapshot times.

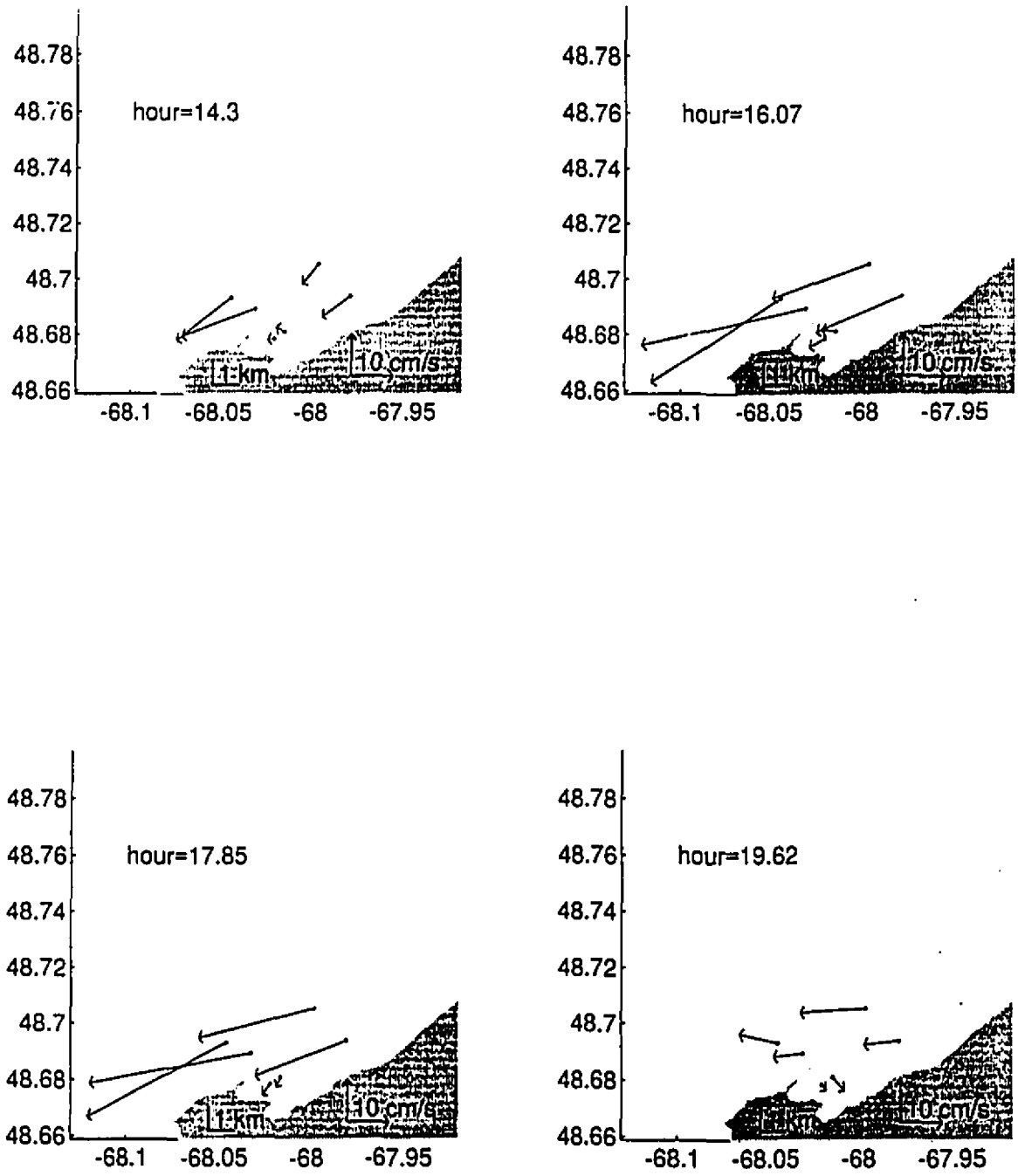

figure 16 continued Snapshots of the M_2 + M_4 current at eight equally spaced times during one M_2 tidal cycle.

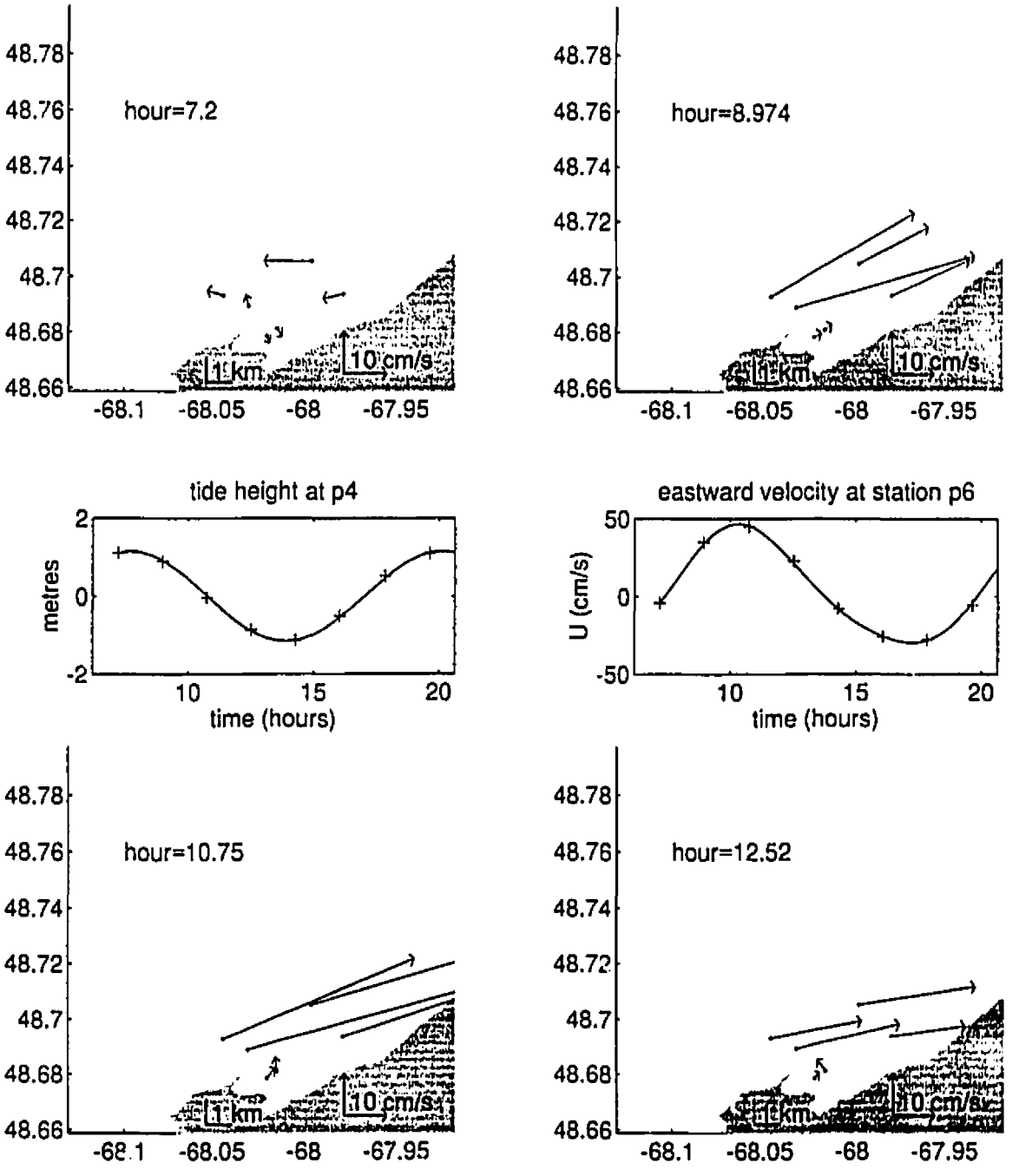

figure 17 Snapshots of the M_2 + M_4 + Eulerian mean current at eight equally spaced during one M_2 tidal cycle. The centre panels show tide height and eastward tidal velocity at stations p4 and p6 respectively, with plus signs indicating the snapshot times.

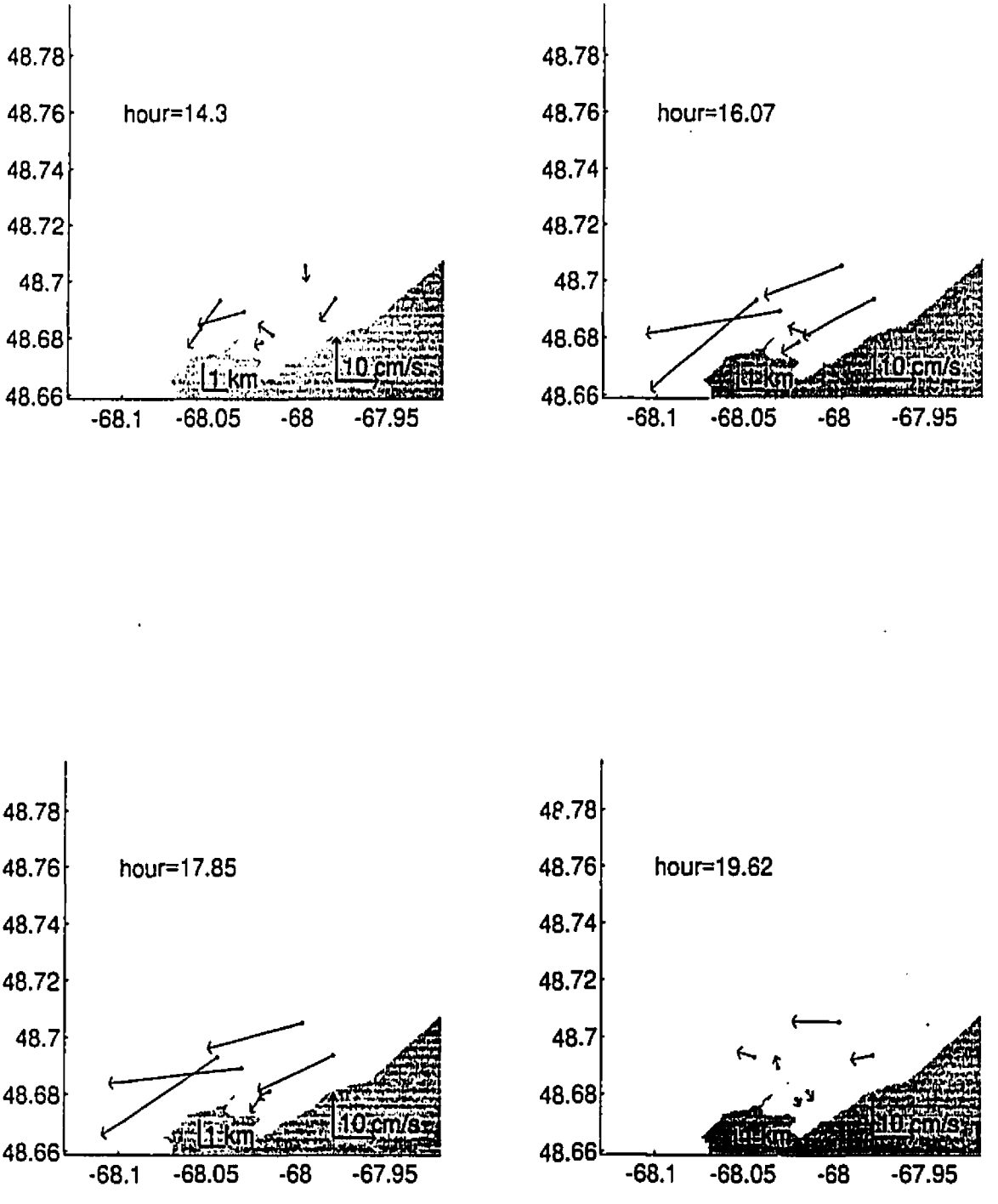

figure 17 continued

Snapshots of the M_2 + M_4 + Eulerian residual current at eight equally spaced times during one M_2 tidal cycle.

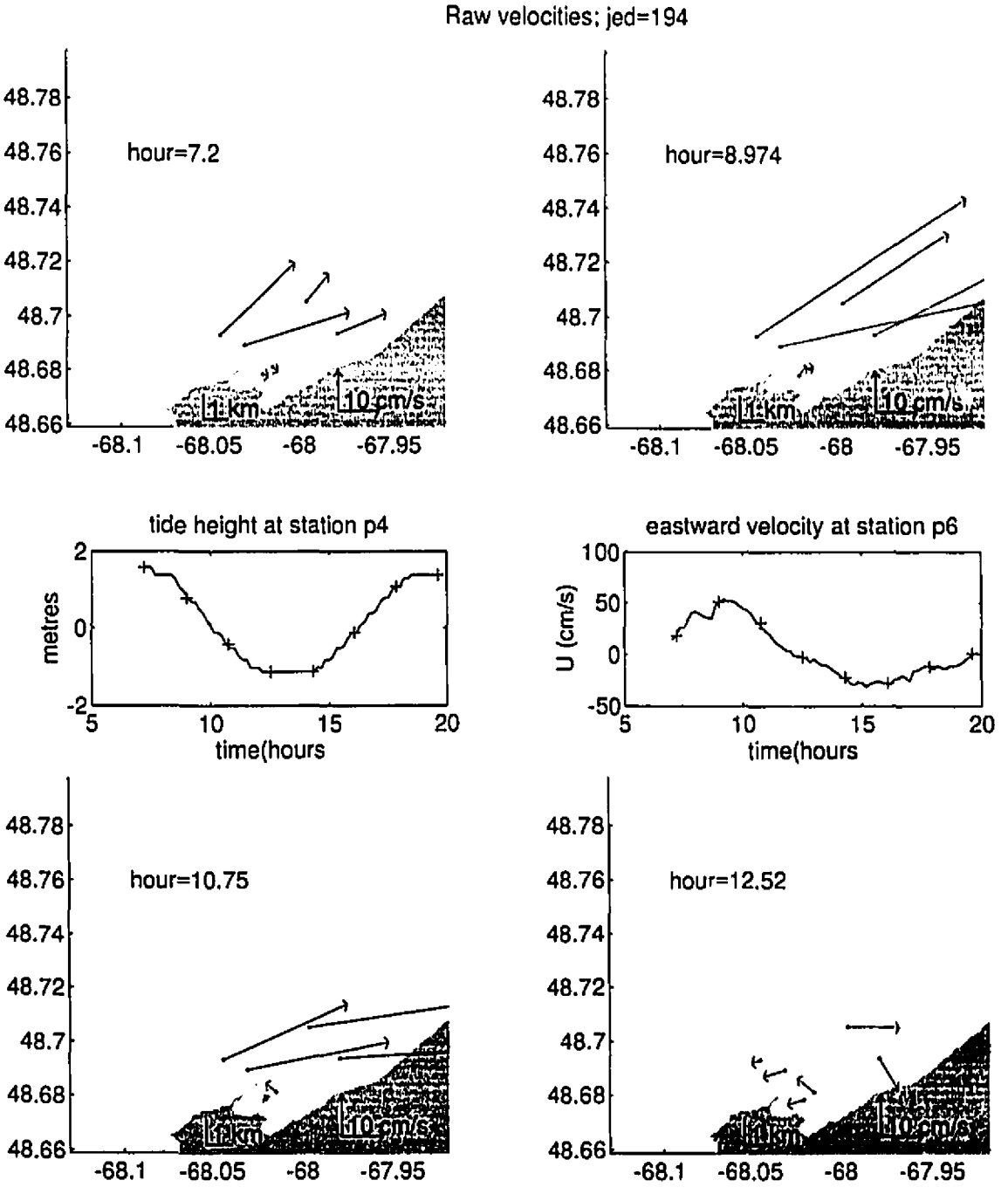

figure 18 Snapshots of the raw velocity data at eight equally spaced intervals during one M_2 tidal cycle. The panels shown are during Julian elapsed day (JED) 194. The centre panels show tide height and eastward tidal velocity at stations p4 and p6 respectively, with plus signs indicating the snapshot times.

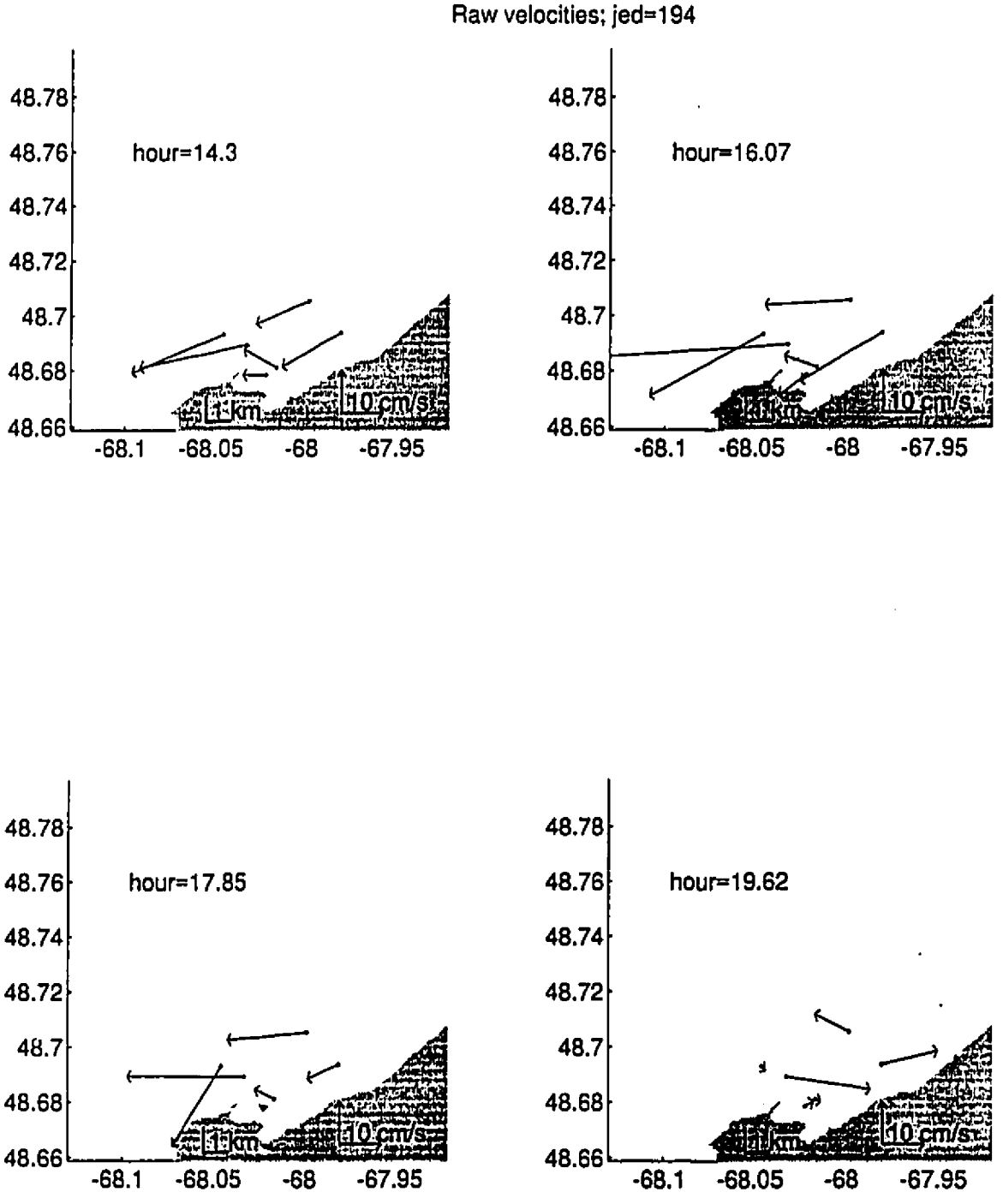

figure 18 continued

Snapshots of the raw velocity data at eight equally spaced times during one M_2 tidal cycle.

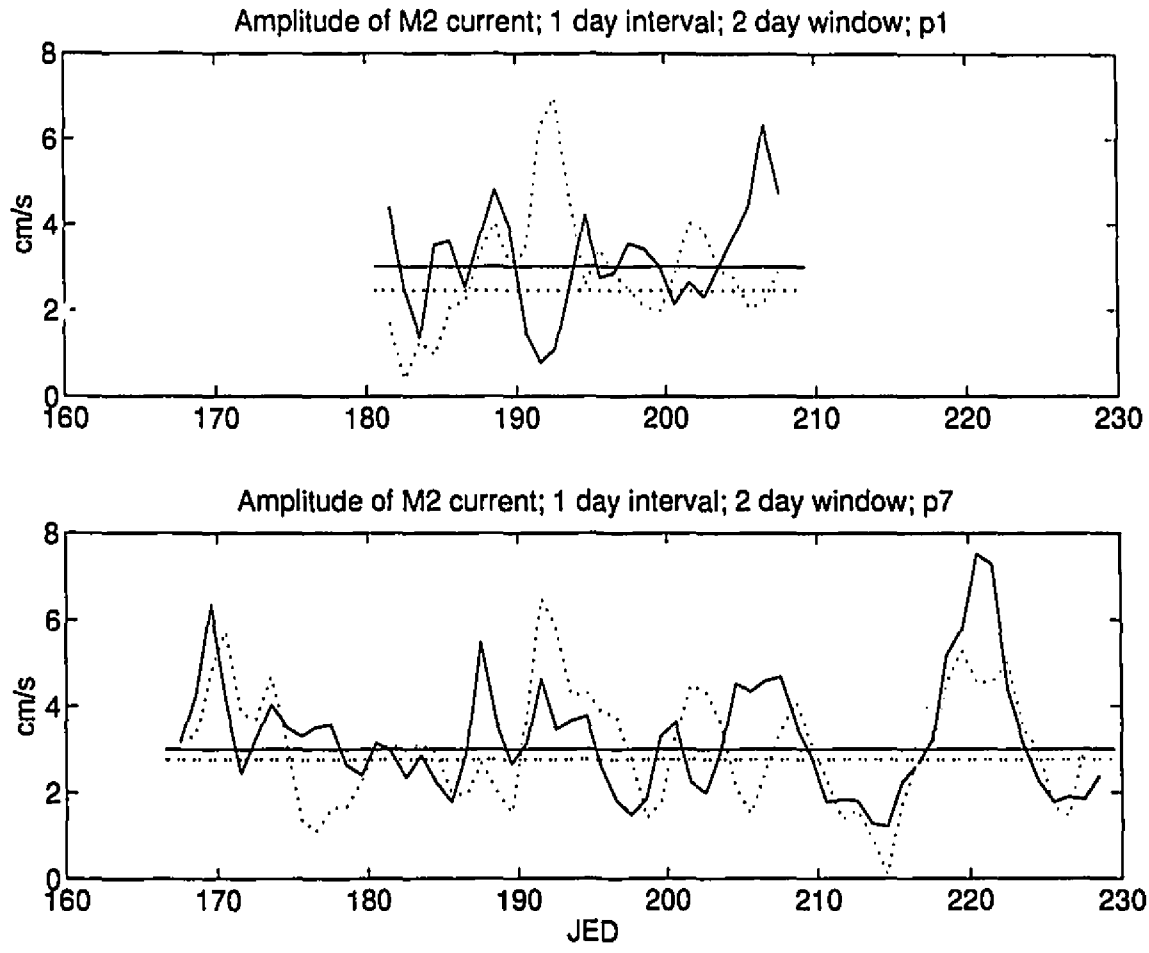

figure 19 Time series of M_2 velocity amplitude using harmonic analyses of two day windows at one day intervals. Stations p1 and p7. The horizontal lines are values obtained by a harmonic analysis of the entire record length. The eastward velocity, u, is given as a solid line and the northward velocity, v, is given as a dotted line. Time is given as julian elapsed day (JED).

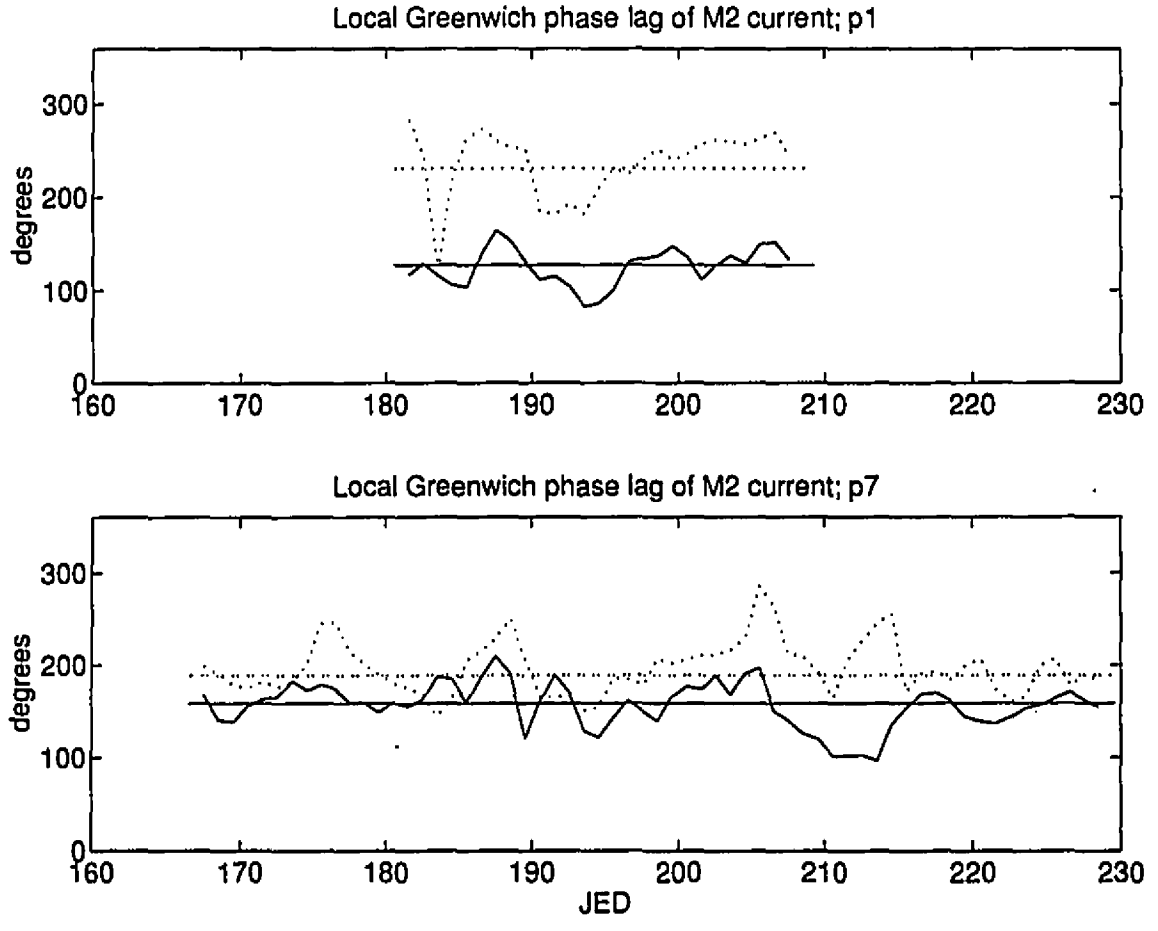

figure 20 Time series of M_2 velocity Greenwich phase lag, g, using harmonic analyses of two day windows at one day intervals. Stations p1 and p7. The horizontal lines are values obtained by a harmonic analysis of the entire record length. The eastward velocity, u, is given as a solid line and the northward velocity, v, is given as a dotted line. Time is given as julian elapsed day (JED).

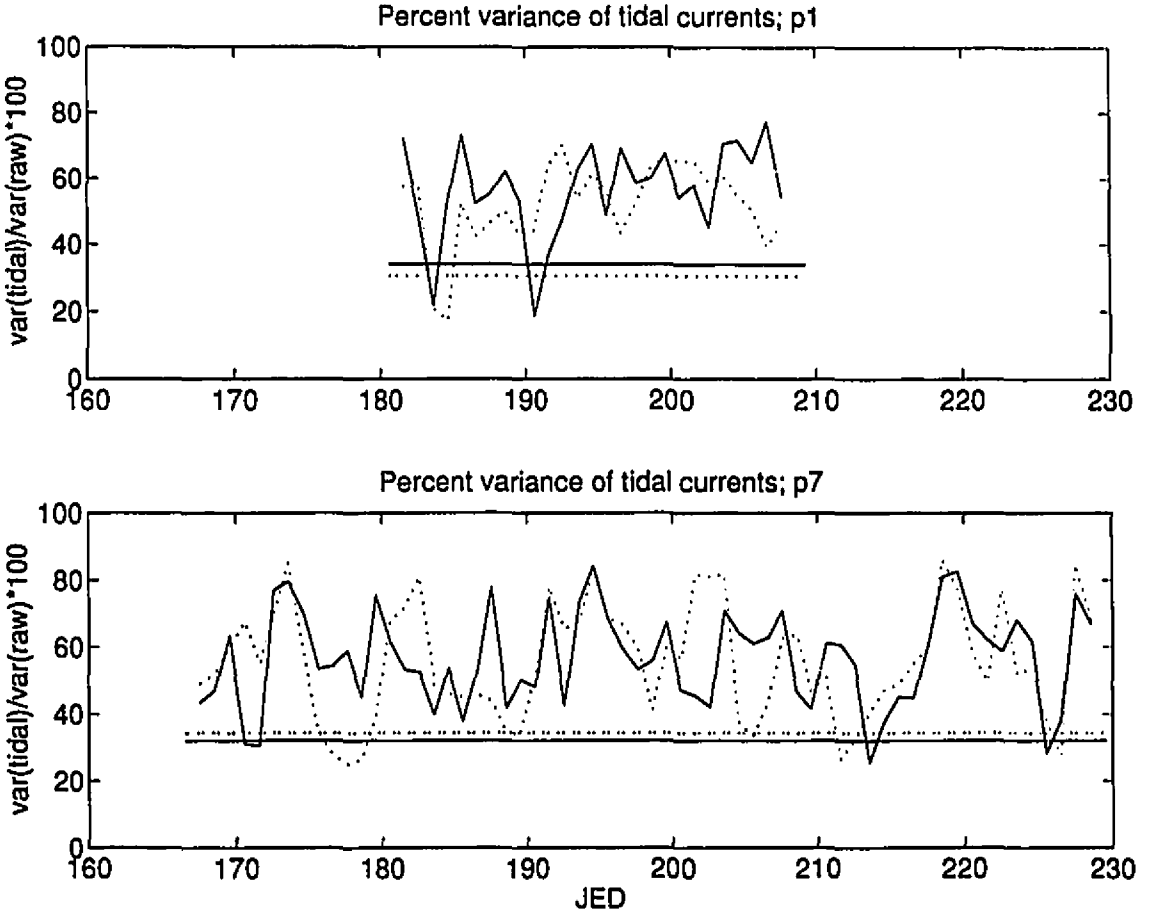

figure 21 Time series of percent variance accounted for by harmonic analyses of two day windows at one day intervals. Stations p1 and p7. The horizontal lines are values obtained by a harmonic analysis of the entire record length. The eastward velocity, u, is given as a solid line and the northward velocity, v, is given as a dotted line. Time is given as julian elapsed day (JED).

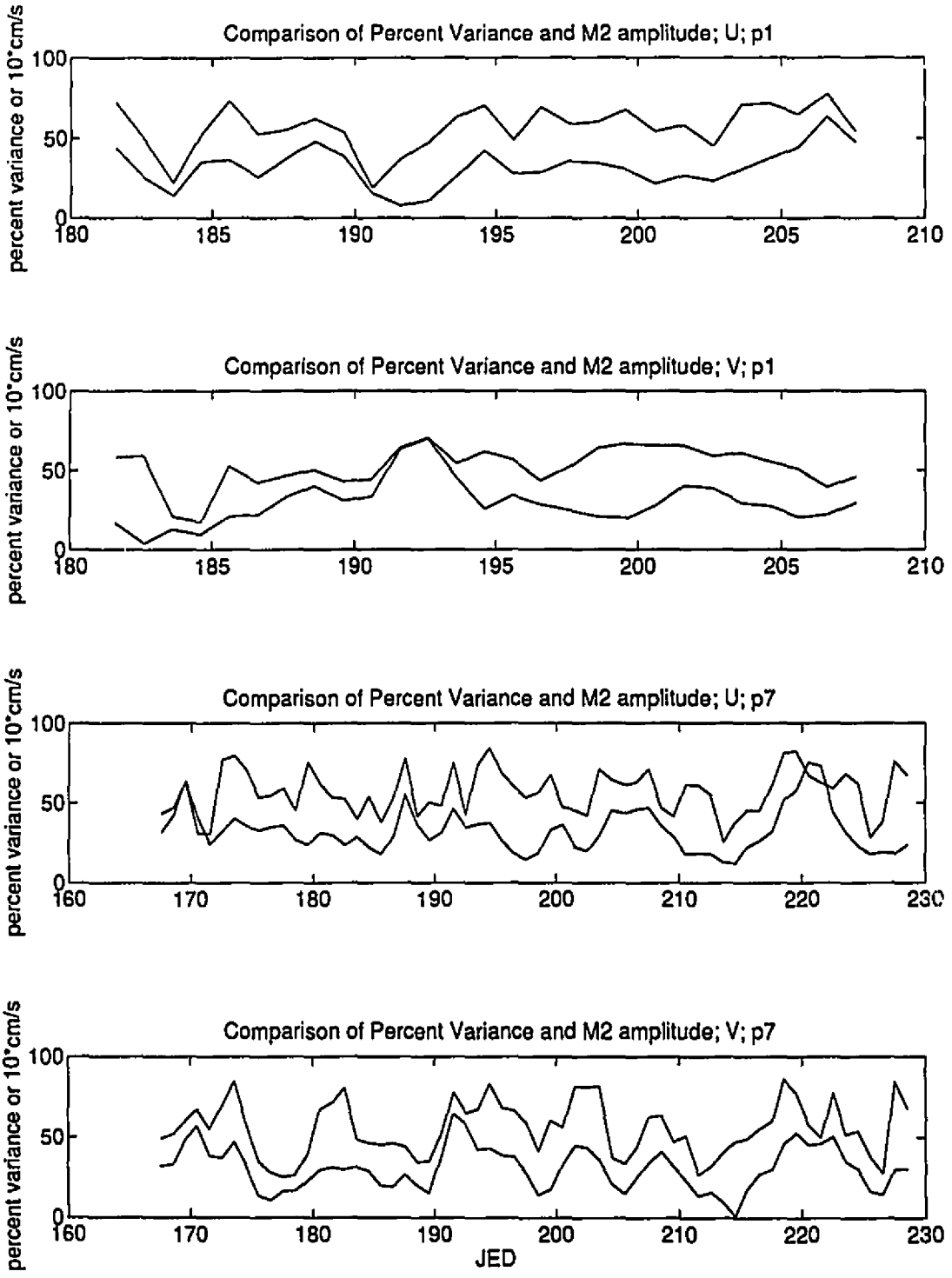

figure 22 Comparison of percent variance accounted for by harmonic analyses with two day windows at one day intervals and M_2 amplitude. Stations p1 and p7. The solid line corresponds to percent variance, and the dotted line corresponds to the M_2 amplitude in 10 x cm s^{-1}. Time is given as Julian Elapsed Day (JED).

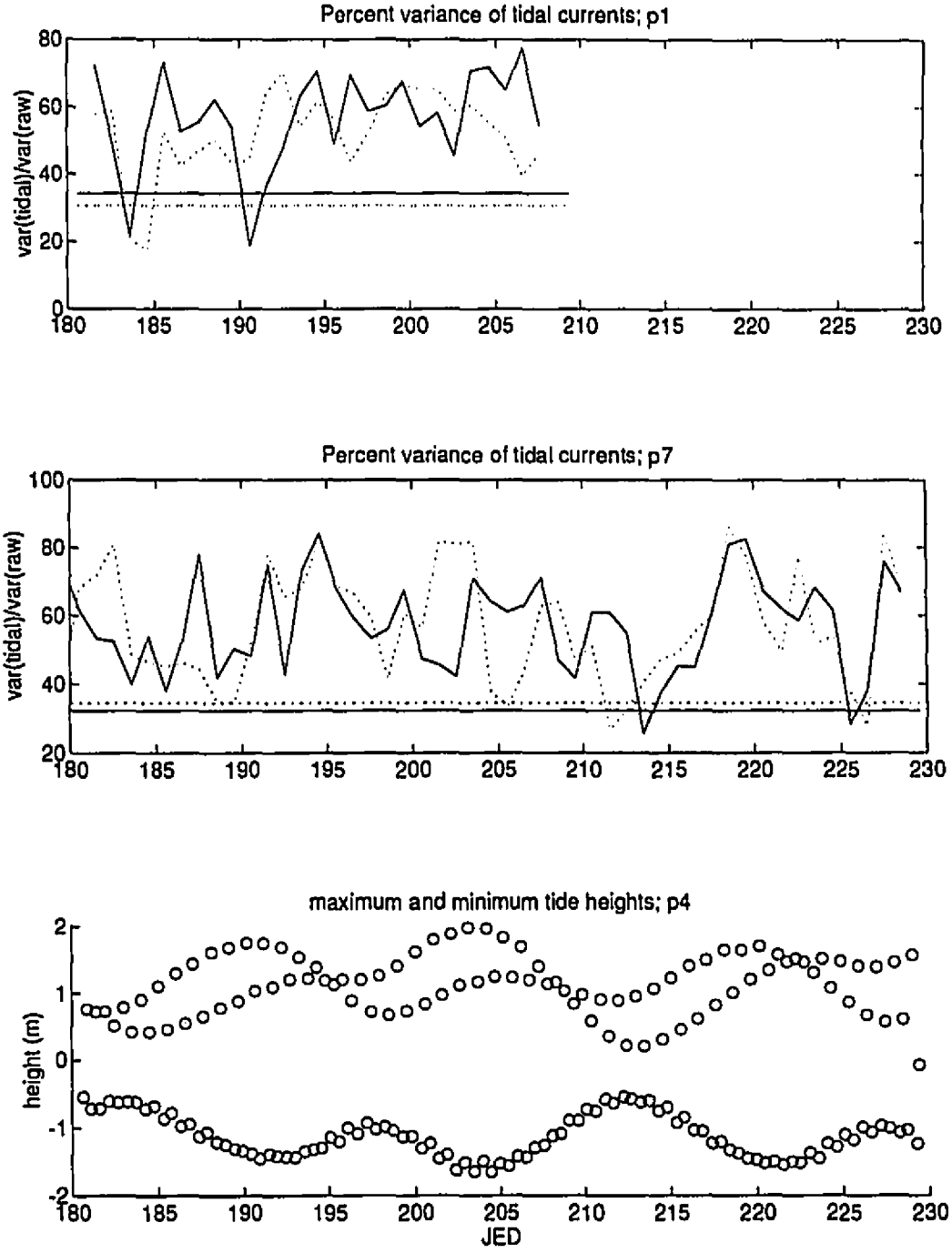

figure 23 Comparison of percent variance accounted for by harmonic analyses with two day windows at one day intervals at stations p1 and p7, and the spring-neap cycle of the tide depth time series at station p4. In the upper two plots, eastward (u) velocity is given as a solid line and northward (v) velocity is given as a dotted line. The horizontal lines refer to the values obtained when calculating percent variance explained by a tidal analysis of the entire time series. Time is given as Julian Elapsed Day (JED).

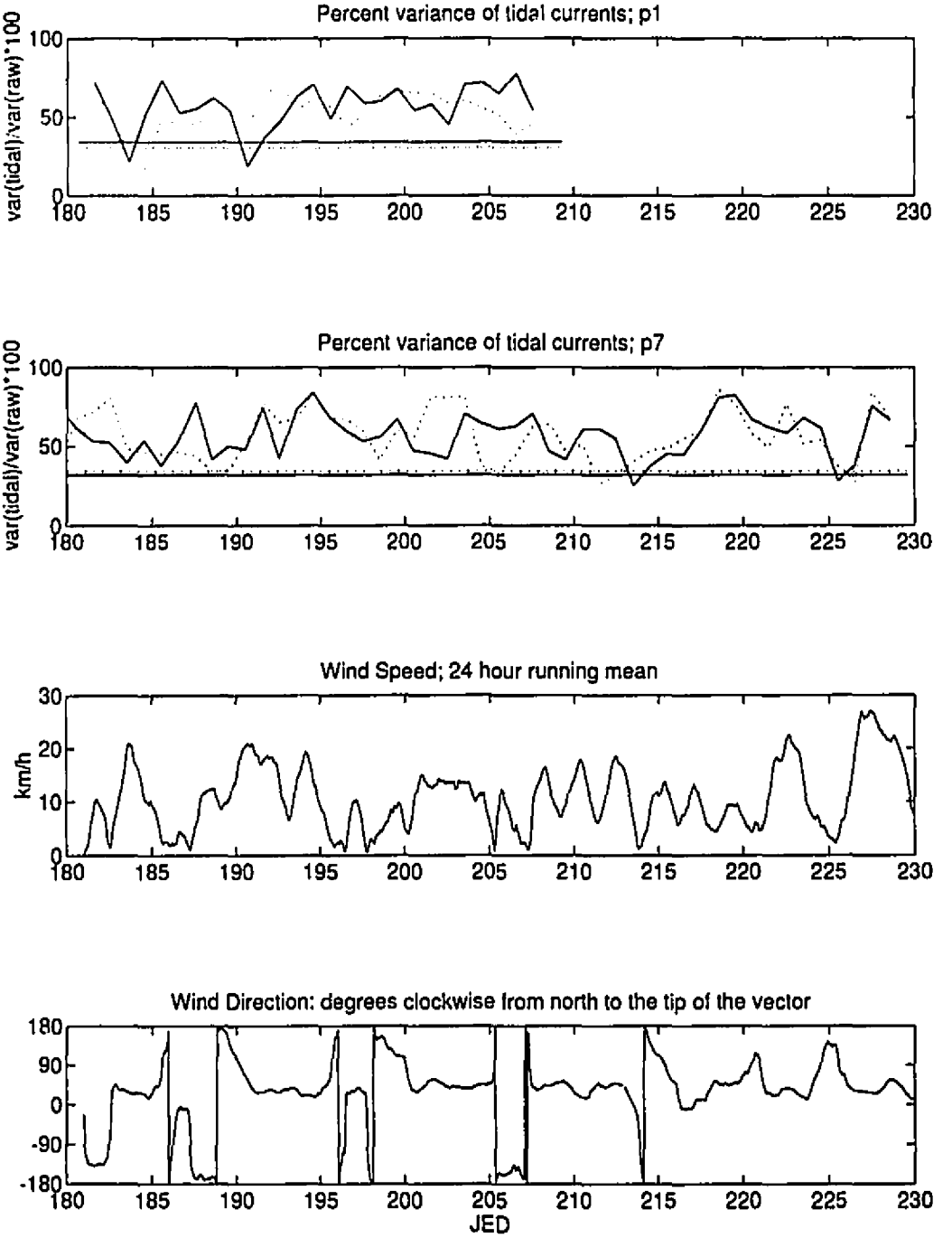

figure 24 Comparison of percent variance accounted for by harmonic analyses with two day windows at one day intervals at stations p1 and p7, and the wind at Mont-Joli airport. In the upper two plots, eastward (u) velocity is given as a solid line and northward (v) velocity is given as a dotted line. The horizontal lines refer to the values obtained when calculating percent variance explained by a tidal analysis of the entire time series. Time is given as Julian Elapsed Day (JED).

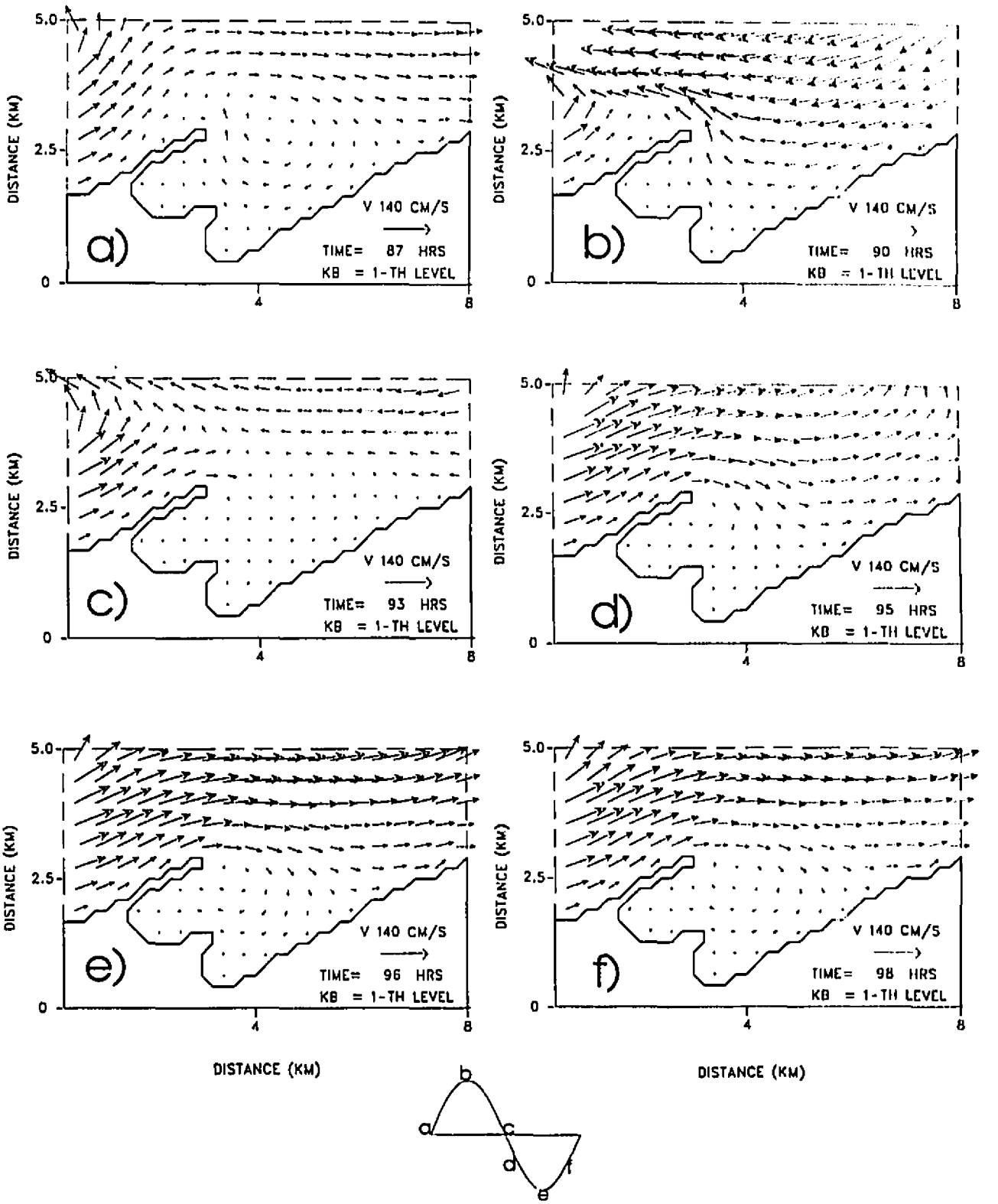

figure 25 Numerical simulation of surface currents at L'Anse du Petit Mitis due to M_2 tidal forcing with an eastward mean flow at six intervals during one M_2 tidal cycle: a) low slack tide; b) peak flood; c) high slack tide; d) 1 hour before peak ebb; e) peak ebb; and f) 2 hours after peak ebb. Taken from figure 2 of van der Baaren *et al*, 1995.

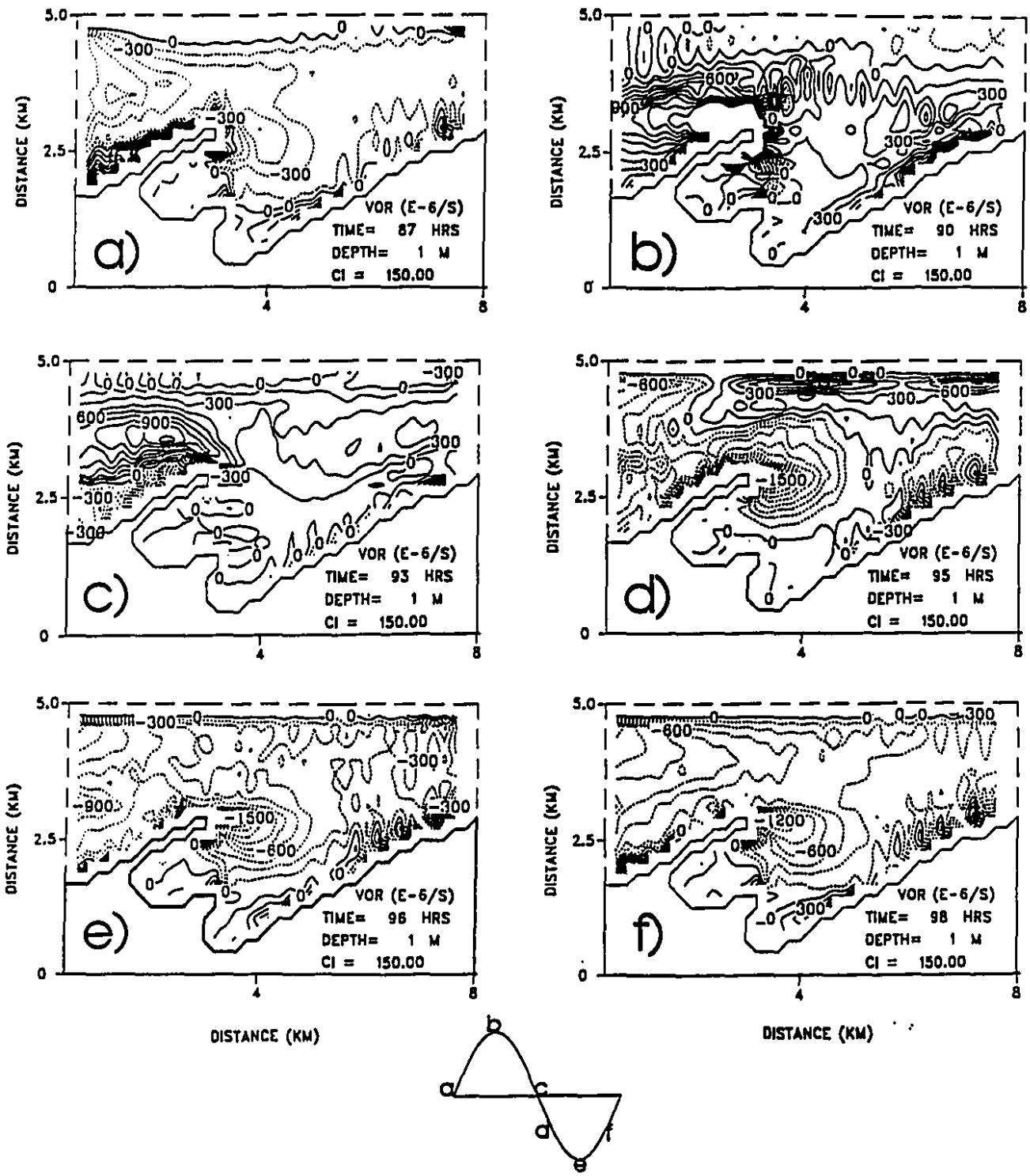

figure 26 Surface vorticity contours due to M_2 tidal forcing at six intervals during one M_2 tidal cycle: a) low slack tide; b) peak flood; c) high slack tide; d) 1 hour before peak ebb; e) peak ebb; and f) 2 hours after peak ebb. Vorticity is given as 10^{-6} s^{-1}. Taken from figure 4 of van der Baaren *et al*, 1995.

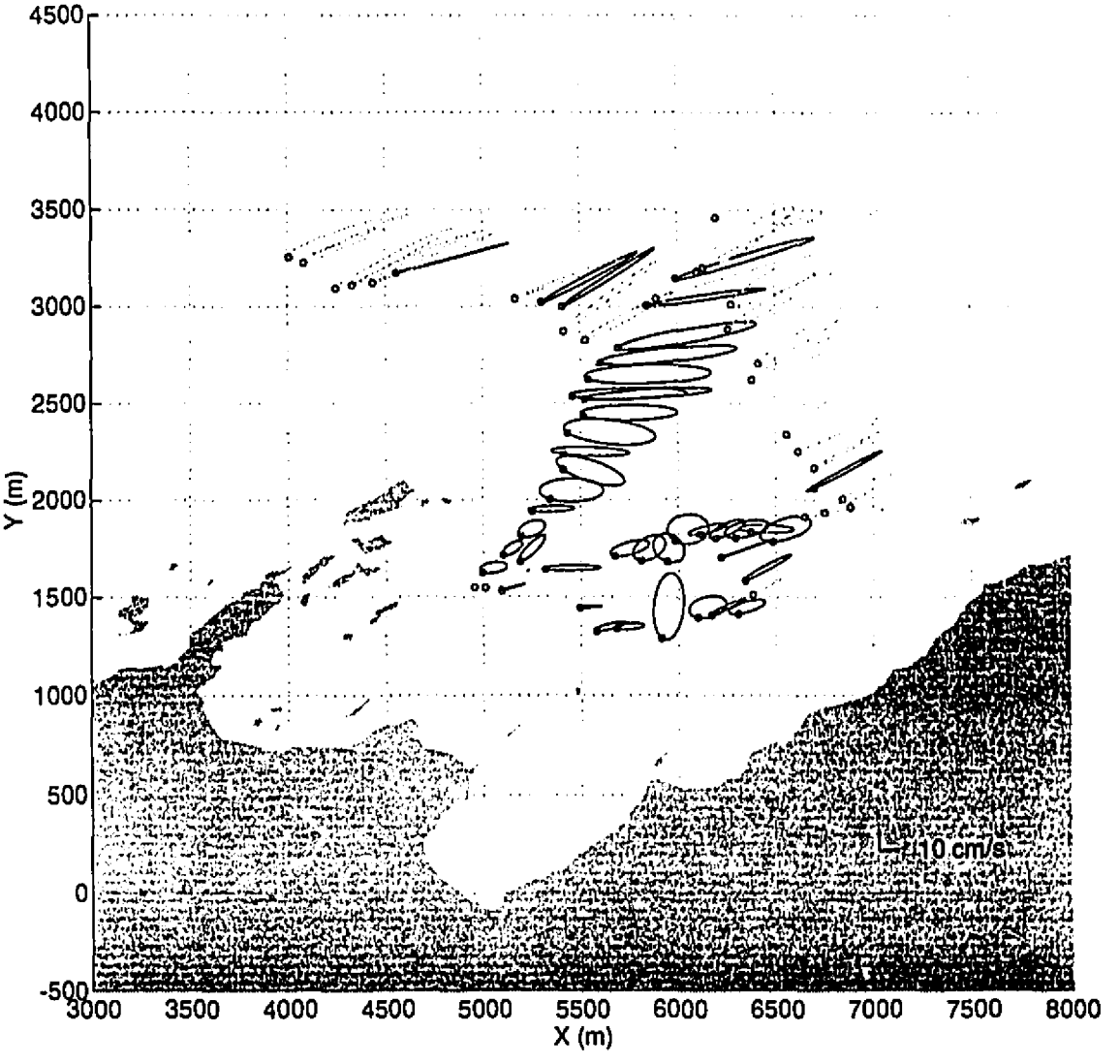

figure 27 M_2 tidal ellipses taken from depth averaged Acoustic Doppler Current Profiler (ADCP) data collected during the summer of 1995 (Bang, Laval, and Ingram, unpublished data). Phase is given as a circle on the perimeter of an ellipse. Grey ellipses represent clockwise rotation, and solid ellipses represent anticlockwise rotation. Location (0,0) corresponds to 48°39'57.8" N latitude and 68°05'19.0" W longitude.

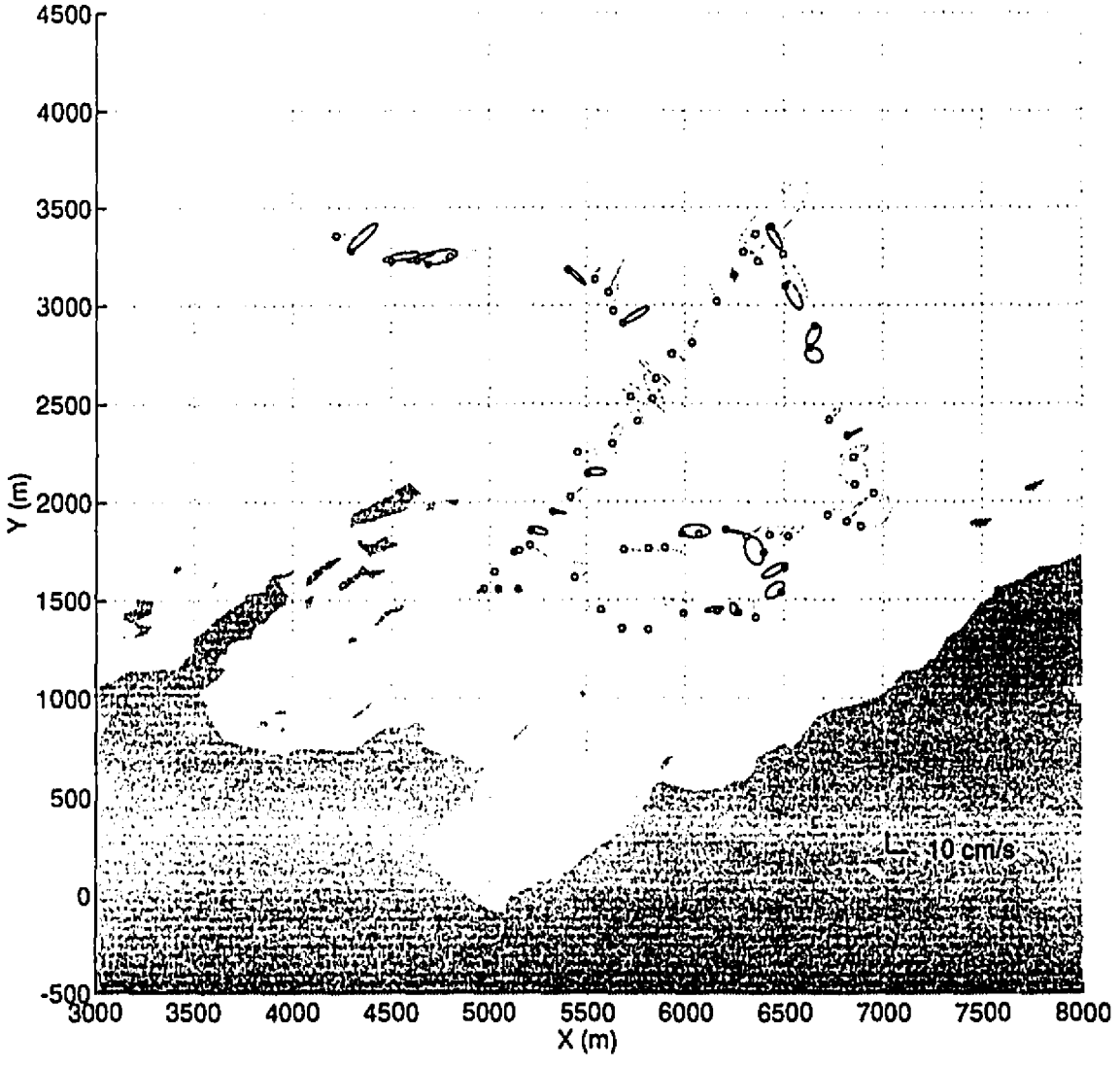

figure 28 M_4 tidal ellipses taken from depth averaged Acoustic Doppler Current Profiler (ADCP) data collected during the summer of 1995 (Bang, Laval, and Ingram, unpublished data). Phase is given as a circle on the perimeter of an ellipse. Grey ellipses represent clockwise rotation, and solid ellipses represent anticlockwise rotation. Location (0,0) corresponds to 48°39'57.8" N latitude and 68°05'19.0" W longitude.

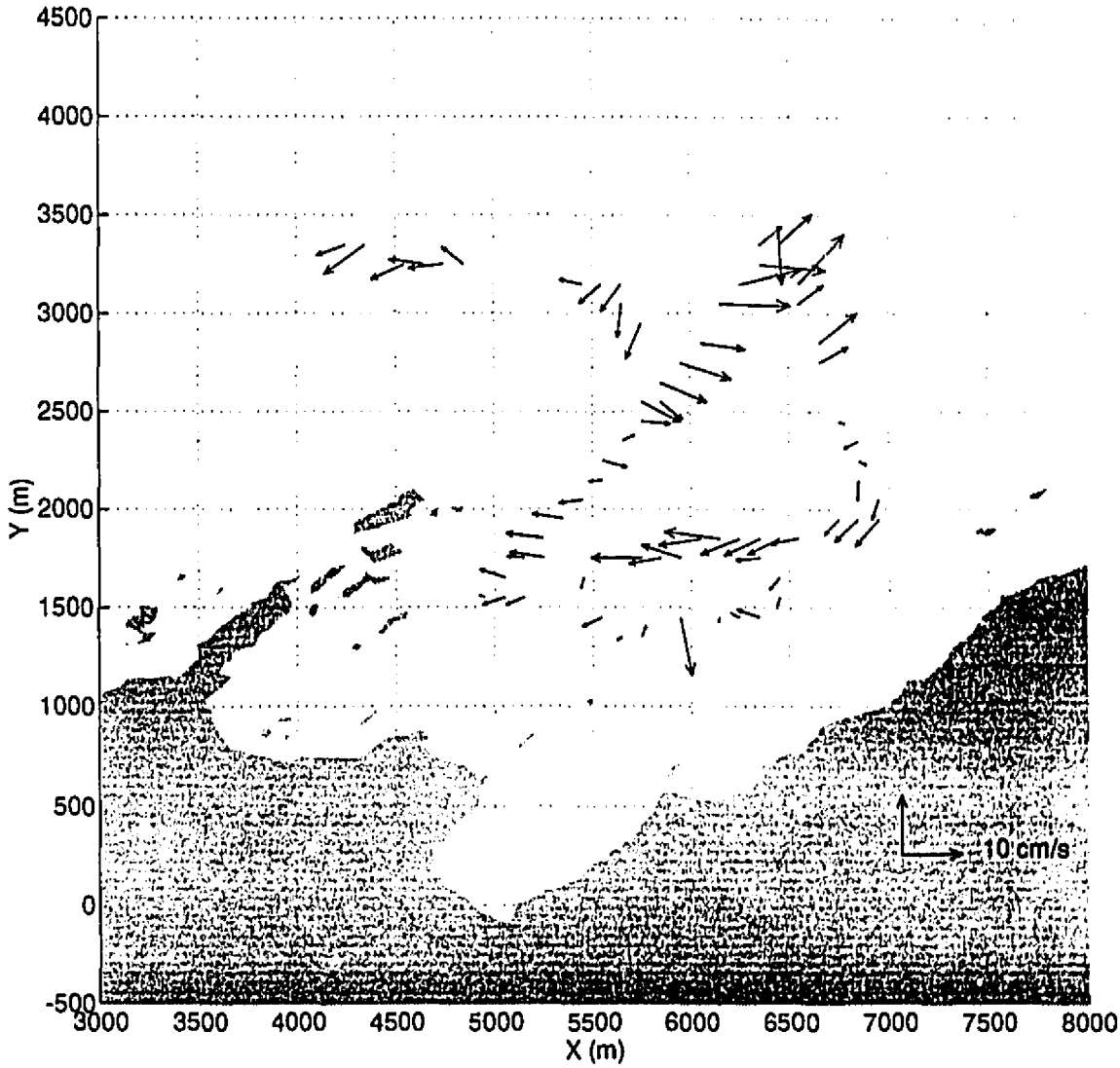

figure 29 Eulerian vector averaged velocities taken from depth averaged Acoustic Doppler Current Profiler (ADCP) data collected during the summer of 1995 (Bang, Laval, and Ingram, unpublished data). Phase is given as a circle on the perimeter of an ellipse. Grey ellipses represent clockwise rotation, and solid ellipses represent anticlockwise rotation. Location (0,0) corresponds to 48°39'57.8" N latitude and 68°05'19.0" W longitude.

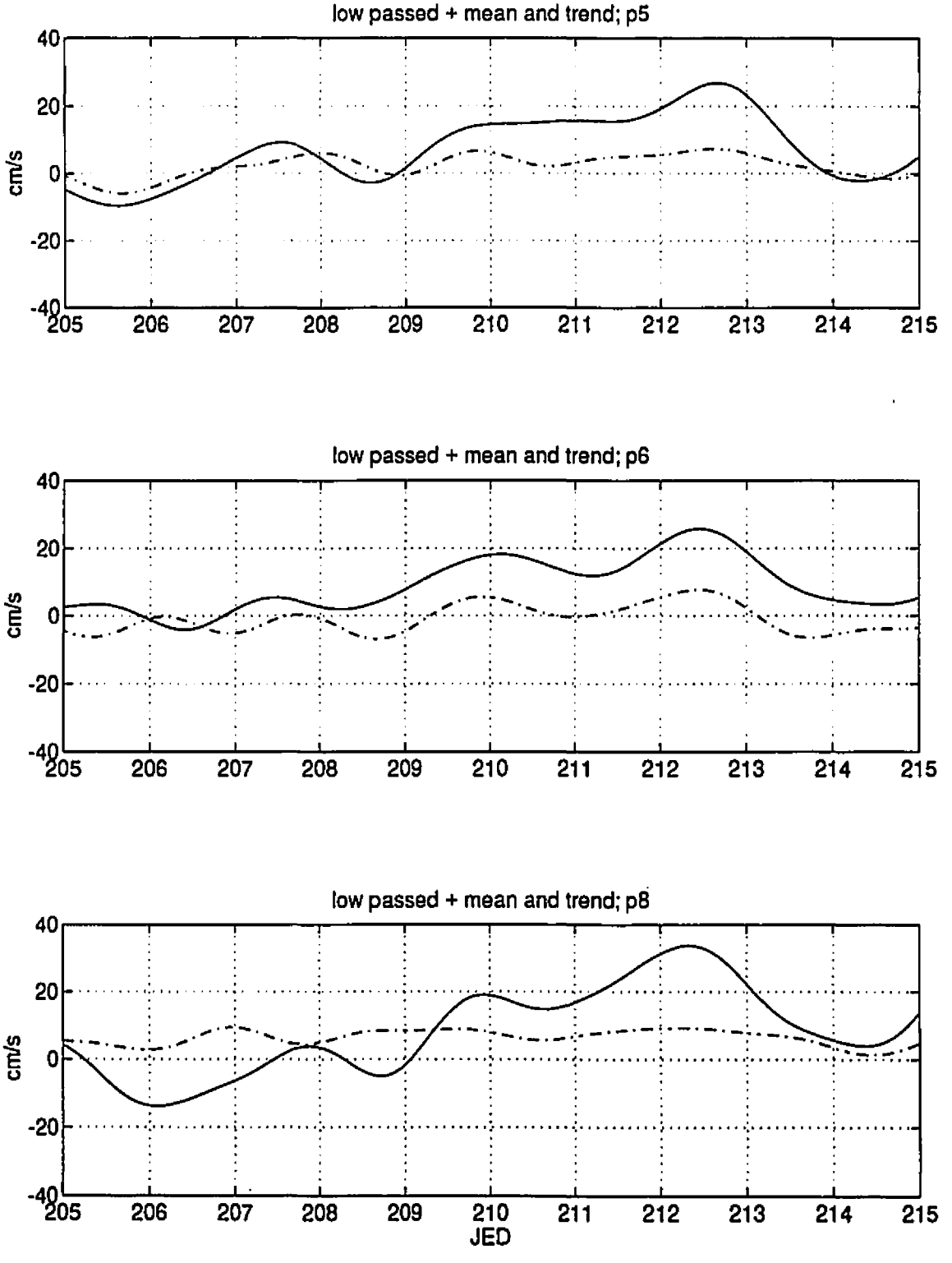

figure 30 Time series constructed from low passed, mean and trend time series data. Stations p5, p6 and p8. Eastward velocity (u) is given as a solid line and northward velocity (v) is given as a dashed line. Time is given as Julian Elapsed Day (JED).